

DOCTORAL THESIS

Micromechanics of dental cement paste: Experiments and multiscale modeling

submitted in satisfaction of the requirements for the degree
Doctor of Science in Civil Engineering
of the Vienna University of Technology, Department of Civil Engineering

DISSERTATION

Mikromechanik von Dentalzementstein: Experimente und Mehrskalenmodellierung

ausgeführt zum Zwecke der Erlangung des akademischen Grades eines
Doktors der technischen Wissenschaften
eingereicht an der Technischen Universität Wien, Fakultät für Bauingenieurwesen

von

Ing. **Petr Dohnalík**
[REDACTED]

Betreuer:

Univ. Prof. Dipl.-Ing. Dr. techn. **Christian Hellmich**
Institut für Mechanik der Werkstoffe und Strukturen
Technische Universität Wien

Ko-Betreuer:

Univ. Prof. Dipl.-Ing. Dr. techn. **Bernhard L.A. Pichler**
Institut für Mechanik der Werkstoffe und Strukturen
Technische Universität Wien

Gutachter:

Prof. Ing. **Jiří Němeček** Ph. D. DSc.
Department of Mechanics, Faculty of Civil Engineering
Czech Technical University in Prague

Univ. Prof. Dipl.-Ing. Dr. sc. nat. **Philipp J. Thurner**
Institut für Leichtbau und Struktur-Biomechanik
Technische Universität Wien

Wien, im September 2022

.....

Acknowledgements

I am sincerely grateful to have had the privilege to pursue a doctoral degree at Vienna University of Technology. An opportunity, that I could hardly have imagined ten years ago but which fulfilled me over the years. It would have not been possible to accomplish this work without the help of numerous people, who contributed to the scientific results presented and provided me the essential support and encouragement.

First and foremost, I would like to express my gratitude to the supervisors of my research work at the Institute for Mechanics of Materials and Structures. My sincerest thanks go to Bernhard Pichler for his guidance, support, and patience throughout the years. I also highly appreciate his introduction into the scientific research work as well as the realm of cementitious materials. I also thank Christian Hellmich for our discussions, his support, and his dedication to science that always kept me motivated. I am also thankful for the stimulating working environment he creates as the head of the institute. I would like to thank Philipp Thurner from Vienna University of Technology and Jiří Němeček from Czech Technical University in Prague for examining this thesis.

This work would not have been possible without the funding of the Horizon 2020 research and innovation programme under the Marie Skłodowska-Curie Actions held by the European Union. I gratefully acknowledge this support which enabled my research at Vienna University of Technology.

I am thankful for my former and current colleagues at the laboratory on Lilienthalgasse as well as the offices at Karlsplatz in Vienna for creating a positive and encouraging work environment. My special thanks go to Eva Binder, Rodrigo Díaz Flores, Luis Zelaya-Lainez, Nabor Jimenez Segura, Vítězslav Štembera, Markus Königsberger, and Sophie Schmid who closely noticed my ups and downs and were always supportive during my studies. I want to thank Wolfgang Dörner not only for the help provided during the preparation of the experiments, but also for his understanding and the pleasant atmosphere he creates in the laboratory workshop. I also thank Olaf Lahayne for our fruitful collaboration and discussions regarding experimental mechanics. I also want to thank Astrid Schuh, Gabriele Ostrowski, and Martina Pöll for their help in easing the workload as regards administrative affairs. I would like to thank the IT team, Jan Valeš and David Kaufmann, for taking care of our daily work tools.

I want to thank Gilles Richard for his support and excellent leadership over the last years, especially during the industrial secondment. I am grateful that I have had the opportunity to meet the R&D team at Septodont in Saint-Maur-des-Fossés. My special thanks go to Rachida LeGrand and Mounir Djoudi with respect to the effective supply of Biodentine, our enriching discussions, and productive collaboration.

I am truly grateful for the opportunity to have met the professors and researchers within the ERICA project who shared their knowledge and extensive experience at the project meetings. I would also like to thank the ERICA PhD students for creating a good team spirit and maintaining it despite the pandemic restrictions. My special thanks go to Miryea Nicole Borg, Magdalena Janota, Adrian-Alexandru Pîrvan, Rémi Albert Boris Kogon, and Örs Istok for their encouragement.

I thank all my friends in Europe who have always lent a sympathetic ear and have always been ready to give a pep talk. They helped me to persist throughout the hardest time of the PhD. Above all, I thank my family. I am truly grateful for their endless support, care, and love.

Abstract

Biodentine is a cementitious material for dental applications marketed by the company Septodont (Saint-Maur-des-Fossés, France). In terms of its chemical composition, Biodentine is very similar to Portland cements used in construction. Nevertheless, the stiffness and strength of hardened Biodentine exceed the corresponding properties of comparable construction cement pastes by a factor of two to three.

Due to the heterogeneous microstructure of the investigated dental cement paste, its macroscopic mechanical properties are functions of the physical properties of the microscopic constituents and their interaction. That was the motivation for the present work. Experimental and theoretical methods of multiscale mechanics were used to microscopically and macroscopically characterize the stiffness and strength of well-hardened Biodentine and to explain the relationship between the experimental results using a quantitative multiscale material model. This goal was achieved in three steps. Thus, the present thesis is organized in three chapters following the Introduction.

Chapter 2 is devoted to the experimental study of well-hardened dental cement paste using nanoindentation and ultrasonic pulse velocity measurements. 5746 nanoindentation tests were performed on test grids, in order to characterize the microstructural constituents of the dental cement paste. Based on the measurement results, 5746 values for both the indentation modulus and the indentation hardness were determined and presented as histograms. They were explained as a superposition of three lognormal distributions each. The latter were preferred to the usually adopted normal distributions, in order to account for the fact that both the indentation modulus and the indentation hardness are positive definite quantities. Two of the three lognormal distributions relate to two types of calcite-reinforced hydration products that differ in their packing density. The third lognormal distribution relates to nanoindentation tests into very stiff and strong particles made of cement and zirconia. In such tests, the particles act as larger indenters that are pushed into the much more compliant hydrate matrix. The macroscopic, homogenized stiffness of the composite material was quantified using the measurements from 325 ultrasonic pulse velocity tests. Finally, theoretical bounds for the macrostiffness of the dental cement paste were calculated based on the stiffnesses of the microscopic solid constituents and their volume fractions. The theoretical lower limit of the macrostiffness is larger than the actual material stiffness determined from the ultrasonic tests. This discrepancy proves the existence of grain boundary defects in the microstructure.

Chapter 3 of this thesis is dedicated to micromechanical modeling of the elastic stiffness of well-hardened dental cement paste. The microstructure of the material is represented as a highly disordered arrangement of the material constituents. The two calcite-reinforced hydrate populations, cement, and zirconia were considered as spherical material phases. The grain boundary defects were introduced in the form of closed circular microcracks which are isotropically orientated in space. Deviating from the usual approach which consists of assigning uniform stiffness values to the material phases, lognormal stiffness distributions from the nanoindentation analysis were assigned to the two calcite-reinforced hydrate populations in the context of an innovative approach. The scale transition from the microstructure to the composite material was accomplished with the self-consistent homogenization scheme of continuum micromechanics. In combination with the macroscopic stiffness of hardened dental cement paste known from the ultrasonic tests, the density of the grain boundary defects and the Poisson's ratio of the calcite-reinforced hydrate populations could be quantified. With regard to the upscaling of the stiffness, the micromechanical model described is practically equivalent to a much simpler alternative model, in which the two hydrate populations are each

assigned uniform stiffnesses (= median values of the stiffness distributions). With regard to the downscaling of stresses, however, the alternative model only provides averaged microstresses, while the model based on two lognormal stiffness distributions allows for quantification of beta-distributed microstresses.

Chapter 4 of this thesis is dedicated to the strength of Biodentine. In the experimental part, the development of the compressive strength of the material during curing at 37°C in the first four weeks after production was investigated. For this purpose, cylindrical specimens with a length-to-diameter ratio of 1.84 and 1.34 were subjected to destructive uniaxial compression tests. The material exhibits a small degree of ductility during the first few hours after production. However, once the material age exceeds 24 hours, the stress-strain relationships are practically linear up to the compressive strength, at which the specimens fail in a brittle fashion, causing them to fall into many fragments. The strength development of Biodentine can be well described by fitting an empirical formula which was developed for the strength development of concrete, and which was published in the *fib* Model Code 2010. The (true) uniaxial compressive strength of Biodentine can be quantified by multiplying the experimentally determined strength values with correction factors. The latter decrease with decreasing length-to-diameter ratio of the cylindrical specimens, and they were taken from the guideline ASTM C39 for testing of concrete. In the modeling part, the multiscale model of Biodentine developed in Chapter 3 of the present work was extended in order to explain the final uniaxial compressive strength of the material. The model establishes a quantile-based correlation between the lognormal stiffness and strength distributions of the two calcite-reinforced hydrate populations. The analysis suggests that the microscopic hydrates are, in good approximation, subjected to uniaxial compression and exhibit shear failure. When the macroscopic material strength is reached, 63% of the material volume of Biodentine has a degree of utilization larger than 99%. This explains pronounced fragmentation of the material under failure load, and also illustrates the highly optimized nature of the material.

Kurzfassung

Biodentine ist ein von der Firma Septodont (Saint-Maur-des-Fossés, Frankreich) vermarktetes zementgebundenes Material für zahnmedizinische Anwendungen. In Hinblick auf seine chemische Zusammensetzung ist Biodentine sehr ähnlich zu den im Bauwesen verwendeten Portlandzementen. Dennoch übertreffen die Steifigkeit und Festigkeit von ausgehärtetem Biodentine-Dentalzementstein die entsprechenden Eigenschaften der vergleichbaren Bauelemente um den Faktor zwei bis drei.

Die makroskopischen mechanischen Kennwerte des untersuchten Dentalzementsteins sind aufgrund seiner heterogenen Mikrostruktur Funktionen von physikalischen Eigenschaften seiner mikroskopischen Bestandteile und deren Interaktion. Das war die Motivation für die vorliegende Arbeit. Es wurden experimentelle und theoretische Methoden der Mehrskalmechanik verwendet, um die Steifigkeit und Festigkeit von ausgehärtetem Biodentine-Dentalzementstein mikroskopisch und makroskopisch zu charakterisieren sowie die Beziehung zwischen den Versuchsergebnissen mit Hilfe eines quantitativen Mehrskalmaterialmodells zu erklären. Dieses Ziel wurde in drei Schritten erreicht. Somit ist die vorliegende Arbeit nach der Einleitung in drei Kapitel gegliedert.

Kapitel 2 ist der experimentellen Untersuchung von ausgehärtetem Dentalzementstein mit Hilfe von Nanoindentation und Ultraschall-Pulsgeschwindigkeitsmessungen gewidmet. 5746 Nanoindentationstests wurden an gitterförmig angeordneten Teststellen durchgeführt, um die mikrostrukturellen Bestandteile des Dentalzementsteins zu charakterisieren. Anhand der Messergebnisse wurden 5746 Zahlenwerte sowohl des Eindringmoduls als auch der Eindringhärte ermittelt und als Histogramme dargestellt. Sie wurden als Überlagerung von jeweils drei Lognormalverteilungen erklärt. Letztere wurden den üblicherweise verwendeten Normalverteilungen vorgezogen, um der Tatsache Rechnung zu tragen, dass sowohl der Eindringmodul als auch die Eindringhärte positive definite Größen sind. Zwei der jeweils drei Lognormalverteilungen beziehen sich auf zwei Arten von kalzitverstärkten Hydratationsprodukten, die sich in ihrer Packungsdichte unterscheiden. Die jeweils dritte Lognormalverteilung bezieht sich auf Nanoindentationstests in sehr steife und feste Partikel aus Zement und Zirkoniumdioxid. Bei solchen Tests fungieren die Partikel als größere Eindringkörper, die in die wesentlich nachgiebigere Hydratmatrix gedrückt werden. Mit Hilfe der Messwerte aus 325 Ultraschallprüfungen wurde die makroskopische, homogenisierte Steifigkeit des Kompositmaterials quantifiziert. Schließlich wurden theoretische Schranken für die Makrosteifigkeit des Dentalzementsteins auf Basis der Steifigkeiten der mikroskopischen Festkörperbestandteile und deren Volumenanteile berechnet. Die untere theoretische Schranke für die Makrosteifigkeit ist größer als die aus den Ultraschalltests ermittelte tatsächliche Materialsteifigkeit. Diese Diskrepanz beweist die Existenz von Korngrenzflächendefekten im Mikrogefüge.

Kapitel 3 der vorliegenden Arbeit ist der mikromechanischen Modellierung der elastischen Steifigkeit von ausgehärtetem Dentalzementstein gewidmet. Die Mikrostruktur des Materials wurde als hochgradig ungeordnete Anordnung der Materialbestandteile modelliert. Die beiden kalzitverstärkten Hydratpopulationen, Zement und Zirkoniumdioxid wurden als kugelförmige Materialphasen berücksichtigt. Die Korngrenzflächendefekte wurden in Form von geschlossenen kreisförmigen Mikrorissen mit isotrop verteilter Ausrichtung eingeführt. Abweichend vom üblichen Zugang, der darin besteht, den Materialphasen jeweils einheitliche Steifigkeitswerte zuzuordnen, wurde im Zuge einer innovativen Herangehensweise den beiden kalzitverstärkten Hydratpopulationen die lognormalen Steifigkeitsverteilungen aus der Nanoindentationsanalyse zugewiesen. Der Skalenübergang von der Mikrostruktur zum Kompositmaterial wurde mit dem selbstkonsistenten Homogenisierungsschema der Kontinuumsmechanik bewerkstelt-

ligt. In Kombination mit der aus den Ultraschalltests bekannten makroskopischen Steifigkeit von ausgehärtetem Dentalzementstein konnten die Dichte der Korngrenzflächendefekte und die Querdehnungszahl der kalzitverstärkten Hydratpopulationen quantifiziert werden. In Hinblick auf das Hochskalieren der Steifigkeit ist das beschriebene mikromechanische Modell praktisch gleichwertig zu einem wesentlich einfacheren Alternativmodell, bei dem den beiden Hydratpopulationen jeweils einheitliche Steifigkeiten (= Medianwerte der Steifigkeitsverteilungen) zugewiesen werden. In Hinblick auf das Hinunterskalieren von Spannungen liefert das Alternativmodell allerdings ausschließlich gemittelte Mikrospannungen, während es das auf zwei lognormalen Steifigkeitsverteilungen beruhende Modell erlaubt, beta-verteilte Mikrospannungen zu quantifizieren.

Kapitel 4 der vorliegenden Arbeit ist der Festigkeit von Biodentine gewidmet. Im experimentellen Teil wurde die Entwicklung der Druckfestigkeit des Materials während des Aushärtens bei 37°C in den ersten vier Wochen nach Herstellung untersucht. Dazu wurden zylindrische Proben mit einem Länge-zu-Durchmesser Verhältnis von 1,84 bzw. 1,34 zerstörenden einaxialen Druckversuchen unterworfen. In den ersten wenigen Stunden nach seiner Herstellung weist das Material ein wenig Duktilität auf. Sobald das Materialalter aber 24 Stunden übersteigt, sind die Spannungs-Dehnungs-Beziehungen praktisch linear bis zur Druckfestigkeit, bei der die Proben spröde versagen, indem sie in zahlreiche Bruchstücke zerspringen. Die Festigkeitsentwicklung von Biodentine lässt sich gut durch Anpassen einer empirischen Formel beschreiben, die für die Festigkeitsentwicklung von Beton entwickelt und im *fib* Model Code 2010 veröffentlicht wurde. Die (wahre) einaxiale Druckfestigkeit von Biodentine kann durch Multiplikation der experimentell ermittelten Festigkeitswerte mit Korrekturfaktoren quantifiziert werden. Letztere nehmen mit abnehmendem Länge-zu-Durchmesser Verhältnis der Probenzylinder ab und wurden der Richtlinie ASTM C39 für mechanisches Testen von Beton entnommen. Im Modellierungsteil wurde das in Kapitel 3 der vorliegenden Arbeit entwickelte Mehrskalmodell von Biodentine erweitert, um die schlussendlich erreichte einaxiale Druckfestigkeit des Materials zu erklären. Das Modell stellt eine auf Quantilen beruhende Korrelation zwischen den lognormalen Steifigkeits- und Festigkeitsverteilungen der beiden kalzitverstärkten Hydratpopulationen her. Die Analyse legt nahe, dass die mikroskopischen Hydrate in guter Näherung auf einachsigen Druck beansprucht sind und Schubversagen zeigen. Beim Erreichen der makroskopischen Materialfestigkeit weisen 63% des Materialvolumens von Biodentine Auslastungsgrade auf, die größer als 99% sind. Das erklärt die weitreichende Fragmentierung des Materials unter Versagenslast, und verdeutlicht somit die weitreichende Optimierung des Materials.

Contents

1	Introduction	1
1.1	Motivation	1
1.2	Cementitious biomaterials for dental applications	3
1.3	Fundamentals of micromechanical modeling	5
1.3.1	Representative volume element and scale separation principle	6
1.3.2	Field equations	6
1.3.3	Boundary condition and average rules	7
1.3.4	Definition of homogenized stiffness	7
1.3.5	Introduction of material phases	8
1.3.6	Eshelby problem	10
1.3.7	Estimates of phase strain concentration tensors	10
1.4	Main objectives of the research	11
1.5	Outline of the thesis	12
2	Micromechanics of dental cement paste	14
2.1	Introduction	15
2.2	Materials and methods	16
2.2.1	Sample preparation	16
2.2.2	Roughness testing protocol	17
2.2.3	Grid nanoindentation protocol	18
2.2.4	Statistical evaluation of nanoindentation test results	19
2.2.5	Light microscopy imaging of polished surfaces	20
2.2.6	Ultrasonic pulse transmission	20
2.2.7	Micromechanical stiffness bounds and estimates	22
2.3	Results	23
2.4	Discussion	27
2.4.1	Dental hydrates vs. construction cement hydrates	27
2.4.2	Discussion on curing conditions	28
2.4.3	Propagation of bulk waves in elastic media	29
2.4.4	Statistical analysis of grid nanoindentation data, and inhomogeneous regions probed by the nanoindenter	29
2.5	Conclusions	32
Appendix 2.A	Details on LND identification	32
2.A.1	Solution of the optimization problem	32
2.A.2	Initial search intervals	34
Appendix 2.B	Continuum micromechanics	36
Appendix 2.C	Experimental data	37

3	Stiffness and stress fluctuations in dental cement paste: A continuum micromechanics approach	41
3.1	Introduction	42
3.2	Lognormal microelasticity model for Biodentine	45
3.2.1	Fundamentals of stiffness homogenization	45
3.2.2	Tensorial formulation of lognormal microelasticity model for Biodentine	47
3.2.3	Transition to flat circular slit cracks	51
3.2.4	Scalar expressions for the homogenized bulk and shear moduli	53
3.2.5	Scalar expressions for volumetric and deviatoric strain and stress tensor components	54
3.2.6	Bulk and shear moduli of the hydrates, as functions of the indentation modulus	56
3.2.7	Identification of crack density of Biodentine and Poisson's ratio of hydrates	57
3.3	Application of the lognormal microelasticity model: strain and stress fluctuations	58
3.3.1	Distributions of strain concentration tensor components of the two populations of hydrates	58
3.3.2	Distributions of stress concentration tensor components of the two populations of hydrates	61
3.3.3	Reproducing the distributions of strain and stress concentration tensor components based on generalized beta-distributions	64
3.3.4	Contribution of the microcracks to the stress and strain average rules	65
3.4	Comparison with piecewise uniform microelasticity models	66
3.4.1	Piecewise uniform microelastic properties equivalent to the stiffness distributions of both populations of hydrates	68
3.4.2	Comparison of the equivalent piecewise uniform microelastic properties with their probability density functions	69
3.4.3	Piecewise uniform microelastic model based on median values of bulk and shear moduli of both populations of hydrates	70
3.5	Discussion	70
3.6	Conclusions	73
	Appendix 3.A Macrostiffness characterization by means of ultrasonic pulse velocity measurements	73
	Appendix 3.B Numerical values of integrals involving the lognormal distributions of the two populations of hydrates	76
	Appendix 3.C Components of the Eshelby tensor of thin oblate spheroids	77
4	Strength of dental cement paste: Early age testing and micromechanical explanation at mature ages	78
4.1	Introduction	79
4.2	Compressive strength testing from early to mature material ages	80
4.2.1	Production and storage of cylindrical specimens	80
4.2.2	Destructive compression testing	82
4.2.3	Discarding tests influenced by imperfections	84
4.2.4	Stress-strain diagrams	86
4.2.5	Early-age strength evolution	86
4.2.6	Failure modes	90
4.3	Standards-based evaluation of experimental data	90
4.3.1	Early-age strength evolution	90

4.3.2	Influence of the length-to-diameter ratio of cylindrical specimens on their compressive strength	91
4.4	Microscopic origin of the macroscopic uniaxial compressive strength of mature Biodentine	94
4.4.1	Results from grid nanoindentation on mature Biodentine	94
4.4.2	Continuum micromechanics model for the elastic stiffness of mature Biodentine	97
4.4.3	Microscopic stress distributions in calcite-reinforced hydrates as a function of their indentation modulus	99
4.4.4	Shear failure of calcite-reinforced hydrates	99
4.4.5	Correlations between lognormal distributions of indentation modulus, indentation hardness, and the equivalent shear strength	100
4.4.6	Identification of lognormal parameters of the equivalent shear strength	101
4.4.7	Degree of utilization of hydrates as a function of their indentation moduli	102
4.4.8	Shear failure of HDCR hydrates explains macroscopic strength of mature Biodentine	102
4.5	Conclusions	104
Appendix 4.A	Quantile-based correlation between two lognormal distributions . .	106
Appendix 4.B	Analysis of the equivalent shear strength of the LDCR hydrates . .	107
5	Summary, conclusions, and outlook	110
5.1	Summary of the experimental studies	110
5.2	Summary of the developed models	111
5.3	Research contribution and main findings	112
5.4	Perspectives	113
	Bibliography	115
	Personal information	126
	Curriculum Vitae	126
	Scientific Dissemination	127

Chapter 1

Introduction

1.1 Motivation

Over the past decades, researchers have endeavored to lower the amount of hydraulic cement clinker in the cementitious materials without compromising their mechanical performance. This tremendous effort has been made in order to address the global greenhouse gases emitted by producing Portland cement clinker (Müller and Harnisch, 2008; Miller et al., 2016). The involved strategy usually resorts to blending the Portland cement powder with supplementary cementitious materials (SCM), such as fly ash, ground blast-furnace slag, or silica fume. In this way, the hydraulic cement clinker, demanding high amount of energy for its production, is substituted by a less energy demanding hydraulic component. Another approach is to use high-performance cement, where the word “performance” refers to the uniaxial compressive strength of these hydraulic materials. Therefore, less, high-quality material is used instead of more, but less strong material. Moreover, the former as well as the latter can possess very similar material compositions.

The ordinary Portland cement, the basic ingredient of concretes and mortars, consists of cement clinker and small amount (units of wt.%) of gypsum to prevent flash setting of the fresh cement paste. The cement clinker mainly consists of four hydraulic mineral constituents (Taylor et al., 1997):

- Tricalcium silicate (Ca_3SiO_5) makes the majority of cement clinker and it is important for development of cement’s strength in the first 28 days of hydration.
- Dicalcium silicate (Ca_2SiO_4) is the second most abundant constituent of cement clinker. It contributes to the strength development at later material ages, i.e. after 28 days of hydration.
- Tricalcium aluminate ($\text{Ca}_3\text{Al}_2\text{O}_6$) is one of the minor constituents of cement clinker. Its rapid setting is typically inhibited by adding gypsum into the cement powder.
- Tetracalcium aluminoferrite ($\text{Ca}_2\text{AlFe}_2\text{O}_5$) is dark-colored constituent of the cement clinker and with tricalcium aluminate takes approximately the same portion of the cement clinker composition.

Mixing the cement clinker with water results in an exothermic reaction, within which hydration products precipitate from the supersaturated solution and create a binding agent that glues together the cement paste itself as well as the aggregates in the case of mortars and concretes.

The most important product of hydration is calcium-silicate-hydrate; abbreviated in cement chemical nomenclature as C-S-H. Calcium hydroxide (portlandite) and aluminates (usually referred to as AFm, AFt phases) are minor hydration products (Taylor et al., 1997). C-S-H forms from hydration of tri- and dicalcium silicates and it occupies the largest volume fraction in the microstructure of a cement paste. Therefore, the C-S-H is the material constituent (phase) that plays a major role in influencing the mechanical properties of cementitious materials.

Given that the C-S-H governs the macroscopic stiffness and strength behavior of the cementitious materials, the quest to get a better grasp of its microstructure and micromechanical properties has been in the focus of researchers ever since. Grid nanoindentation combined with micromechanical modeling can provide such a valuable information by means of linking the micro- and macrostructure properties. In this context, pioneering work using results from grid nanoindentation as microscopic input for upscaling of the elastic stiffness of cement paste was introduced by Constantinides and Ulm (2004). 200 indentation tests into the calcium-silicate-hydrate matrix gave access to 200 values of indentation moduli which were translated into moduli of elasticity, assuming a Poisson's ratio of 0.24 (Constantinides, 2002). Subsequently, the histogram, created based on these statistical sample, revealed two peaks that were represented as a superposition of two Gaussian probability density functions. The mean values of these distributions were used as an input for stiffness upscaling of a cement paste, delivering a homogenized modulus of elasticity amounting to 23.2 GPa. Complementary ultrasound pulse velocity measurements gave access to the macroscopic modulus of elasticity amounting to 22.8 GPa (Constantinides and Ulm, 2004). As the consequence of the successful implementation of the results from nanoindentation into the micromechanical models, this method was further applied to ultra high performance concrete (Sorelli et al., 2008), to cement paste, gypsum, and aluminum alloy (Němeček et al., 2013), to polymer-modified cement paste (Göbel et al., 2018), and to self-compacting concrete modified with nanoparticles (Stefaniuk et al., 2019). The latter study used Gaussian probability density functions describing stiffness distributions of two populations of hydration products as an input for micromechanical modeling.

Micromechanical strength modeling of the cementitious materials was the logical next step after validation of the micromechanical stiffness models. In this context, careful consideration of the microstructural morphology of the C-S-H was necessary for successful prediction of strength evolution from early-age to mature states of cement pastes, and mortars based on the elastic properties of their non-aging constituents, their volume fractions (expressed as a function of hydration degree), and their mutual mechanical interaction (Pichler and Hellmich, 2011). This inspired several follow up works on compressive strength modeling of concrete (Königsberger et al., 2018) and even recycled concrete (Königsberger and Staquet, 2018), which accounted for narrow zones around the aggregates (referred as interfacial transition zones - ITZs) typically considered to be the weakest link within the concrete microstructure. As regards compressive strength modeling of blended cement pastes, different approach was chosen by Hlobil et al. (2016) assuming that the compressive strength is governed by apparent tensile strength of the C-S-H globule.

The above-mentioned microstructure models provide a validated approach that can be applied to study (macroscopic) strength and stiffness properties of other materials based on their microstructures. Compressive strength of Biodentine significantly outperforms chemically similar construction cement pastes, which suggest that this material has a highly optimized microstructure. Thus, deciphering the microscopical physical phenomena, governing the high mechanical strength of this dental cement paste, is the main motivation of the present thesis.

The following sections give a brief introduction to dental cement pastes and fundamentals of micromechanical modeling. The former introduces Biodentine's composition and its mechanical properties in accordance to published scientific literature, whereas the latter revisits the micromechanical modeling used as a tool for investigation of the studied material.

1.2 Cementitious biomaterials for dental applications

Important requirements on cementitious dental materials are that the freshly mixed material is workable for a few minutes and that it hardens quickly thereafter. Moreover, dental cement pastes must be biocompatible with the surrounding living tissues. Typical application of the cementitious dental materials include endodontic restorative procedures such as, root-end filling, perforation repair, apexification, or pulp-capping (Primus et al., 2019).

The use of Portland cement as dental restorative material can be traced back to the end of 19th century, where it was used by Dr. Witte for placement under a gold filling (Deus et al., 2014). The idea of using a material based on Portland cement for filling cavities in human teeth was revisited a century later by Dr. Torabinejad and Mr. White. Their work resulted in two patents (Torabinejad and White, 1993a,b) and two studies (Torabinejad et al., 1993; Lee et al., 1993) on sealing ability of this cementitious material, introduced under the name "Mineral Trioxide Aggregate" (MTA). The composition of the main hydraulic components of this novel material was identical to the composition of type I (ordinary) Portland cement, which was also explicitly recommended in the patents as the material of choice. The ordinary Portland cement was blended with bismuth oxide (Bi_2O_3) in order to increase opacity of the material on radiographs (Torabinejad and White, 1993a). Since its first introduction, the name MTA has been quickly adopted and became a generic name for other products that are based on Portland cement powder, or tri-/dicalcium silicates, such that many of the subsequent commercial cementitious dental materials bear this abbreviation in their names (Primus et al., 2019). Nowadays, more than 20 cement-based dental materials are available in the market. These products typically vary in radiopacifying agent, fineness of the powder, or presence of other additives (Primus et al., 2019).

This thesis refers to a cementitious dental material named "BiodentineTM" (Septodont, Saint-Maur-des-Fossés, France) that comes in capsules, containing 0.7 grams of cement powder, and tubes, containing approximately 200 μL of mixing liquid. Although the exact composition and particle sizes are corporate secrets, some studies on these topics are available in the scientific literature. Next two paragraphs describe the results of these studies.

In order to quantify the phase composition of the dry powder, X-ray diffraction (XRD) analyses with Rietveld refinement have been carried out (Camilleri et al., 2013; Graziotin-Soares et al., 2019; Li et al., 2019). With respect to the listed literature, the reported results were the following:

- 80.1 wt% of tricalcium silicate (Ca_3SiO_5), 14.9 wt% of calcium carbonate (CaCO_3 , also known as calcite), and 5.0 wt% zirconium dioxide (ZrO_2) (Camilleri et al., 2013).
- 23.8 wt% monoclinic Ca_3SiO_5 , 56.6 wt% triclinic Ca_3SiO_5 , 14.9 wt% of CaCO_3 , and 4.7 wt% of ZrO_2 (Graziotin-Soares et al., 2019).
- 4.45 wt% of monoclinic β -dicalcium silicate (Ca_2SiO_4), 73.8 wt% of triclinic Ca_3SiO_5 , 16.6 wt% of CaCO_3 , and 5.15 wt% of ZrO_2 (Li et al., 2019).

These studies suggest that the powder is made up of about 80 wt% of reactive binder, 15 wt% of calcium carbonate, acting as filler material, and 5 wt% of zirconium dioxide providing X-ray

opacity (Laurent et al., 2008, 2012). The mixing liquid contains water (H_2O), calcium chloride (CaCl_2), accelerating the transition of freshly-mixed Biodentine from a moldable gel into a solid material, and a hydrosoluble polycarboxylate-based polymer improving workability at small initial liquid-to-solid mass ratios (Laurent et al., 2008; Bronnec et al., 2010; Laurent et al., 2012).

Advanced grinding of the particles of the Biodentine powder allows for shortening the setting time, and for further accelerating the hydration kinetics. Brunauer-Emmett-Teller (BET) nitrogen gas adsorption was used for quantification of the specific surface area (SSA) of anhydrous Biodentine powder. The values reported in the literature range from $2.81 \text{ m}^2/\text{g}$ (Camilleri et al., 2013), $3.35 \text{ m}^2/\text{g}$ (Li et al., 2019) to $4.00 \text{ m}^2/\text{g}$ (Chang, 2018). Particle size distribution was quantified by means of laser diffraction analysis, which provided access to equivalent diameters. The 10th percentile, the median, and the 90th percentile amount to $1.15 \text{ }\mu\text{m}$, $3.48 \text{ }\mu\text{m}$, and $7.51 \text{ }\mu\text{m}$, respectively (Ha et al., 2015). Backscattered electron (BSE) images of dental cement powder showed particles of characteristic sizes ranging from some 1 to $6 \text{ }\mu\text{m}$ (Li et al., 2019). Using the same imaging technique for a hydrated 28 days old Biodentine paste revealed smaller and evenly distributed particles (Camilleri, 2022). Energy dispersive X-ray (EDX) spectroscopy of Biodentine powder suggested that the CaCO_3 particles are of sub-micrometric size, whereas the clinker and zirconia are of micrometer size (Li et al., 2019).

As regards strength properties of Biodentine, they are usually investigated in comparative studies with other dental materials, in which Biodentine usually outperforms other cementitious materials (Rajasekharan et al., 2014). The next three paragraphs documents several studies on strength properties of dental cement pastes which are available in the scientific literature.

Compressive strength tests are typically carried out in accordance to the ISO 9917:1-2007 standard recommending molds with inner diameter and height of 4 mm and 6 mm, respectively. These specimens are usually exposed to different curing environments.

- Strength of the specimens cured in distilled water, at material ages of one hour as well as one, seven, and 28 days amounted to $140 \pm 1 \text{ MPa}$, $171 \pm 1 \text{ MPa}$, $269 \pm 1 \text{ MPa}$, and $305 \pm 3 \text{ MPa}$, respectively (Butt et al., 2014). Similar values were obtained in Franquin et al. (2010).
- Specimens were exposed to acidic solutions and distilled water with pH-values amounting to 4.4, 5.4, 6.4, and 7.4, respectively, and the compressive strength seven days after production amounted to $59 \pm 5 \text{ MPa}$, $74 \pm 7 \text{ MPa}$, $81 \pm 8 \text{ MPa}$, and $95 \pm 9 \text{ MPa}$, respectively (Elnaghy, 2014).
- To simulate in vivo conditions, Biodentine was cast into molds contaminated with blood or saliva as well as into clean molds which served as a control group. Three days after production, the strength amounted to $177 \pm 28 \text{ MPa}$, and $157 \pm 57 \text{ MPa}$, and $205 \pm 22 \text{ MPa}$, respectively (Subramanyam and Vasantharajan, 2017).
- Similarly, casting Biodentine into molds filled with blood, and testing at material ages of six hours, one, three, and seven days delivered strength values amounting to $34 \pm 9 \text{ MPa}$, $50 \pm 13 \text{ MPa}$, $36 \pm 15 \text{ MPa}$, $39 \pm 12 \text{ MPa}$, respectively (Sheykhrezae et al., 2018).

Due to the challenging aspects of tensile strength testing of small specimens, diametral compression tests (Brazilian splitting test) of cylindrical specimens are usually performed in order to approximate the tensile strength of the dental cement materials. The splitting tests of cylindrical specimens produced in molds with inner diameter and height of 6 mm and 12 mm, respectively, were carried out by Alzraikat et al. (2016). The specimens were cured in

an oven at 37°C for three hours in 100 % relative humidity. Subsequently, they were immersed in distilled water and stored again in the oven for 1 and 21 days which resulted in strength of 7.9 ± 1.9 MPa and 5.0 ± 1.1 MPa, respectively. Similar strength results from the diametral compression test were obtained by testing cylindrical specimens produced from molds with inner diameter and height amounting to 4 mm and 6 mm, respectively. The specimens were cured at 37°C in relative humidity higher than 95 %. The splitting strength values obtained after 1, 28, and 180 days of this treatment amount to 6.3 ± 1.4 MPa, 5.7 ± 0.3 MPa, and 6.8 ± 0.9 MPa, respectively. Nagas et al. (2016) cured the specimens at 37°C in 100 % relative humidity for 21 days which resulted in splitting strength of 12.1 ± 1.4 MPa. Uyanik et al. (2019) quantified the splitting strength after 21 days of curing the specimen at 37°C in 100 % relative humidity delivering strength value of 16.3 ± 0.5 MPa. Elsaka et al. (2019) cured the fresh Biodentine cement pastes inside the molds at 37°C in 100 % relative humidity for the first hour after production; then, the specimens were immersed in 10 mL of deionized distilled water for another 24 hours at 37°C in 100 % relative humidity, resulting in 15.3 ± 0.4 MPa splitting strength. Nagas et al. (2016); Uyanik et al. (2019); Elsaka et al. (2019) tested the cylindrical specimens produced from molds with inner diameter and height amounting to 4 mm and 6 mm, respectively.

Flexural strength of thin prisms with dimensions $10 \times 2 \times 1$ mm³ were tested by means of three point bending test by Natale et al. (2015). The specimens were cured at 37°C in 100 % relative humidity for 48 hours which resulted in flexural strength of 24.4 ± 7.5 MPa. Bi-axial flexural strength of 2 mm thick and 12 mm wide discs were performed by Alhodiry et al. (2014). A disc was placed on three fixed ball bearings arranged around the disc's circumference with angular spacing of 120°. The loading was applied to the center of the disk on the opposite side from the ball bearings through a stainless steel rod of 1 mm radius. The material age at the time of testing was one week at least. The experimentally derived biaxial flexural strength amounts to 9.5 ± 2.9 MPa.

As a summary, from the information available in the literature, Biodentine cement powder consist mainly from finely ground tricalcium silicate, calcium carbonate, and zirconium dioxide. Hardened Biodentine possess compressive strength values that usually surpasses the strength of other dental cement pastes investigated in the comparative studies (Rajasekharan et al., 2018). As discussed in Section 1.1, macroscopic behavior can be explained based on understanding the microstructure of studied material by means of micromechanical modeling. This makes Biodentine an attractive subject for such investigation. However, to the best knowledge of the author this has never been accomplished. Therefore, the basic principles of micromechanical modeling are revisited in next section, following (Königsberger, 2016; Schmid, 2018; Binder, 2019).

1.3 Fundamentals of micromechanical modeling

Macroscopic properties of materials are governed by physical phenomena prevailing at the microscopic scale. Methods of continuum micromechanics provide quantitative link between the micro- and macroscopic word. Thus, if the physical mechanism at the small scales of observation are considered carefully, then the micromechanical modeling can predict the macroscopic material behavior.

1.3.1 Representative volume element and scale separation principle

In continuum micromechanics, the representative volume element (RVE) is considered representative as long as the studied volume of interest fulfils the scale separation principle. This principle states that the dimensions of a structure and the characteristic dimensions of external loading, \mathcal{L} , are larger than the characteristic size of the RVE, ℓ_{RVE} , and that the ℓ_{RVE} must be considerably larger than the characteristic size of the microheterogeneities, d_{het} , see Fig. 1.1. This can be mathematically expressed as:

$$\mathcal{L} \gg \ell_{RVE} \gg d_{het}. \quad (1.1)$$

The first inequality is satisfied, when the \mathcal{L} is by a factor of 2 to 3 larger than ℓ_{RVE} (Drugan and Willis, 1996), and the second inequality is satisfied, when ℓ_{RVE} is by a factor of 5 to 10 larger than d_{het} (Königsberger, 2016). In Eq. (1.1), the \mathcal{L} is defined as the norm of the macroscopic linearized strain tensor \mathbf{E} divided by the norm of the gradient of this tensor (Auriault et al., 2010; Königsberger et al., 2020)

$$\mathcal{L} = \frac{\|\mathbf{E}(\underline{x})\|}{\|\text{GRAD } \mathbf{E}(\underline{x})\|}. \quad (1.2)$$

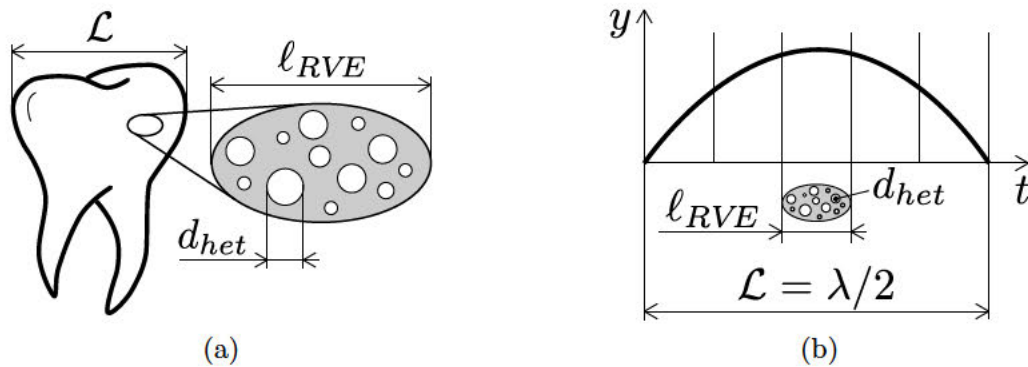


Fig. 1.1. Illustration of the scale separation principle for: (a) a structure with characteristic size \mathcal{L} , within which an RVE is defined having characteristic size ℓ_{RVE} that contains inhomogeneities with characteristic size d_{het} , and (b) a pulse load of characteristic size equal to half of the wavelength, $\mathcal{L} = \lambda/2$, imposed on an RVE with size ℓ_{RVE} containing microheterogeneities of size d_{het} .

1.3.2 Field equations

The field equations refer to all positions \underline{x} inside of the representative volume element V . The linear geometric equations define the linearized strain tensor ε as the symmetric part of the displacement gradient. Denoting the displacement vector as \underline{u} , with $\nabla(\cdot) = \partial(\cdot)/\partial\underline{x}$ as the microscopic gradient, the linear strain-displacement relations read as

$$\varepsilon(\underline{x}) = \frac{1}{2}[\nabla\underline{u}(\underline{x}) + \nabla\underline{u}^T(\underline{x})]. \quad (1.3)$$

The linear constitutive equations refer to linear elastic material behavior. Denoting Cauchy's (second order) stress tensor as $\underline{\sigma}(\underline{x})$ and the (fourth order) elasticity tensor as $\mathbb{C}(\underline{x})$, the linear stress-strain relations read as

$$\underline{\sigma}(\underline{x}) = \mathbb{C}(\underline{x}) : \varepsilon(\underline{x}). \quad (1.4)$$

Finally, the stresses must fulfill the equilibrium conditions, reading as

$$\operatorname{div}\boldsymbol{\sigma}(\underline{x}) = 0. \quad (1.5)$$

1.3.3 Boundary condition and average rules

At the boundary ∂V of the RVE, either strain or stress uniform boundary conditions can be prescribed. In case of uniform strain boundary conditions, denoting the imposed macroscopic strain state as \mathbf{E} , they read as

$$\underline{u}(\underline{x}) = \mathbf{E} \cdot \underline{x}. \quad \forall x \in \partial V. \quad (1.6)$$

For a kinematically admissible (compatible) microstrain field $\boldsymbol{\varepsilon}(\underline{x})$, the uniform strain boundary condition (1.6) implies that the volume average of the microstrain field is equal to the macrostrain (Hill, 1963; Hashin, 1983; Zaoui, 2002):

$$\frac{1}{V} \int_V \boldsymbol{\varepsilon}(\underline{x}) \, dV = \mathbf{E}. \quad (1.7)$$

Hill's lemma reads as (Hill, 1963; Zaoui, 2002):

$$\frac{1}{V} \int_V \boldsymbol{\sigma}(\underline{x}) : \boldsymbol{\varepsilon}(\underline{x}) \, dV = \boldsymbol{\Sigma} : \mathbf{E}, \quad (1.8)$$

where $\boldsymbol{\Sigma}$ denotes the macroscopic (homogeneous) stress within the RVE. Eq. (1.8) implies that the strain energy stored in an RVE can be calculated at the microscopic as well as at the macroscopic scale. Combining Eq. (1.8) with the strain average rule (1.7) yields the stress volume average rule:

$$\frac{1}{V} \int_V \boldsymbol{\sigma}(\underline{x}) \, dV = \boldsymbol{\Sigma}. \quad (1.9)$$

In case of uniform stress boundary conditions, the macroscopic (homogeneous) stresses $\boldsymbol{\Sigma}$ are prescribed at the boundary of the RVE. They are applied in terms of traction vectors $\underline{t}(\underline{x})$ in the form of Cauchy's formula with:

$$\underline{t}(\underline{x}) = \boldsymbol{\Sigma} \cdot \underline{n}(\underline{x}), \quad (1.10)$$

where \underline{n} represents the outward normal vector at the boundary. Due to the equilibrium state of the microscopic stress field $\boldsymbol{\sigma}(\underline{x})$, the stress volume-average rule (1.9) is obtained directly. Using the Hill's lemma yields the strain volume-average rule (1.7) (Zaoui, 2002).

1.3.4 Definition of homogenized stiffness

If the homogenized stiffness tensor \mathbf{C}_{hom} is calculated as the volume average of the microscopic stiffness tensor field $\mathbf{C}(\underline{x})$, then this volume average represents an upper bound for the homogenized stiffness of a material

$$\frac{1}{V} \int_V \mathbf{C}(\underline{x}) \, dV \geq \mathbf{C}_{hom}. \quad (1.11)$$

The access to the homogenized stiffness tensor is obtained through strain concentration tensor field $\mathbf{A}(\underline{x})$. Considering the linearity of the field equations (1.3), (1.5), as well as the boundary

conditions (1.6), or (1.10), the strain concentration tensor field relates the microscopic strain field $\boldsymbol{\varepsilon}(\underline{x})$ and the macroscopic strain \mathbf{E} in linear fashion, reading as:

$$\boldsymbol{\varepsilon}(\underline{x}) = \mathbb{A}(\underline{x}) : \mathbf{E}, \quad (1.12)$$

and inserted into the constitutive equation (1.4) allows for rewriting the stress field as follows:

$$\boldsymbol{\sigma}(\underline{x}) = \mathbb{C}(\underline{x}) : \mathbb{A}(\underline{x}) : \mathbf{E}. \quad (1.13)$$

Inserting the latter to the stress volume-average rule (1.9) and extracting the position-independent macroscopic strain state \mathbf{E} from the integral yields:

$$\boldsymbol{\Sigma} = \frac{1}{V} \int_V \mathbb{C}(\underline{x}) : \mathbb{A}(\underline{x}) : \mathbf{E} \, dV = \frac{1}{V} \int_V \mathbb{C}(\underline{x}) : \mathbb{A}(\underline{x}) \, dV : \mathbf{E}. \quad (1.14)$$

Comparing this equation with the macroscopic version of the elasticity law,

$$\boldsymbol{\Sigma} = \mathbb{C}_{hom} : \mathbf{E}, \quad (1.15)$$

delivers the following expression for the homogenized stiffness (Hill, 1963; Zaoui, 2002):

$$\mathbb{C}_{hom} = \frac{1}{V} \int_V \mathbb{C}(\underline{x}) : \mathbb{A}(\underline{x}) \, dV. \quad (1.16)$$

Inserting the identity tensor to $\mathbb{A}(\underline{x})$ in Eq. (1.16) yields stiffness volume average, see Eq. (1.11), which also implies $\boldsymbol{\varepsilon}(\underline{x}) = \mathbf{E}$, see Eq. (1.12). This aspect underlines that the strain concentration tensor field $\mathbb{A}(\underline{x})$ makes scale transitions possible. As for top-down scale transition, i.e. macro-to-micro concentration (1.12), $\mathbb{A}(\underline{x})$ is used to downscale macroscopic strains to microscopic scale. Regarding the bottom-up scale transition, i.e. micro-to-macro homogenization, $\mathbb{A}(\underline{x})$ allows for upscaling of the microscopic stiffness field, see Eq. (1.16).

Due to the complexity of heterogeneous microstructures, the $\mathbb{A}(\underline{x})$ is not a priori known. This provides the motivation to introduce material phases.

1.3.5 Introduction of material phases

Quasi-homogeneous constituents of the microheterogeneous material, denoted as material phases, facilitates the homogenization of the elastic stiffness. They occupy specific subvolumes V_i of the RVE V . Volume fractions of the material phases read as $f_i = V_i/V$, with $i = 1, 2, \dots, N$, where N stands for the number of material phases. In addition, material phases are characterized by specific elastic stiffness tensors \mathbb{C}_i . Average phase strains and stresses of material phase i are introduced as:

$$\boldsymbol{\varepsilon}_i = \frac{1}{V_i} \int_{V_i} \boldsymbol{\varepsilon}(\underline{x}) \, dV, \quad i = 1, 2, \dots, N, \quad (1.17)$$

$$\boldsymbol{\sigma}_i = \frac{1}{V_i} \int_{V_i} \boldsymbol{\sigma}(\underline{x}) \, dV, \quad i = 1, 2, \dots, N. \quad (1.18)$$

Considering the volumes of material phases, defined above, the integrals in the strain volume-average rule (1.7) and stress volume-average rule (1.9) can be, respectively, rewritten as

$$\mathbf{E} = \frac{1}{V} \int_V \boldsymbol{\varepsilon}(\underline{x}) \, dV = \frac{1}{V} \sum_{i=1}^N \int_{V_i} \boldsymbol{\varepsilon}(\underline{x}) \, dV = \sum_{i=1}^N \left[\frac{V_i}{V} \frac{1}{V_i} \int_{V_i} \boldsymbol{\varepsilon}(\underline{x}) \, dV \right] = \sum_{i=1}^N f_i \boldsymbol{\varepsilon}_i, \quad (1.19)$$

$$\boldsymbol{\Sigma} = \frac{1}{V} \int_V \boldsymbol{\sigma}(\underline{x}) \, dV = \frac{1}{V} \sum_{i=1}^N \int_{V_i} \boldsymbol{\sigma}(\underline{x}) \, dV = \sum_{i=1}^N \left[\frac{V_i}{V} \frac{1}{V_i} \int_{V_i} \boldsymbol{\sigma}(\underline{x}) \, dV \right] = \sum_{i=1}^N f_i \boldsymbol{\sigma}_i. \quad (1.20)$$

Inserting the strain concentration rule (1.12) in the strain volume-average rule, and extracting macroscopic strains from the integral, yields

$$\boldsymbol{\varepsilon}_i = \frac{1}{V_i} \int_{V_i} \mathbb{A}(\underline{x}) : \mathbf{E} \, dV = \frac{1}{V_i} \int_{V_i} \mathbb{A}(\underline{x}) \, dV : \mathbf{E} = \mathbb{A}_i : \mathbf{E}, \quad i = 1, 2, \dots, N, \quad (1.21)$$

where \mathbb{A}_i denotes the phase strain concentration tensor. Because of the uniform stiffness inside the phase volumes V_i , the phase-specific version of the elasticity law reads as:

$$\boldsymbol{\sigma}_i = \mathbb{C}_i : \boldsymbol{\varepsilon}_i, \quad i = 1, 2, \dots, N. \quad (1.22)$$

Inserting the phase strain concentration law (1.21) into phase elasticity law (1.22) yields

$$\boldsymbol{\sigma}_i = \mathbb{C}_i : \mathbb{A}_i : \mathbf{E}, \quad i = 1, 2, \dots, N, \quad (1.23)$$

which inserted into Eq. (1.20) yields a relation between the macrostress $\boldsymbol{\Sigma}$ and the macrostrain \mathbf{E} . Its comparison with the macroscopic version of the elasticity law (1.15) delivers the following expression for the homogenized stiffness tensor (Hill, 1963; Zaoui, 2002)

$$\mathbb{C}_{hom} = \sum_{i=1}^N f_i \mathbb{C}_i : \mathbb{A}_i. \quad (1.24)$$

By analogy to the phase strain concentration tensors, phase stress concentration tensors \mathbb{B}_i establish links between the macrostress and the average phase stresses:

$$\boldsymbol{\sigma}_i = \mathbb{B}_i : \boldsymbol{\Sigma}, \quad i = 1, 2, \dots, N. \quad (1.25)$$

The stress concentration tensors are related to the strain concentration tensors, as shown in the following lines. The macroscopic elasticity law (1.15) solved for the macrostrain reads as:

$$\mathbf{E} = (\mathbb{C}_{hom})^{-1} : \boldsymbol{\Sigma}. \quad (1.26)$$

Inserting it into phase strain concentration law (1.21) and the resulting expression for $\boldsymbol{\varepsilon}_i$ into elasticity law (1.22) yields a relation between the microstresses $\boldsymbol{\sigma}_i$ and the macrostress $\boldsymbol{\Sigma}$. Comparing this relation with Eq. (1.25) yields

$$\mathbb{B}_i = \mathbb{C}_i : \mathbb{A}_i : (\mathbb{C}_{hom})^{-1}, \quad i = 1, 2, \dots, N. \quad (1.27)$$

Eqs. (1.21), (1.24), and (1.27) underline that strain concentration tensors allows for scale transitions in continuum micromechanics. These strain concentration tensors are estimated based on Eshelby/Laws-type matrix-inclusion problems (Eshelby, 1957; Laws, 1977).

1.3.6 Eshelby problem

Eshelby problem is a matrix inclusion problem that consist of a single three-dimensional ellipsoidal inclusion of stiffness \mathbf{C}_i embedded in an infinite matrix of stiffness \mathbf{C}_∞ . The matrix is subjected to a remote strain boundary condition, such that it is in infinite distance from the inclusion:

$$\underline{u}(\underline{x}) = \mathbf{E}_\infty \cdot \underline{x}, \quad \text{for } \underline{x} \rightarrow \infty. \quad (1.28)$$

Eshelby (1957) found out that the strain within an inclusion is constant. He related the phase strain $\boldsymbol{\varepsilon}_i$ to fourth-order Hill tensor (also know as morphology tensor) \mathbf{P}_i^∞ , stiffness contrast between the inclusion \mathbf{C}_i and the matrix \mathbf{C}_∞ , as well as the remote strain \mathbf{E}_∞ . Mathematically expressed as:

$$\boldsymbol{\varepsilon}_i = [\mathbb{I} + \mathbf{P}_i^\infty : (\mathbf{C}_i - \mathbf{C}_\infty)]^{-1} : \mathbf{E}_\infty. \quad (1.29)$$

The Hill tensor depends on shape and orientation of the inclusion. It relates the inverse of the matrix stiffness tensor \mathbf{C}_∞^{-1} with dimensionless Eshelby tensor $\mathcal{S}_i(\nu_\infty)$ depending on Poisson's ratio of the infinite matrix ν_∞ ,

$$\mathbf{P}_i^\infty = \mathcal{S}_i(\nu_\infty) : \mathbf{C}_\infty^{-1}. \quad (1.30)$$

Eshelby's result (1.29) is reminiscent of the phase strain concentration law (1.21), where the remote strain \mathbf{E}_∞ concentrates into the inclusion strain $\boldsymbol{\varepsilon}_i$, implying the strain concentration tensor in the form:

$$\mathbf{A}_\infty = [\mathbb{I} + \mathbf{P}_i^\infty : (\mathbf{C}_i - \mathbf{C}_\infty)]^{-1}. \quad (1.31)$$

Therefore, the Eshelby problem (also referred to as matrix-inclusion problem) is essential tool for estimation of the phase strain concentration tensors of heterogeneous materials. To this end, the real material RVE has to be linked with the Eshelby problem, as discussed next.

1.3.7 Estimates of phase strain concentration tensors

In order to estimate the phase strain concentration tensors of a real microheterogeneous material with N material phases, N Eshelby problems have to be considered. The Eshelby problems are linked with the real material RVE as described next. First, for each material phase, one Eshelby problem is formulated. In other words, the properties (stiffness, shape, and orientation) of the i -th material phase are transferred to the inclusion of the i -th Eshelby problem. Then, the stiffness of the infinite matrices of all Eshelby's problems are set equal to a representative stiffness property of the real RVE. This is determined based on the interaction of the material phases and on the morphology of the microstructure. There are two distinct morphology types.

- Matrix-inclusion-type morphology has the stiffness of the infinite matrix \mathbf{C}_∞ equal to the stiffness of the RVE-related matrix phase (Zaoui, 2002). This approach is usually referred to as the Mori-Tanaka scheme (Benveniste, 1987).
- Polycrystalline morphology is characterized by a disordered arrangement of phases which are in direct mutual interaction. In this case, the stiffness of the infinite matrix \mathbf{C}_∞ is equal to the stiffness of the homogenized RVE \mathbf{C}_{hom} . This approach is usually referred to as the self-consistent scheme (Hershey, 1954).

As the next step, link between the loading of the infinite matrix in Eshelby problem \mathbf{E}_∞ and the loading of the real RVE of the microheterogeneous material is established. To this end,

Eq. (1.29) is formulated N times for N material phases, such that N inclusions strains from Eq. (1.29) are equal to the estimates of the N real average phase strains (1.7):

$$\mathbf{E} = \sum_{i=1}^N f_i \boldsymbol{\varepsilon}_i = \sum_{i=1}^N f_i [\mathbb{I} + \mathbf{P}_i^\infty : (\mathbf{C}_i - \mathbf{C}_\infty)]^{-1} : \mathbf{E}_\infty. \quad (1.32)$$

Solving Eq. (1.32) for \mathbf{E}_∞

$$\mathbf{E}_\infty = \left[\sum_{i=1}^N f_i [\mathbb{I} + \mathbf{P}_i^\infty : (\mathbf{C}_i - \mathbf{C}_\infty)]^{-1} \right]^{-1} : \mathbf{E}, \quad (1.33)$$

and inserting it into Eq. (1.29) yields an estimate of the phase strain concentration tensor:

$$\boldsymbol{\varepsilon}_i = [\mathbb{I} + \mathbf{P}_i^\infty : (\mathbf{C}_i - \mathbf{C}_\infty)]^{-1} : \left[\sum_{j=1}^N f_j [\mathbb{I} + \mathbf{P}_j^\infty : (\mathbf{C}_j - \mathbf{C}_\infty)]^{-1} \right]^{-1} : \mathbf{E}. \quad (1.34)$$

Comparing Eq. (1.34) with the phase strain concentration law (1.21) delivers phase strain concentration tensor

$$\mathbf{A}_i = [\mathbb{I} + \mathbf{P}_i^\infty : (\mathbf{C}_i - \mathbf{C}_\infty)]^{-1} : \left[\sum_{j=1}^N f_j [\mathbb{I} + \mathbf{P}_j^\infty : (\mathbf{C}_j - \mathbf{C}_\infty)]^{-1} \right]^{-1}. \quad (1.35)$$

Finally, inserting the latter into Eq. (1.16) yields the sought estimate of the homogenized stiffness:

$$\mathbf{C}_{hom} = \sum_{i=1}^N f_i \mathbf{C}_i : [\mathbb{I} + \mathbf{P}_i^\infty : (\mathbf{C}_i - \mathbf{C}_\infty)]^{-1} : \left[\sum_{j=1}^N f_j [\mathbb{I} + \mathbf{P}_j^\infty : (\mathbf{C}_j - \mathbf{C}_\infty)]^{-1} \right]^{-1}. \quad (1.36)$$

Eq. (1.36) accounts for four key characteristic features of a microheterogeneous material: phase shapes and orientations, phase interactions, phase volume fractions, as well as elastic stiffness of the material phases.

1.4 Main objectives of the research

The knowledge gaps identified in the previous text are closed by means of methods provided by continuum micromechanics and experimental mechanics. In this context, the objectives can be divided into two parts: (i) experimental campaign, and (ii) micromechanical modeling. As regards the former, the attention is drawn to grid nanoindentation, ultrasonic pulse transmission technique, and compressive strength tests, as described in the following.

- **Grid nanoindentation:**

In order to obtain information on the microstructure behavior, the focus is put on the grid nanoindentation. In particular, stiffnesses of the individual material constituents are of interest as these are the essential input parameters for quantifying upper and lower stiffness bounds as well as simple stiffness homogenization approach.

- **Ultrasonic pulse transmission technique:**

This technique is used for characterization of macroscopic (“homogenized”) stiffness. In comparison to the conventional unloading experiments, the ultrasonic pulse transmission technique is convenient when dealing with small specimens. This is typically the case when testing dental cement pastes.

- **Compressive strength test:**

Broadly adopted standard for compressive strength tests of cementitious dental materials, ISO 9917:1-2007, recommends molds with inner length and diameter equal to 6 mm and 4 mm, respectively. Even if the specimens are prepared perfectly, i.e. their dimensions are identical to the inner cavity of the mold, their length-to-diameter ratio is smaller than two. This suggests, that such tests account for structural effect rather than material property (Karte et al., 2015; Ausweger et al., 2019). For a meaningful explanation of strength at microscopic scale, the genuine *uniaxial* compressive strength of the investigated material is required.

As regards the modeling part, the focus is put on simple micromechanical modeling, which is the cornerstone for more sophisticated model that accounts for continuous stiffness distribution of the two population of hydrates. This model is also used for explanation of the compressive strength at microscopic scale, as described next.

- **Simple micromechanical modeling:**

The classical Voigt and Reuss stiffness bounds (Zaoui, 2002) as well as a simple stiffness upscaling model in a self-consistent form (Hershey, 1954; Hill, 1965b) provide fast and robust plausibility check between the “microstructural” elastic properties, probed by nanoindentation tests, and the “macroscopic” elastic properties obtained from ultrasound experiments.

- **Improved model for stiffness upscaling:**

In order to upscale the stiffness of mature dental cement paste, the micromechanical model uses probability density functions describing lognormal microstiffness distributions of the two populations of hydrates as an input. Moreover, the micromechanical performance of this improved model is compared with a classical model in which each material constituent is represented by one constant stiffness value.

- **Explanation of compressive strength:**

In order to explain the reason for failure of the dental cement paste at the micromechanical scale, the stiffness homogenization model from previous step is exploited here; in particular, its ability of the top-down stress quantification. This feature is used for establishing quantile-based correlations between the statistically distributed indentation modulus and equivalent shear strength, a quantity stemming from Mohr-Coulomb failure criterion.

It is of importance to consider the basic mechanisms that have significant effects on behavior of the material. Therefore, an engineering approach, according to the principle, “*as simple as possible, as complex as necessary*” is applied, in order to obtain first insights into this extraordinary material. In this context, the models are intended to reproduce behavior of cementitious dental materials at mature ages. In particular for stiffness homogenization, this justifies the approximation of the hydrates shapes as spheres.

1.5 Outline of the thesis

The following chapters contain already published papers as well as mature paper draft which is planned to be submitted soon for publication. Chapter 2 investigates the elastic properties of dental cement paste, first, at microscale by means of grid nanoindentation technique, and second, at the macroscale by means of ultrasound experiments. Simple micromechanical

modeling provides a means to check the consistency between results obtained from these analyses. Chapter 3 presents a microelasticity model in which infinitely many material phases are introduced. This is based on the two statistical microstiffness distributions of the two population of hydrates identified from nanoindentation experiments. Next, the statistical microelasticity model is further used to examine the strain and stress fluctuations inside the hydration products by means of probability density functions of the volumetric and deviatoric strain and stress concentration tensor components. These findings on strength fluctuations are further exploited in Chapter 4 for a detailed micromechanical explanation of the failure behavior of mature dental cement paste. In this context, compressive strength tests of cylindrical specimens are carried out in order to obtain genuine uniaxial compressive strength. Finally, the thesis is summarized, concluded, and completed with a future outlook in Chapter 5.

Chapter 2

Micromechanics of dental cement paste

Authored by: Petr Dohnalík, Bernhard L.A. Pichler, Luis Zelaya-Lainez, Olaf Lahayne, Gilles Richard, Christian Hellmich

Published in: *Journal of the Mechanical Behavior of Biomedical Materials*,
DOI: 10.1016/j.jmbbm.2021.104863, 2021

The final publication is available at:
<https://doi.org/10.1016/j.jmbbm.2021.104863>

Abstract: Biodentine is a calcium silicate/calcium carbonate/zirconium dioxide/water-based dental replacement biomaterial, significantly outperforming the stiffness and hardness properties of chemically similar construction cement pastes. We here report the first systematic micromechanical investigation of Biodentine, combining grid nanoindentation with ultrasonic testing and micromechanical modeling. Histograms of nanoindentation-probed hardness and elastic modulus, comprising more than 5700 values each, are very well represented by the superposition of three log-normal distributions (LNDs). Most of the data (74%) belong to the intermediate LND, representing highly dense calcite-reinforced hydration products with on-average more than 60 GPa elastic modulus and 3 GPa hardness. The remaining data refer, on the one hand, to lower density hydration products, and on the other hand, to single-micron-sized unhydrated clinker and zirconium-dioxide inclusions. Micromechanical homogenization of these three material phases delivers elastic properties of the overall cement paste material, which significantly exceed those probed by more than 300 ultrasonic tests performed in the kHz and MHz regime. This indicates the presence of micro-defects, which slightly weaken the otherwise highly optimized biomaterial system.

Contribution: Petr Dohnalík: Investigation, Methodology, Formal analysis, Software, Visualization, Writing – review & editing. Bernhard L.A. Pichler: Supervision, Conceptualization, Funding acquisition, Methodology, Formal analysis, Writing – original draft, Writing – review & editing. Luis Zelaya-Lainez: Investigation, Methodology, Visualization. Olaf Lahayne: Investigation, Methodology. Gilles Richard: Conceptualization, Funding acquisition, Resources, Writing – review & editing. Christian Hellmich: Conceptualization, Funding acquisition, Methodology, Formal analysis, Supervision, Writing – original draft, Writing – review &

editing.

Keywords: Dental cement, Nanoindentation, Ultrasound, Micromechanics, Calcite-reinforced hydrates

2.1 Introduction

Dental cement pastes need to be workable for a few minutes after mixing, and to harden quickly thereafter. Moreover, their biocompatibility with enamel, dentin, and pulp is required, while their mechanical strength needs to allow for physiologically relevant biting (Primus et al., 2019).

Accordingly, they typically exhibit strength values exceeding those of chemically similar construction cements, with Biodentine™ (Septodont, Saint-Maur-des-Fossés, France) reaching some 300 MPa uniaxial strength (Butt et al., 2014). However, different from the situation with construction cements, the micromechanical performance of dental cements, i.e. the contribution of the material’s individual constituents to its overall mechanical behavior, has hardly been studied so far. The present paper wishes to close the corresponding knowledge gap. Therefore, it is useful to recall basic properties of Biodentine first: The cement powder comes in capsules containing 0.7 grams, and its chemical composition was quantified by means of X-ray diffraction analyses with Rietveld refinement (Camilleri et al., 2013; Grazziotin-Soares et al., 2019; Li et al., 2019), see also Table 2.1: Some 74 wt% of the cement powder are made up by tricalcium silicate (Ca_3SiO_5), some 16.5 wt% by calcium carbonate (CaCO_3) acting as a filler, some 5 wt% by zirconium dioxide (ZrO_2) providing X-ray opacity (Laurent et al., 2008, 2012), and some 4.5 wt% by dicalcium silicate (Ca_2SiO_4).

Table 2.1

Composition of the dry binder of Biodentine: constituent-specific mass fractions (Li et al., 2019), masses in one capsule containing 0.7 g of powder, and mass densities (Lavergne et al., 2018; Kyocera Group, 2019).

index i	constituent	mass fraction [wt%]	mass in one capsule [mg]	mass density [kg/m ³]
1	Ca_2SiO_4	4.45	31.15	3270
2	Ca_3SiO_5	73.80	516.60	3150
3	CaCO_3	16.60	116.20	2710
4	ZrO_2	5.15	36.05	5600
	sums	100.00	700.00	

The mixing liquid of “Biodentine” comes in tubes containing approximately 200 microliters. This liquid consists of water, a modified polycarboxylate polymer acting as a superplasticizer, and calcium chloride (CaCl_2) accelerating the setting reaction (Laurent et al., 2012).

Herein, we resort to grid nanoindentation testing (Constantinides et al., 2006; Constantinides and Ulm, 2007; Ulm et al., 2007), in order to probe the material at maximum indentation depths h_{max} of around 100 nm. The correspondingly derived elastic and hardness properties relate to representative material volume elements (RVEs) the characteristic size of

which follows as (Jagsch et al., 2020):

$$\ell_{\text{RVE}}^{\text{NI}} \in \left[\frac{h_{\text{max}}}{3}; \frac{h_{\text{max}}}{2} \right] = [33; 50] \text{ nm}. \quad (2.1)$$

Hence, our nanoindentation tests do not characterize the overall hardened dental cement paste, but rather its micromechanical phases, such as unhydrated clinker grains or different hydration products. In order to precisely screen corresponding phase properties, we perform thousands of nanoindentation tests, and we represent histograms of elasticity and hardness as the superposition of phase-specific log-normal distributions. In this way, we consider *a priori* the positive definiteness of the probed mechanical properties (Pichler et al., 2005). The relevance of this strategy is then checked through complementary investigations:

- Microscopic images give direct access to characteristic particle sizes within the microstructure;
- ultrasonic tests in the kHz to MHz frequency regime detect the “macroscopic” elastic properties of Biodentine hardened cement paste at an RVE-size $\ell_{\text{RVE}}^{\text{US}}$ in the order of tens of micrometers; and
- micromechanical modeling, both in a self-consistent form (Hershey, 1954; Hill, 1965b) as well as in terms of the classical Voigt and Reuss stiffness bounds (Zaoui, 2002), provides a means to check the consistency between the “microstructural” elastic properties probed by nanoindentation tests and their ultrasound-derived “macroscopic” counterparts.

Along these lines, the present paper is structured as follows: Section 2.2 refers to materials and methods, Section 2.3 to results, Section 2.4 to the discussion of the obtained results, and Section 2.5 to the conclusions drawn from the present study.

2.2 Materials and methods

2.2.1 Sample preparation

Biodentine cement pastes were produced according to the instructions of the manufacturer. Capsules containing the dry binder power were opened, five droplets of the liquid were dripped onto the binder, and then the capsules were closed and shaken in the amalgamator for 30 seconds. After mixing, the capsules were removed from the amalgamator and opened.

For grid nanoindentation testing, the freshly produced material was taken out of the capsule with a spatula and formed into a cuboidal shape with dimensions $12 \times 7 \times 3 \text{ mm}^3$. This cuboidal specimen was allowed to harden for four months, at room temperature and exposed to the ambient air. We note that this led to the formation of a carbonated layer at the outer surface of the specimen. Hence, it was important to follow a protocol which effectively prevents any adverse effects of this layer. Accordingly, the following steps were taken:

First, the cuboidal specimen was fixed, by means of the two component polyurethane glue WIKO Repair 90 (Gluetec, Germany), onto a glass plate for further processing. The top surface of the well-hardened specimen was first ground by hand and subsequently polished by means of a PM5 precision polishing machine (Logitech, Scotland), operated for 20 hours at 40 to 50 revolutions per minute, using silicon carbide (SiC) grinding paper with a grain size of $5 \mu\text{m}$. This treatment reduced the thickness of the specimen from 3 mm to 1.5 mm, implying the removal of all the material which was negatively affected by air curing. Conclusively, the

nanoindentation tests were performed on the surface of a material which was similar to that tested ultrasonically.

Namely, for ultrasonic testing, the freshly produced material was cast into seven cylindrical plastic molds of 5 mm diameter and 10 mm height, with the top and the bottom bases of the cylinders being covered by plexiglass. The filled molds remained, for at least 15 minutes and for at most two hours, in a temperature chamber at 37°C. Thereafter, the specimens were demolded, and conditioned in lime-saturated solution, again at 37°C. The specimens were taken out of this solution for ultrasonic testing only.

2.2.2 Roughness testing protocol

Employing the Scanning Probe Microscopy (SPM) mode of the Hysitron Triboindenter TI-900, Bruker, USA, the root-mean-squared average roughness R_q was quantified as (Miller et al., 2008)

$$R_q = \sqrt{\frac{1}{P^2} \sum_{m=1}^P \sum_{n=1}^P z_{mn}^2}, \quad (2.2)$$

where z_{mn} is the distance between the surface at position (m, n) and the mean plane of the scanned surface. P^2 is the number of scanned positions within a quadratic testing area with 50 μm side length, scanned along a regular grid of 256 \times 256 measurement points. The surface probed herein was characterized by

$$R_q = 18 \text{ nm}, \quad (2.3)$$

see Fig. 2.1. The average roughness R_q sets a minimum requirement for the maximum

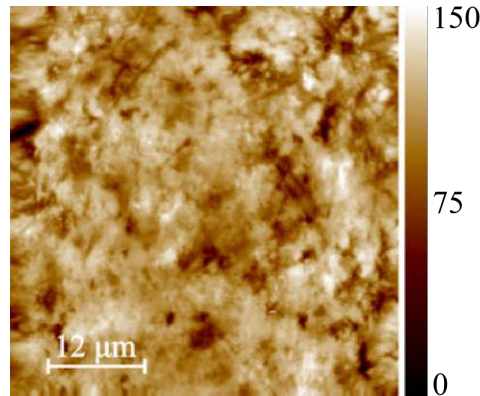


Fig. 2.1. Scanning probe microscopic image showing polished surface of hardened dental cement paste; heights are given in nm, and resolved down to a pixel size of 195 nm.

indentation depth needed to allow for reasonable determination of hardness and elastic modulus from the Oliver-Pharr solution for a Berkovich tip pressed into the surface of an elasto-plastic halfspace (Oliver and Pharr, 1992). Namely, the maximum indentation depth needs to amount to at least 2.5 times the roughness (see page 432 of Donnelly et al. (2006); and Fig. 8 of Miller et al. (2008))

$$h_{\max} \geq 2.5 R_q = 45 \text{ nm}, \quad (2.4)$$

where also use of Eq. (2.3) was made. Out of the 5748 indentation tests performed according to the protocol described in the subsequent subsection, only two were associated with maximum indentation depths smaller than 45 nm; hence, the roughness requirement was virtually always fulfilled.

2.2.3 Grid nanoindentation protocol

5748 indentation tests along a grid with a typical spacing of 70 μm were performed. Given that this spacing is considerably larger than the typical indentation depth of 139 nm, the indentation results can be regarded as being totally independent of each other.

All indentation tests were performed under force control, prescribing the history depicted in Fig. 2.2(a). This force history resulted in typical load-displacement curves as the one shown in Fig. 2.2(b). Such curves allow for hardness and elastic property determination. In

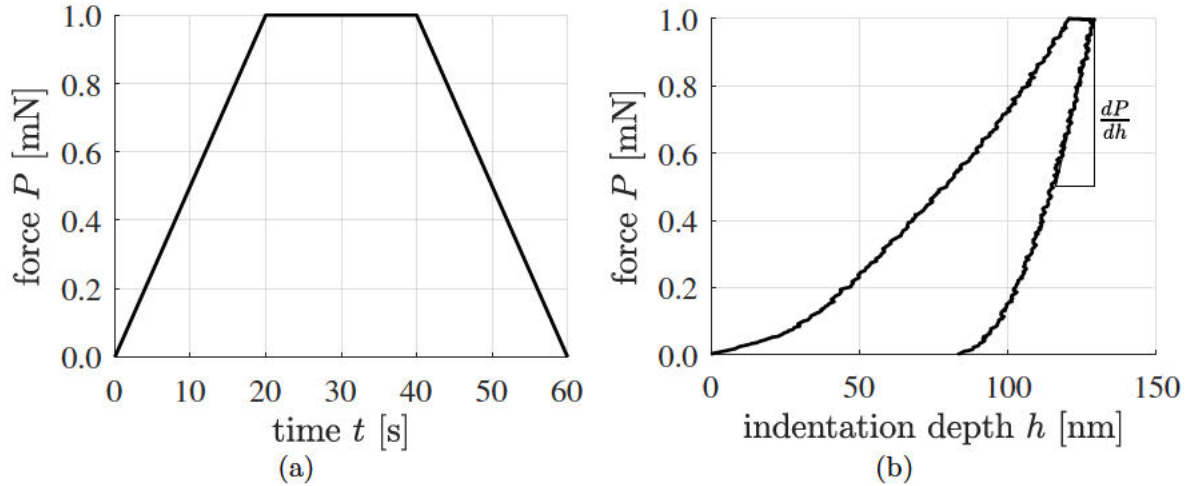


Fig. 2.2. (a) Force history prescribed during all 5748 individual nanoindentation experiments, and (b) force-displacement diagram representing the result of a single nanoindentation experiment.

more detail, the maximum load P_{max} divided by the corresponding projected contact area A yields the hardness H ; mathematically reading as (Oliver and Pharr, 1992)

$$H = \frac{P_{\text{max}}}{A}, \quad (2.5)$$

whereby the contact area depends quadratically on the contact indentation depth according to (Oliver and Pharr, 1992)

$$A = 24.5 h^2. \quad (2.6)$$

The slope of the unloading branch gives access to the indentation modulus M , according to (Oliver and Pharr, 1992)

$$M = \frac{1}{2} \sqrt{\frac{\pi}{A}} \left. \frac{dP}{dh} \right|_{h=h_{\text{max}}}. \quad (2.7)$$

The indentation modulus is a function of the elastic stiffness properties of the probed domain and of the diamond tip of the indenter. For an isotropic domain, the aforementioned function reads as (Oliver and Pharr, 1992)

$$\frac{1}{M} = \frac{1 - \nu^2}{E} + \frac{1 - 0.07^2}{1141 \text{ GPa}}. \quad (2.8)$$

In Eq. (2.8), ν and E stand for Poisson's ratio and the elastic modulus of the probed domain, while 0.07 and 1141 GPa are the corresponding stiffness properties of the diamond tip.

2.2.4 Statistical evaluation of nanoindentation test results

The data sets of hardness and modulus values, respectively, are represented in terms of histograms. For choosing appropriate bin widths, we resort to the Freedman-Diaconis rule (Freedman and Diaconis, 1981),

$$b_X^{FD} = 2 \text{IQR}(X) N_i^{-\frac{1}{3}}, \quad X = M, H, \quad (2.9)$$

where $N_i = 5746$ stands for the total number of measurements represented by the histogram and $\text{IQR}(X)$ stands for the interquartile range of the hardness or modulus data set, respectively. Based on the numbers suggested by the Freedman-Diaconis rule, the actually chosen bin widths are

$$b_M = 2 \text{ GPa}, \quad (2.10)$$

and

$$b_H = 0.15 \text{ GPa}. \quad (2.11)$$

The central value X_i of each of these bins reads as

$$X_i = (i - 1) \times b_X + \frac{b_X}{2}, \quad i = 1, 2, \dots, N_b, \quad X = M, H. \quad (2.12)$$

with $N_b = 100$ being the total number of histogram bars. The number of indents associated with each specific histogram bar is translated into a corresponding probability value, so that the sum of the areas of all bars belonging to one histogram is equal to 1. Hence, the experimentally obtained probability associated with the i^{th} histogram bar reads as

$$P^{exp}(X_i) = \frac{x_i}{N_i b_X}, \quad X = M, H, \quad (2.13)$$

where x_i denotes the number of experimental results found in the interval $X_i \pm \frac{b_X}{2}$.

The experimentally determined probability distributions Eq. (2.13) are approximated by the superposition of log-normal distributions; mathematically, this approximation reads as

$$P^{app}(X) = \sum_{c=1}^C f_c P_c^{log}(X, \mu_{X,c}; \sigma_{X,c}), \quad X = M, H, \quad (2.14)$$

with the log-normal distributions reading as

$$P_c^{log}(X; \mu_{X,c}, \sigma_{X,c}) = \frac{1}{X \sigma_{X,c} \sqrt{2\pi}} \exp\left(-\frac{1}{2} \left[\frac{\ln(X) - \mu_{X,c}}{\sigma_{X,c}}\right]^2\right), \quad X > 0. \quad (2.15)$$

and with the weights f_c fulfilling the side condition

$$\sum_{c=1}^C f_c = 1. \quad (2.16)$$

The weights are equal to the area fractions of the constituents of the nanoindentation-probed microheterogeneous material. Given a highly disordered microstructure of a macroscopically isotropic material, and a grid nanoindentation testing campaign that probes an area which is statistically representative for the analyzed microheterogeneous material, the weights are also equal to the volume fraction of the constituents (Constantinides and Ulm, 2007), i.e. the

ratio of the volume occupied by a specific constituent, V_c , divided by the total volume of the composite

$$f_c = \frac{V_c}{\sum_{j=1}^C V_j} \quad c = 1, 2, \dots, C. \quad (2.17)$$

The median and mode values, denoted as $\text{Md}(X_c)$ and $\text{Mo}(X_c)$, are related to the log-normal parameters $\mu_{X,c}$ and $\sigma_{X,c}$ through

$$\text{Md}(X_c) = \exp(\mu_{X,c}), \quad (2.18)$$

$$\text{Mo}(X_c) = \exp\left(\mu_{X,c} - \sigma_{X,c}^2\right). \quad (2.19)$$

The approximation according Eq. (2.14) to Eq. (2.16) is realized by minimizing the following square root of the sum of squared errors:

$$\varepsilon_{SRSS} = \sqrt{\frac{1}{2N_b} \sum_{X=M,H} \sum_{i=1}^{N_b} \left[P^{exp}(X_i) - P^{app}(X_i) \right]^2} \rightarrow \min. \quad (2.20)$$

The optimization problem defined by Eqs. (2.13)–(2.20) is solved iteratively, based on search intervals that are progressively refined and shifted, see [Appendix 2.A](#) for details.

2.2.5 Light microscopy imaging of polished surfaces

The ultrasonically tested specimens were embedded into epoxy resin, before being cut, polished, and cleaned in an ultrasonic bath. Color as well as black-and-white images of 2584×1936 pixels and 1292×968 pixels, respectively, with pixel sizes ranging from 0.34 to 0.54 microns, were taken by a Zeiss AxioCam MRc5 camera connected to a light microscope Zeiss Axio Imager Z1m. The images were postprocessed by Software ImageJ, in terms of a threshold-based conversion into binary images revealing a matrix-inclusion morphology.

2.2.6 Ultrasonic pulse transmission

The non-destructive ultrasonic pulse transmission technique, based on longitudinal waves, is used for the characterization of the macroscopic “effective” (or homogenized) elastic stiffness of the composite Biodentine. The test setup consists of a serial arrangement of a pulse generator, a layer of honey (= coupling medium), a plastic foil, the specimen, another plastic foil, another layer of honey, and a pulse detector, see [Fig. 2.3](#). The plastic foils ensure that the coupling medium does not penetrate in the potentially open porosity of the tested sample. The setup is placed inside a temperature chamber conditioned to 37°C .

According to the theory of wave propagation through isotropic and linearly elastic media (Carcione, 2007; Achenbach, 1973), the component C_{1111} of the elastic stiffness tensor is equal to the product of the investigated material’s mass density ρ and the velocity v of longitudinal waves propagating through the sample (Kohlhauser and Hellmich, 2012; Carcione, 2007; Achenbach, 1973),

$$C_{1111} = \rho v^2. \quad (2.21)$$

The wave velocity is equal to the height of the tested specimen b divided by the time of flight t_f of the ultrasonic pulse through the tested specimen,

$$v = \frac{b}{t_f}. \quad (2.22)$$

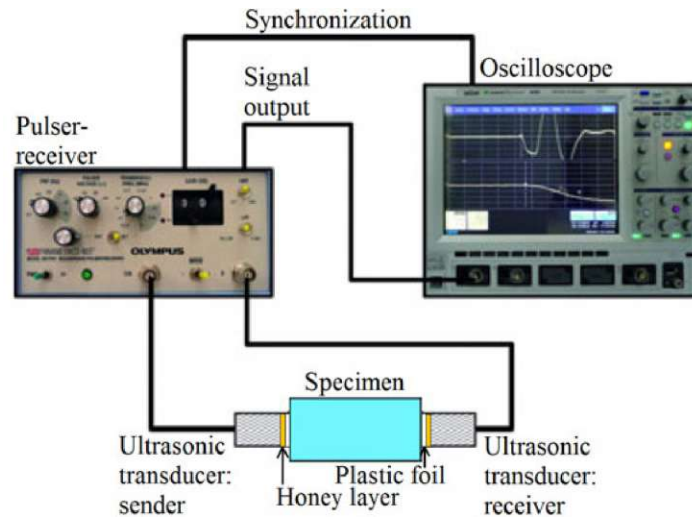


Fig. 2.3. Setup of the ultrasonic pulse transmission tests, consisting of ultrasonics transducers (Olympus PR5077), the tested specimen, honey layers as coupling medium, plastic foils separating the specimen from the honey layers, and a digital oscilloscope (Wave Runner 62Xi); source: (Kohlhauser, 2009).

t_f cannot be directly measured, but results from the difference of two other time measurements,

$$t_f = t_{tot} - t_d, \quad (2.23)$$

where t_{tot} is the travel time of the pulse from the transducer – through the coupling medium, the plastic foils, *and* the specimen – to the receiver, while the delay time t_d is needed by the pulse to just travel from the generator, through honey and plastic foils (but without specimen), to the receiver. In total, 325 tests were performed at material ages from 7 to 28 days, using longitudinal transducers with excitation frequencies amounting to 50 kHz, 500 kHz, 1 MHz, 2.25 MHz, 5 MHz, 10 MHz, and 20 MHz, see Table 2.2.

Table 2.2

Ultrasonic longitudinal wave transducers used for characterization of hardened Biodentine.

Frequency [MHz]	Longitudinal transducer
0.05	X1021
0.5	V101-RB
1	C602-RB
2.25	C604-RB
5	C109-RM
10	V112-RM
20	V116-RM

The mass density of hardened Biodentine was determined specimen-per-specimen, and on every measurement day. The mass of every specimen, determined using a digital scale (Kern & Sohn GmbH, PCB 2400-2B), was divided by the volume $V = b a^2 \pi/4$, where the diameter a and the length b of the cylindrical specimens were measured using a digital sliding caliper.

Ultrasonic waves characterize material volumes with characteristic lengths which need to be by at least a factor of ten smaller than the wavelength λ (Kohlhauser and Hellmich, 2013). Anticipating wave velocities in the order of $v = 5$ km/s, see Fig. 2.7 (a), fairly independent of the frequency of the applied signals, we obtain

$$\begin{aligned}\min \lambda &= \frac{v}{\max f} = \frac{5000 \text{ m/s}}{20 \times 10^6 \text{ Hz}} = 0.00025 \text{ m}, \\ \max \lambda &= \frac{v}{\min f} = \frac{5000 \text{ m/s}}{0.05 \times 10^6 \text{ Hz}} = 0.1 \text{ m},\end{aligned}\quad (2.24)$$

$$\ell_{\text{RVE}}^{\text{US}} \in \left[\frac{\min \lambda}{10}; \frac{\max \lambda}{10} \right] = [0.025; 10] \text{ mm} \gg \ell_{\text{RVE}}^{\text{NI}} \in [33; 50] \text{ nm}, \quad (2.25)$$

where use of Eq. (2.1) was made. We see that the nanoindentation-probed material volumes with characteristic length $\ell_{\text{RVE}}^{\text{NI}}$ appear as microheterogeneities in the much larger ultrasonics-probed material volumes with characteristic length $\ell_{\text{RVE}}^{\text{US}}$. We note in passing that the scale separation requirement (2.25) between nanoindentation-probed microheterogeneities and ultrasonics-probed homogenized material volume is largely overfulfilled: A corresponding factor of two to three normally suffices for spherical microheterogeneities (Drugan and Willis, 1996; Pensée and He, 2007), while a larger factor of four to fourteen is needed in case fiber networks (Shahsavari and Picu, 2013).

2.2.7 Micromechanical stiffness bounds and estimates

Methods of continuum micromechanics (Zaoui, 2002) provide access to bounds and estimates of the homogenized “effective” stiffness of RVEs of microheterogeneous materials, see Appendix 2.B. As for their numerical application to the investigated material, the volume fractions of freshly mixed Biodentine, f_c , were determined from the following compositional analysis, based on the data from Table 2.1 for the dry binder components and on the following mass and volume measurements on the mixing liquid: The mass of five droplets of the mixing liquid, m_5 , was quantified based on three individual measurements of the liquid in an Eppendorf tube using advanced level balance (Mettler Toledo PG403-S, Switzerland):

$$m_5 = 193.0 \pm 6.2 \text{ mg}. \quad (2.26)$$

The mass density of the mixing liquid, ρ_5 , was determined from measuring the mass of a tip detached from a micropipette, before and after aspirating 100 μL of the mixing liquid into the tip. The mass of 100 μL of the mixing liquid amounts to 147.2 ± 3.7 mg, which divided by the known volume yields the mass density of the mixing liquid as

$$\rho_5 = 1.472 \pm 0.037 \text{ mg/mm}^3. \quad (2.27)$$

The volume fractions of the individual constituents of freshly mixed Biodentine are equal to the volume occupied by the individual constituents divided by the sum of volumes of all constituents. Expressing volumes as masses divided by mass densities, yields, by analogy to Eq. (2.17),

$$f_i = \frac{m_i}{\sum_{j=1}^5 \frac{\rho_i}{\rho_j} m_j}, \quad i = 1, 2, \dots, 5, \quad (2.28)$$

see Table 2.3. The initial volume fractions of the chemically inert calcite, 12.12%, and zirconium dioxide, 1.82%, are constant throughout the hardening process. Thus, they are also valid for hardened Biodentine.

Table 2.3

Composition of freshly mixed Biodentine: constituent-specific masses in one capsule containing 0.7 g of powder (see also Table 2.1), mass densities (see also Table 2.1), and volume fractions.

index i	constituent	mass m_i [mg]	mass density ρ_i [mg/mm ³]	volume fraction** f_i [%]
1	Ca ₂ SiO ₄	31.15	3.270	2.69
2	Ca ₃ SiO ₅	516.60	3.150	46.33
3	CaCO ₃	116.20	2.710	12.12
4	ZrO ₂	36.05	5.600	1.82
5	Liquid	193.00*	1.472*	37.04
sums		893.00		100.00

* this study, see Eqs. (2.26) and (2.27)

** see Eq. (2.28)

2.3 Results

The probability density function representing the 5746 nanoindentation test results fulfilling requirement (2.4) can be very well represented by means of the superposition of three log-normal distributions (LNDs) [i.e. $C = 3$ in Eq. (2.14)], as is underlined by an error according to Eq. (2.20), which is as low as 1.25×10^{-3} ; see Fig. 2.4. According to the increasingly high numbers associated to these LNDs, the latter are referred to as “low LND”, “medium LND”, and “high LND”; and the corresponding median and mode values are given in Table 2.4.

Table 2.4

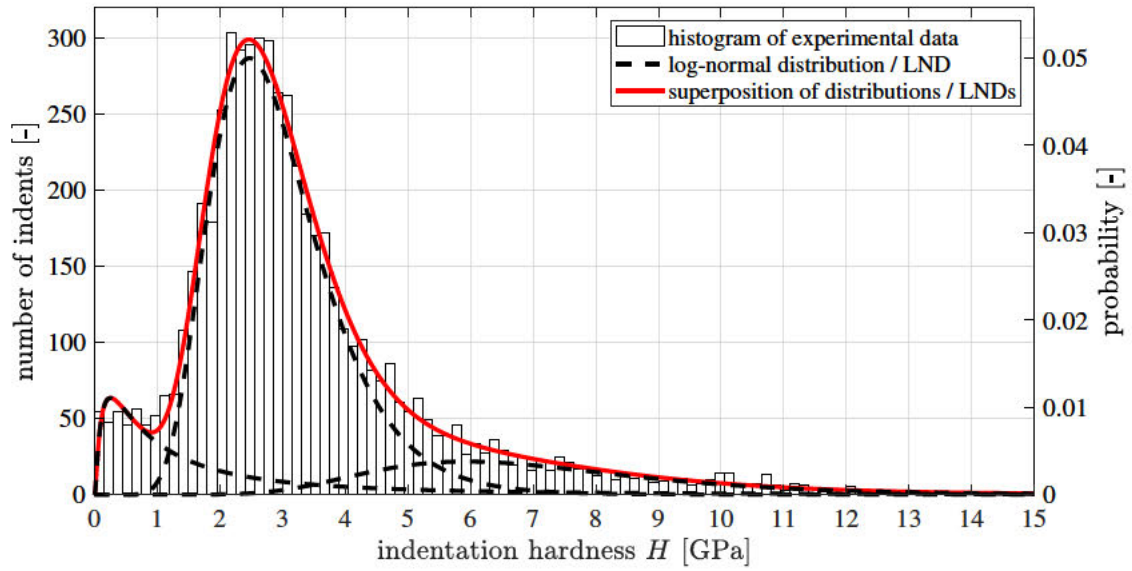
Approximation of $N_i = 5746$ indentation test results through log-normal distributions, three each for hardness and modulus data.

statistical sub-sample	Md(M) [GPa]	Md(H) [GPa]	Mo(M) [GPa]	Mo(H) [GPa]	volume fraction f [-]
low LND	45.1	1.15	24.5	0.26	0.1228
medium LND	62.6	2.78	60.2	2.47	0.7420
high LND	92.2	6.66	89.0	5.93	0.1352
sum:					1.0000

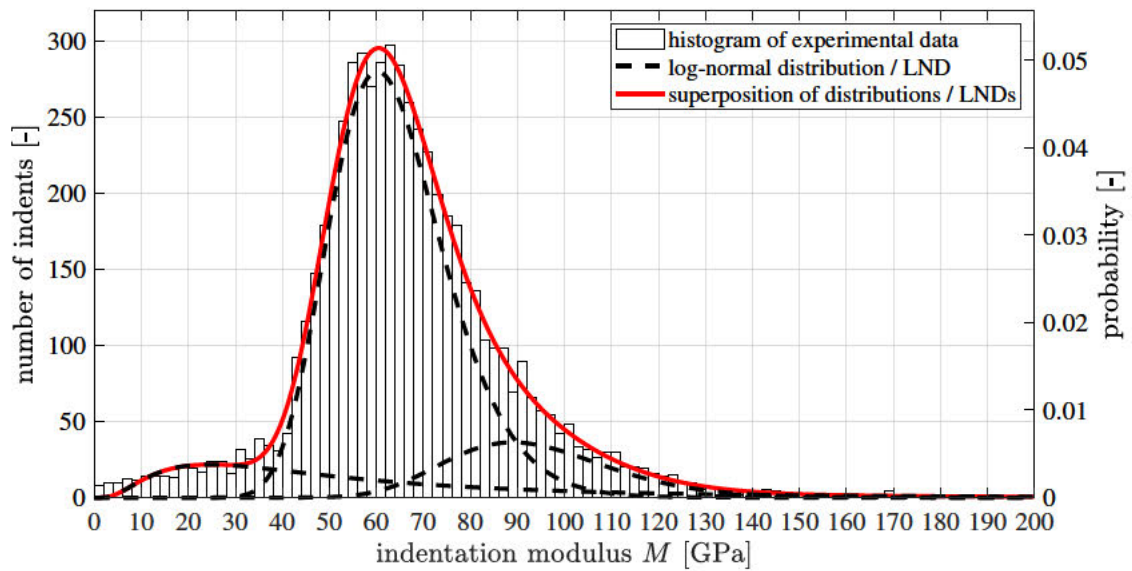
It is interesting to relate the three domains defined by the nanoindentation results of Table 2.4, to the light microscopic images taken according to Section 2.2.5, see Figs. 2.5 and 2.6, and to the mechanical properties of calcite, cement clinker, and zirconium dioxide.

Figs. 2.5 (b) shows black inclusions with a binary-image-derived volume fraction of 1.3% and a mean size of 10.7 μm , embedded in an overall “matrix”. These inclusions qualify as air pores. Given their low volume fraction, they are not represented as a distinctive LND in Table 2.4 or Fig. 2.4.

The median values of the modulus and the hardness of the high LND, $\text{Md}(M) = 92.2$ GPa and $\text{Md}(H) = 6.66$ GPa, see Table 2.4, are larger than the mechanical properties of calcite: $M = 85.8$ GPa and $H = 4.6$ GPa, see Lavergne et al. (2018); Merkel et al. (2009), and



(a)



(b)

Fig. 2.4. Approximation of histograms by the superposition of three log-normal distributions: (a) hardness, (b) indentation modulus.

smaller than those of cement clinker $M = 125$ GPa and $H = 9.2$ GPa, see Constantinides and Ulm (2007). Notably, zirconium dioxide is even stiffer and stronger than cement clinker. Considering that a nanoindentation test may well probe the mechanical behavior of both a sufficiently small, stiff inclusion and its much softer environment (Königsberger et al., 2021), see also Section 2.4.4 for a more detailed discussion of this aspect, we conclude that the high LND must refer to cement clinker and zirconium dioxide.

This conclusion is further confirmed by an additional plausibility check: Fig. 2.6 (b) shows black inclusions embedded in an overall “matrix”, with a mean particle size of $4.3 \mu\text{m}$ and a binary-image-derived volume fraction of 12.1%. Considering that these particles are residual cement clinker, and adding to their image-derived volume fraction (12.1%) that of zirconium dioxide: 1.8%, see Table 2.3, yields 13.9%. This value is remarkably close to 13.5%, which is the volume fraction associated with the high LND in Table 2.4.

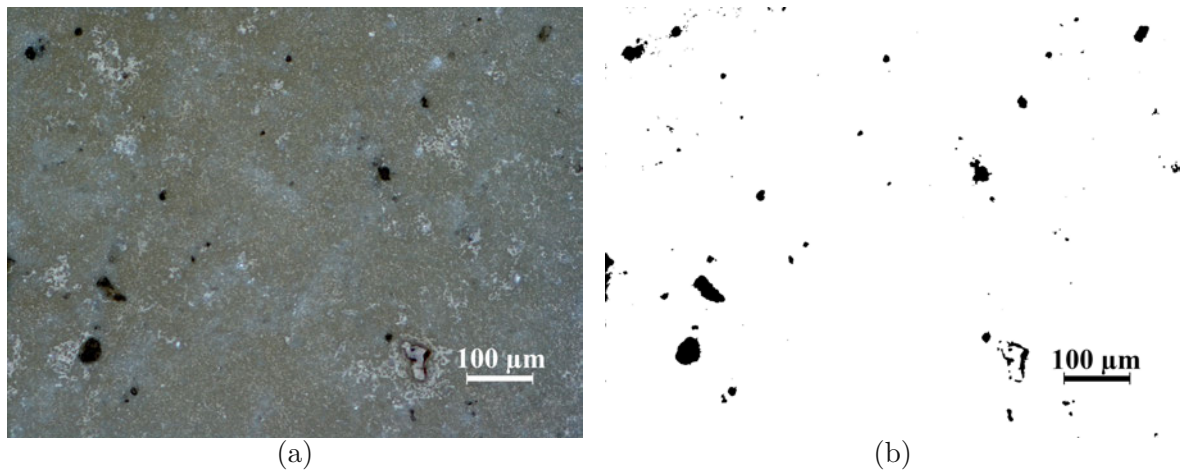


Fig. 2.5. (a) Color light microscopy image of a polished surface of hardened Biodentine, with pixel size amounting to $0.54 \mu\text{m}$: air pores appear as black spots; they comprise 1.3% of the image, as quantified from a thresholded binary image (b).

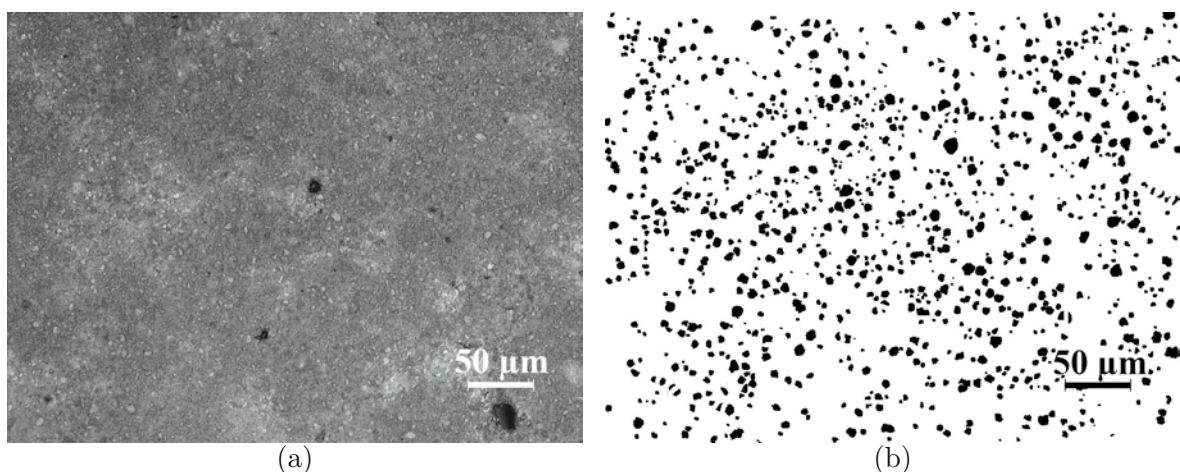


Fig. 2.6. (a) Black-and-white light microscopy image of a polished surface of hardened Biodentine, with pixel size amounting to $0.34 \mu\text{m}$, remnants of unhydrated clinker appear in light grey; they comprise 12.1% of the image, as quantified from a thresholded binary image (b).

The mechanical behavior of this material around the stiff inclusions is very well represented by two log-normal distributions, the medium LND and the low LND of Table 2.4. This reveals the existence of two types of hydrates reinforced by calcite particles of single-to-sub-micrometric size (Li et al., 2019). The medium LND refers to a high-density version of these calcite-reinforced hydrates, while the low LND refers to a less dense version. The existence of two types of structurally different, but compositionally similar hydrate phases is reminiscent of the so-called *inner products* and *outer products* known from construction cements (Taplin, 1959). They are also referred to as *low-density calcium-silicate-hydrates (C-S-H)* and *high-density C-S-H* (Jennings, 2000; Tennis and Jennings, 2000) and they were mechanically characterized by means of grid nanoindentation (Constantinides and Ulm, 2004). In this context, we note that it is always advisable to complement statistical nanoindentation studies by microscopic as well as chemical analyses (Lura et al., 2011; Chen et al., 2010).

At the macroscopic level of hardened Biodentine cement paste, ultrasonic and weighing/volume tests according to Section 2.2.6 reveal age- and frequency-invariant longitudinal wave velocities and mass densities, amounting to $v = 4977 \pm 191$ m/s and $\rho = 2.311 \pm 0.059$ kg/dm³, respectively, see Fig. 2.7. Thus, the expected value of the stiffness tensor component C_{1111} , see Eq. (2.21), amounts to 57.2 GPa. The corresponding RVE measuring

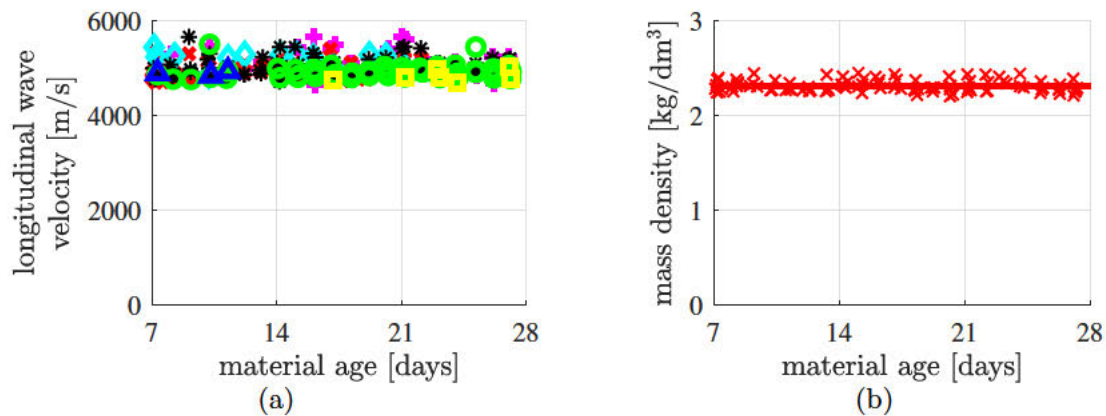


Fig. 2.7. (a) Longitudinal wave velocities v as a function of the material age ranging from 7 to 28 days after production, for different central frequencies: 50 kHz (pink '+'), 500 kHz (red 'x'), 1 MHz (cyan '◇'), 2.25 MHz (black '*'), 5 MHz (green 'o'), 10 MHz (blue '△'), 20 MHz (yellow '□'), and (b) mass density of Biodentine as a function of material age.

at least 25 microns according to Eq. (2.25) is sufficiently scale-separated from the clinker inclusion size of 4.3 microns, see Fig. 2.6; hence, the ultrasonic waves indeed characterize the homogenized properties of hardened cement paste. However, the experimental value of 57.2 GPa is significantly smaller than the micromechanical estimates derived from continuous interaction of the nanoindentation-probed hydrate and clinker phases with properties according to Table 2.5. This discrepancy, given in quantitative terms in Table 2.6, cannot be explained by the very low volume fraction of air pores seen in Fig. 2.5, and hence, indicate the presence of defects and cracks. The latter typically exhibit a negligibly low volume fraction, but induce very pronounced microstress peaks which lower the overall homogenized stiffness. This is reminiscent of somewhat similar findings from grid nanoindentation into bone (Pastrama et al., 2018; Furin et al., 2016) and steel (Jagsch et al., 2020). Notably, the micrographs of Fig. 2.6(a) do not show traces of such cracks. Correspondingly, the cracks are actually closed, so that their volume fraction is very close to zero. The effect of closed cracks on the overall material behavior cannot be traced back to their volume fraction, but requires

Table 2.5

LND-specific elastic properties (“micromechanical phase properties”) determined from the median values of Table 2.4.

material phase	indentation modulus M_c [GPa]	Poisson’s ratio ν_c [-]	elastic modulus E_c [GPa]	bulk modulus k_c [GPa]	shear modulus μ_c [GPa]
low LND: $c = 1$	45.1	0.24	44.2	28.4	17.8
medium LND: $c = 2$	62.6	0.24	62.4	40.0	25.2
high LND: $c = 3$	92.2	0.30	91.2	76.0	35.1

Table 2.6

Bounds and self-consistent estimates for homogenized stiffness component C_{1111} of hardened Biodentine, based on the phase properties of Table 2.5.

upper bound	77.6 GPa
self-consistent estimate	75.3 GPa
lower bound	73.7 GPa
effective experimental value	57.2 GPa

the introduction of other microstructural quantities, such as the crack density parameter of Budiansky and O’Connell (Budiansky and O’Connell, 1976; Pensée et al., 2002). However, quantification of the crack density, as e.g. given in greater detail in Jagsch et al. (2020), is beyond the scope of the present paper.

2.4 Discussion

2.4.1 Dental hydrates vs. construction cement hydrates

The high-density calcite-reinforced hydrates of Biodentine, with $H = 2.78$ GPa and $M = 62.6$ GPa, see Table 2.4, are significantly stronger and stiffer than hydrates of chemically similar construction cement pastes, including

- low-density (LD) C-S-H, with $H = 0.45$ GPa and $M = 18.2$ GPa, see the circle in Fig. 2.8 and Constantinides and Ulm (2007),
- high-density (HD) C-S-H, with $H = 0.83$ GPa and $M = 29.1$ GPa, see the square in Fig. 2.8 and Constantinides and Ulm (2007), as well as
- a nano-composite consisting of HD C-S-H reinforced by nanocrystals of calcium hydroxide (initially also referred to as “ultra high-density C-S-H”, see Vandamme and Ulm (2009)), with $H = 1.6$ GPa and $M = 47.2$ GPa, see the star in Fig. 2.8 and Chen et al. (2010).

The less-dense calcite-reinforced hydrates of Biodentine with $H = 1.15$ GPa and $M = 45.1$ GPa, see Table 2.4, are comparable to the calcium-hydroxide-reinforced HD C-S-H, see Fig. 2.8.

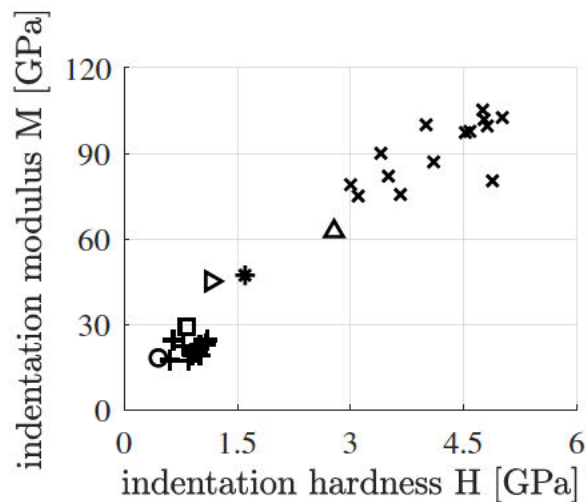


Fig. 2.8. Indentation modulus over indentation hardness of different cement hydrates including Biodentine, of human dentin, and of enamel: low-density C-S-H of construction cements ('o') (Constantinides and Ulm, 2007), high-density C-S-H of construction cements ('□') (Constantinides and Ulm, 2007), C-S-H reinforced with calcium hydroxide ('*') (Chen et al., 2010), enamel ('x') (Mahoney et al., 2000; Jeng et al., 2011; Barbour et al., 2003; Mahoney et al., 2004; Park et al., 2008), dentin ('+') (Mahoney et al., 2000; Balooch et al., 2001; Angker et al., 2003; Fränzel and Gerlach, 2009; Ziskind et al., 2011; Chan et al., 2011; Guidoni et al., 2006; Habelitz et al., 2002; Halgaš et al., 2013), and *Biodentine high-density calcite-reinforced hydrates* ('△' - median), and *Biodentine low-density calcite-reinforced hydrates* ('▷' - median) this study.

It is interesting to compare nanoindentation properties of different hydrated cementitious materials with the ones of the natural tooth materials dentin and enamel. LD and HD C-S-H have nanoindentation properties which are similar to those of dentin (Mahoney et al., 2000; Balooch et al., 2001; Angker et al., 2003; Fränzel and Gerlach, 2009; Ziskind et al., 2011; Chan et al., 2011; Guidoni et al., 2006; Habelitz et al., 2002; Halgaš et al., 2013), see Fig. 2.8. Already the less-dense calcite-reinforced hydrates are significantly stiffer and stronger than dentin. The high-density calcite-reinforced hydrates, in turn, reach almost the properties of enamel (Mahoney et al., 2000; Jeng et al., 2011; Barbour et al., 2003; Mahoney et al., 2004; Park et al., 2008), see Fig. 2.8.

2.4.2 Discussion on curing conditions

The question may arise whether the curing in limestone solution may be considered as physiologically relevant. In this context, we note that physiological testing of Biodentine is normally performed in 100 % relative humidity (Rajasekharan et al., 2014; Guneser et al., 2013), often with additional direct contact to different fluids, such as water at different pH levels, saline solution, blood, or saliva. In this context, it turned out that blood and saliva did not alter the strength of Biodentine in a statistically significant way (Subramanyam and Vasantharajan, 2017), while very low pH values did (Poplai et al., 2012). The latter fact indicates that the material is susceptible to leaching.

Curing the specimens used for ultrasonics characterization in limestone solution was motivated as follows. Air-curing leads to carbonation of the surface of the specimens. While we were able to polish away the carbonated layer from the air-cured specimens undergoing

nanindentation, carbonation of the specimens for ultrasonic characterization had to be avoided. Accordingly, they were cured in a limestone solution. This prevented both carbonation and leaching.

When it comes to suction of water into the specimens, we do not expect any difference between our sample immersion protocol and the standard “physiological” sample exposure to 100 % relative humidity (Rajasekharan et al., 2014; Gunesser et al., 2013): As a matter of fact, our own experiments have evidenced that masses of the specimens, measured directly after demolding of the cylindrical samples (without any contact to air with 100 % relative humidity or fluids) and measured after several days of immersion in limestone solution did not differ from each other by more than the measuring precision limit; the latter amounting to 0.01 gram. This is consistent with the choice of Jang et al. (2021) to immerse, in water, specimens for compressive strength tests.

2.4.3 Propagation of bulk waves in elastic media

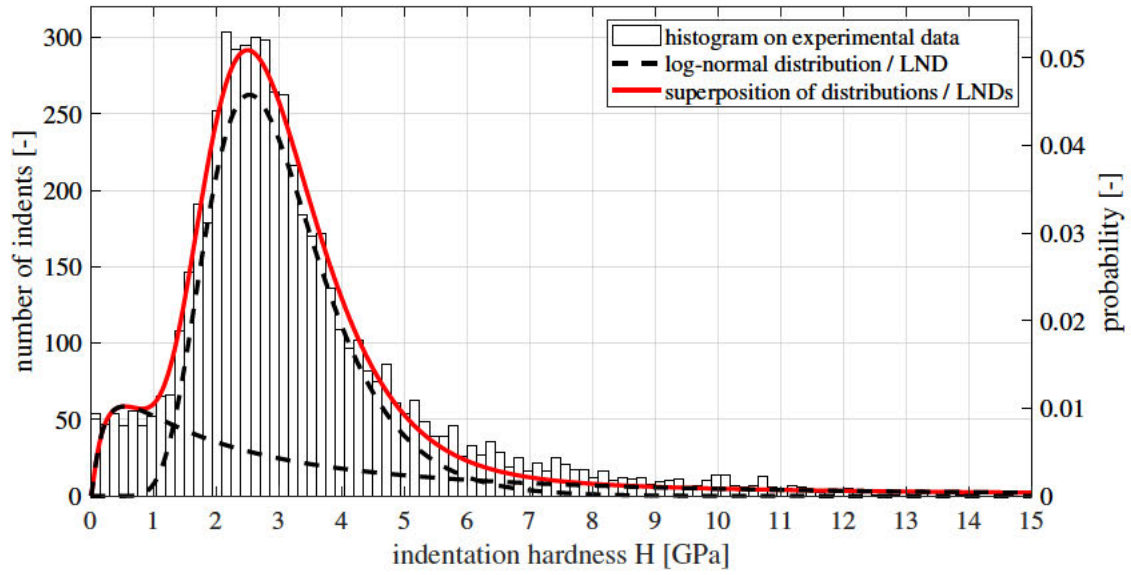
It is known that not only bulk waves without lateral deformations, mathematically characterized by Eq. (2.21), but also bar waves may propagate through a cylindrical specimen. In the case of bar waves, the Young’s modulus E rather than the elastic constant C_{1111} would follow from the product of mass density and square of the wave velocity. A systematic experimental study (Kohlhauser and Hellmich, 2013) has evidenced that the propagation of a bulk wave in cylindrical specimens with diameter a and height h essentially depends on the slenderness ratio a/h and on the height-over-wavelength ratio h/λ , according to the following criterion

$$-1.426 \log\left(\frac{a}{h}\right) - 0.530 \log\left(\frac{h}{\lambda}\right) \leq 1. \quad (2.29)$$

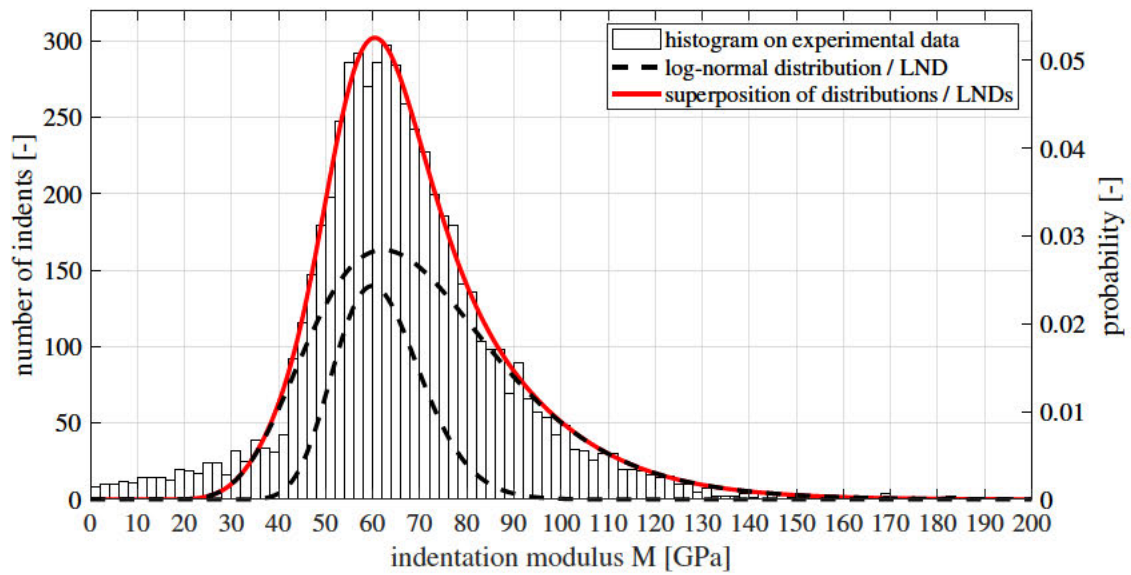
In our case, the wave velocity amounts to $v = 5000$ m/s, so that frequencies f ranging from 50 kHz to 20 MHz are associated to wavelengths $\lambda = v/f$ between 0.00025 m and 0.1 m, and with $h = 0.01$ m, the height-over-wavelength ratio ranges from 0.1 to 40. Given in addition a slenderness ratio of $a/h = 1/2$, this readily implies that the criterion (2.29) is fulfilled for all our ultrasonic tests - we indeed encounter bulk, rather than bar wave propagation, and Eq. (2.21) is valid.

2.4.4 Statistical analysis of grid nanoindentation data, and inhomogeneous regions probed by the nanoindenter

Another question which may arise concerns the necessity to represent the histograms of modulus and hardness values seen in Fig. 2.4 by three LNDs. In order to provide a direct answer to this question, we approximate the histograms of modulus and hardness by means of the superposition of only two LNDs, i.e. choosing $C = 2$ in Eq. (2.14), and employing the search intervals given for the low and medium LNDs in Table 2.A.7. As a result, we obtain realistically distinct medium and mode values characterizing the two log-normal distributions representing the hardness data, while the approximation of the modulus data delivers log-normal distribution-specific median and mode values which differ from each other by only 10.5 % and 3.7 %, respectively. Hence, when it comes to modulus representation, the approximation based on two log-normal distributions does not deliver physically distinct material phases of the cement paste material. This clearly shows that the minimum number of log-normal distribution functions needed to represent modulus and hardness data in a physically reasonable way, is three.



(a)



(b)

Fig. 2.9. Approximation of histograms by the superposition of two log-normal distributions: (a) hardness, (b) indentation modulus.

There is considerable interest in the size and properties of the region below the nanoindenter tip, which is actually characterized in the course of a nanoindentation test. Targeting at deeper understanding of a “region surrounded by the probe used”, Garboczi and Lura (2020) performed a series of computational homogenization simulations: There, a cube which was, in terms of edge length, ten to 800 times larger than differently size “subvolumes”, was subjected to periodic boundary conditions reflecting a macroscopic homogeneous strain state. Based on corresponding simulation results, Garboczi and Lura checked whether stress and strain states averaged over sufficiently small SVs still give the properties of spherical domains the size of which are approximately 1/20-th of the edge of the aforementioned big cube; as well as the properties of the matrix filling the space between these spherical domains. We remain careful when it comes to fully adopting Garboczi and Lura’s conclusions regarding nanoindentation, as the “micro”-stress and “micro”-strain fields encountered below a tip of a nanoindenter are clearly not those of a large cube subjected to periodic boundary conditions around one homogeneous “macroscopic” strain state. Rather, considerable “macroscopic” strain *gradients* would be encountered, as we will discuss further below. Still, the simulations of Garboczi and Lura are of considerable interest for us, as they underline that an SV the characteristic length of which is twice as large as the spherical domains playing the role of micro-heterogeneities or phases in the context of micromechanics, already delivers results which are close to those expected from homogenization over a matrix-inclusion composite. Hence, their simulations are fully consistent with the scale separation factor of 2 to 3 known from the landmark contributions of Drugan and Willis (1996) and Pensée and He (2007), which we refer to at the end of Section 2.2.6.

Coming back to the question whether a nanoindentation test probes the material properties of the material found directly below the tip, we refer to recent experimental studies (Königsberger et al., 2021; Ma et al., 2017) relating Oliver-Pharr solution-based modulus and hardness values associated with a particular indent, to the distance of this very indent from a boundary between a stiff and hard inclusion on the one hand, and a compliant and soft matrix domain on the other hand. Such an experimental approach naturally considers all the aforementioned stress and strain gradients occurring in the inhomogeneous domain probed by the nanoindenter, and hence, is free of potentially oversimplifying model assumptions. It turns out that the regions probed in and around stiff inclusions are three times larger than those probed by a tip indented into a soft matrix domain. Hence, it is much more probable to retrieve, from the statistical evaluation procedure described in Section 2.2.4, the actual elastic and hardness properties of the matrix, than to find those of a material making up stiff and hard inclusions. Accordingly, we obtain trustworthy results (“true peaks”) for the two types of hydrates reinforced by single-to-submicrometric calcite particles; while the elastic and hardness values associated with the third peak are lower than those expected for unhydrated clinker. The latter values rather reflect the action of an “integrated indentation tool” comprising both the tip and the clinker inclusion, which is then pressed into the matrix phase. Of course, there are no analytical solutions such as that of Oliver and Pharr, for such a complex loading scenario - and the standardly employed Oliver-Pharr formulae deliver mechanical properties which are smaller than those of the actually indented stiff inclusion material. Representation of this combined matrix-inclusion behavior may well explain not only the highest LND-peak not coinciding with the actual mechanical properties of unhydrated clinker, but also the broad spread of this LND peak. In turn, the spreading out of the two LNDs associated with calcite-reinforced hydrates rather stems from the polymorph nature of C-S-H, as reflected by a widespread density distribution (Juenger and Jennings, 2001; Muller et al., 2013b,a; Königsberger et al., 2016).

2.5 Conclusions

From the results of the presented study, the following conclusions are drawn:

- Biodentine is a hierarchically organized material containing calcite-reinforced hydrates, into which, at a higher scale, clinker grains are embedded as additional reinforcements.
- The high-density calcite-reinforced hydrates, with indentation modulus and hardness amounting to $M = 62.6$ GPa and $H = 2.78$ GPa, are significantly stiffer and stronger than hydrates of construction cement pastes, including low-density calcium-silicate-hydrates, high-density calcium-silicate-hydrates, and a nano-composite consisting of high-density calcium-silicate-hydrates reinforced by nanocrystals of calcium hydroxide.
- The macroscopic mechanical properties of Biodentine may be enhanced by reducing the occurrence of microstructural defects.
- Comprehensive grid nanoindentation into a matrix-inclusion composite, with several thousands of individual indents, allowed for demonstrating that the histograms of indentation-related stiffness and strength properties of the material constituents are asymmetric and can be represented by log-normal distributions.
- Indents with characteristic maximum depths of 87 nm into tricalcium silicate grains with a characteristic size of $4.3 \mu\text{m}$ are probing domains which are larger than the grains. This implies that the probed domain was larger than 50 times the maximum indentation depth, a situation which is known from the indentation of stiff inclusions being embedded into a soft matrix (Königsberger et al., 2021). The obtained indentation moduli and hardnesses are lower than expected, because they are influenced by the softer matrix in which the grains are embedded, see Section 2.4.4.

Acknowledgments

This project has received funding from the European Union’s Horizon 2020 research and innovation programme under the Marie Skłodowska-Curie Grant Agreement No. 764691. The authors gratefully acknowledge the support of Wolfgang Dörner from the Institute for Mechanics of Materials and Structures at TU Wien with the preparation of the molds and the temperature chamber for the ultrasound experiments.

Appendix 2.A Details on LND identification

2.A.1 Solution of the optimization problem

The optimization problem defined by Eqs. (2.13)–(2.20) as well as (2.10) and (2.11) is solved iteratively, whereby the search intervals are progressively shifted or refined, inspired by the solution method described in Irfan-ul-Hassan et al. (2016). The solution is performed in a staggered fashion, because simultaneous optimization of 14 unknowns is a computationally expensive task. Every iteration step is organized in three parts. Six variables are optimized in the first part, another six in the second part, and the remaining variables in the third part.

Part 1 of every iteration step refers to the optimization of the mean $m_{X,c}$ and standard deviation $s_{X,c}$ of a log-normal distribution. They are related with log-normal distribution

parameters $\mu_{X,c}$ and $\sigma_{X,c}$ based on following formulas:

$$\mu_{X,c} = \ln \left(m_{X,c}^2 / \sqrt{s_{X,c}^2 + m_{X,c}^2} \right) \quad (2.A.1)$$

$$\sigma_{X,c} = \sqrt{\ln \left(s_{X,c}^2 / m_{X,c}^2 + 1 \right)}. \quad (2.A.2)$$

The search intervals for the 6 optimization variables $m_{H,1}$, $m_{H,2}$, $m_{H,3}$, $s_{H,1}$, $s_{H,2}$, and $s_{H,3}$ contain 3 values each, see Table 2.A.7 for the initial search intervals. Thus, there are $3^6 = 729$ combinations. The volume fractions f_1 and f_3 are set equal to the central value of their current search interval. The remaining volume fraction f_2 is computed according to Eq. (2.16), see also Table 2.A.7. ε_{SRSS} -values of all 729 combinations are computed according to

$$\varepsilon_{SRSS} = \sqrt{\frac{1}{100} \sum_{i=1}^{100} \left[P^{exp}(H_i) - P^{app}(H_i) \right]^2} \rightarrow \min. \quad (2.A.3)$$

The optimal combination of values of $m_{H,1}$, $m_{H,2}$, and $m_{H,3}$, as well as $s_{H,1}$, $s_{H,2}$, and $s_{H,3}$ is stored.

Part 2 of every iteration step refers to the optimization of the mean $m_{X,c}$ and standard deviation $s_{X,c}$ of a log-normal distribution of the indentation modulus. The search intervals for the 6 optimization variables $m_{M,1}$, $m_{M,2}$, $m_{M,3}$, $s_{M,1}$, $s_{M,2}$, and $s_{M,3}$ contain 3 values each, see Table 2.A.7 for the initial search intervals. Thus, there are $3^6 = 729$ combinations. The volume fractions f_1 and f_3 are set equal to the central value of their current search interval. The remaining volume fraction f_2 is computed according to Eq. (2.16), see also Table 2.A.7. ε_{SRSS} -values of all 729 combinations are computed according to

$$\varepsilon_{SRSS} = \sqrt{\frac{1}{100} \sum_{i=1}^{100} \left[P^{exp}(M_i) - P^{app}(M_i) \right]^2} \rightarrow \min. \quad (2.A.4)$$

The optimal combination of values of $m_{M,1}$, $m_{M,2}$, and $m_{M,3}$, as well as $s_{M,1}$, $s_{M,2}$, and $s_{M,3}$ is stored.

Part 3 of every iteration step refers to the optimization of the volume fractions. The search intervals for f_1 and f_3 contain three values each, see Table 2.A.7 for the initial search interval. Thus, there are nine combinations. The remaining volume fraction f_2 is computed according to Eq. (2.16), see also Table 2.A.7. The mean $m_{X,c}$ and standard deviation $s_{X,c}$ of a log-normal distribution are set equal to the optimal values computed in parts 1 and 2. ε_{SRSS} -values of all 9 combinations of values of f_1 and f_3 are computed according to Eq. (2.20). The optimal values of f_1 and f_3 are stored.

Finally, new search intervals are defined for all 14 optimization variables. There are two possibilities:

1. The search interval is refined, if the optimal value of an optimization variable is equal to the central value of the previous search interval. The optimal value of the just completed iteration step becomes the central value of the new search interval, and the interval limits are redefined, such as to reduce the width of the search interval by a factor of 2, e.g. if the old search interval reads as [2 , 4 , 6], with 4 as the optimal value in the just completed iteration step, the new search interval reads as [3 , 4 , 5].

2. The search interval is shifted within the parameter space, if the optimal value of a variable is at the boundary of the previous search interval. The optimal value of the just completed iteration step becomes the central value of the new search interval, and the interval limits are redefined, such as to keep the width of the search interval the same, e.g. if the old search interval reads as [2 , 4 , 6], with 6 as the optimal value in the just completed iteration step, the new search interval reads as [4 , 6 , 8].

Within 80 000 iteration steps, optimal values are found, see Fig. 2.A.10 for the evolution of the search intervals towards the converged solution.

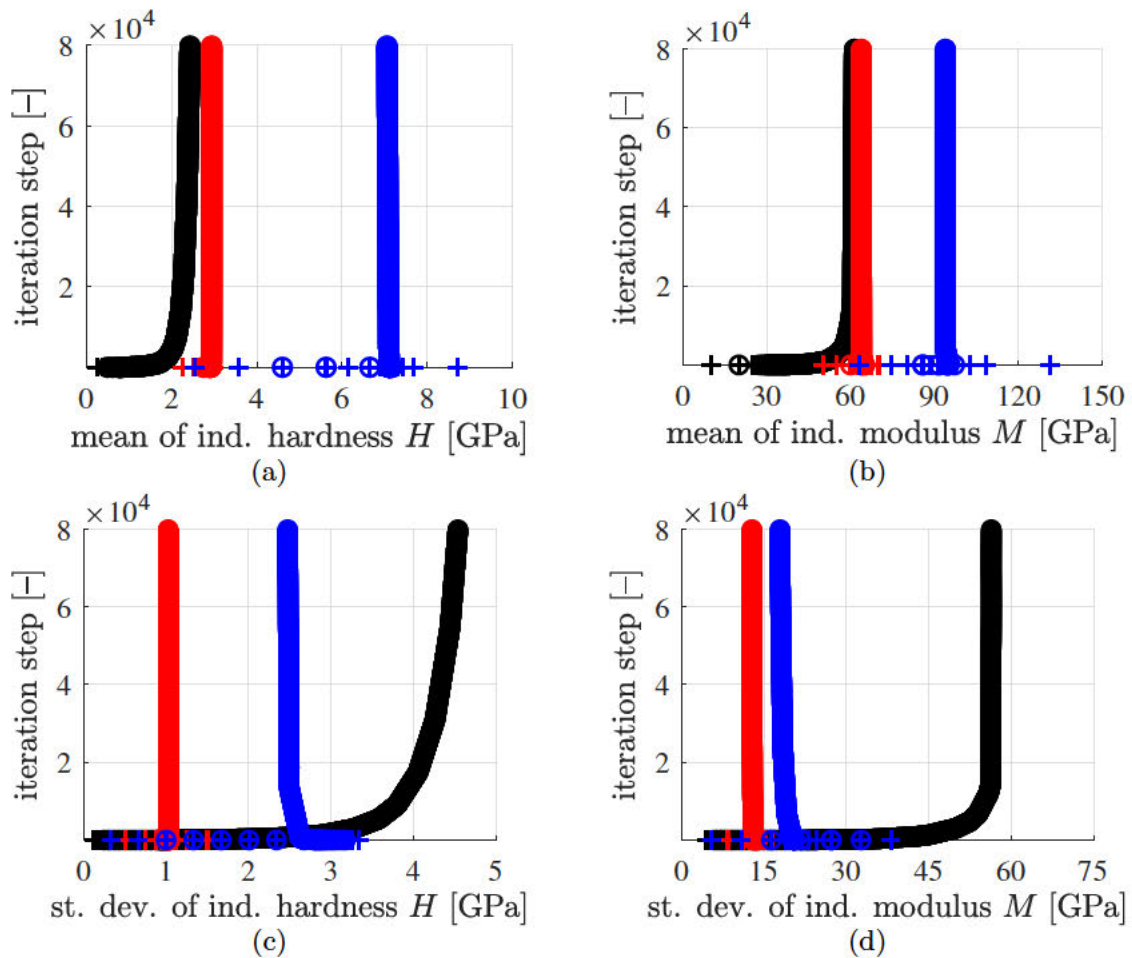


Fig. 2.A.10. Evolution of search intervals for (a) the mean value $m_{H,c}$ of the indentation hardness, (b) the mean value $m_{M,c}$ of indentation modulus, (c) the standard deviation $s_{H,c}$ of the indentation hardness, (d) the standard deviation $s_{M,c}$ of the indentation modulus; the search intervals of the low LND are shown in black, the ones of medium LND in red, and the ones of high LND in blue; numerical values within the search intervals are labelled with crosses (+), optimal values as circles (o).

2.A.2 Initial search intervals

As regards volume fraction of the high log-normal distribution (LND), the initial search interval is defined as $f_3 \in [0.10, 0.15, 0.20]$. The initial search interval for low LND is defined

as $f_1 \in [0.02, 0.03, 0.04]$. The volume fraction of medium LND is obtained from solving Eq. (2.16) for f_2 . This yields $f_2 = 1 - f_1 - f_3$, see also Table 2.A.7.

Table 2.A.7

Initial search intervals for 14 variables optimized during modal analysis.

low LND, $c = 1$	$m_{M,1} \in [20, 30, 40]$ GPa	$s_{M,1} \in [4.5, 6.0, 7.5]$ GPa
	$m_{H,1} \in [0.25, 0.50, 0.75]$ GPa	$s_{H,1} \in [0.125, 0.25, 0.375]$ GPa
	$f_1 \in [0.02, 0.03, 0.04]$	
medium LND, $c = 2$	$m_{M,2} \in [50, 60, 70]$ GPa	$s_{M,2} \in [8.4, 11.1, 13.8]$ GPa
	$m_{H,2} \in [2.25, 2.50, 2.75]$ GPa	$s_{H,2} \in [0.50, 1.00, 1.50]$ GPa
	$f_2 = 1 - f_3 - f_1$	
high LND, $c = 3$	$m_{M,3} \in [85.8, 108.6, 131.4]$ GPa	$s_{M,3} \in [5.4, 10.9, 16.3]$ GPa
	$m_{H,3} \in [4.60, 6.65, 8.70]$ GPa	$s_{H,3} \in [0.33, 0.67, 1.00]$ GPa
	$f_3 \in [0.10, 0.15, 0.20]$	

The initial search intervals for the mean values of the indentation modulus are defined on the basis of the histogram of Fig. 2.4 (a). As for the low LND, the search interval is defined as $m_{M,1} \in [20, 30, 40]$ GPa, and the one for the medium LND as $m_{M,2} \in [50, 60, 70]$ GPa. As for high LND, the lower and upper estimate is based on elastic modulus of calcite and clinker, respectively. The corresponding values 83.8 GPa and 135 GPa, and their Poisson's ratios, 0.31 and 0.3, taken from Lavergne et al. (2018), Velez et al. (2001), respectively, are inserted into Eq. (2.8). This yields the expected values of the indentation moduli of 85.8 GPa, and 131.4 GPa. Then, the corresponding initial search interval are defined as $m_{M,3} \in [85.8, 108.6, 131.4]$ GPa, see also Table 2.A.7.

The initial search interval for the standard deviation of the indentation modulus of high LND is defined by analogy to cement clinker, in the range from 5% to 15% of the middle value of $m_{M,3}$ search interval, here: 108.6 GPa, see the previous paragraph. This yields $s_{M,3} \in [5.4, 10.9, 16.3]$ GPa. The search interval for medium LND is defined, by analogy to properties of low and high density C-S-H (Constantinides and Ulm, 2007), in the range from 14% to 23% of the expected value, here: 60 GPa, see the previous paragraph. This yields $s_{M,2} \in [8.4, 11.1, 13.8]$ GPa. Given that the ratio between standard deviation and expected value is typically the larger, the smaller the expected value, the initial search interval of low LND is set equal to 15%, 20%, 25% of the expected value, here 30 GPa, see the previous paragraph. This yields: $s_{M,1} \in [4.5, 6.0, 7.5]$ GPa, see also Table 2.A.7.

The initial search intervals for the mean values of the indentation hardness are defined on the basis of the histogram of Fig. 2.4 (b). As for the low LND, the search interval is defined as $m_{H,1} \in [0.25, 0.50, 0.75]$ GPa, and the one for the medium LND as $m_{H,2} \in [2.25, 2.50, 2.75]$ GPa. As for high LND, the lower and upper bound of the initial search interval is defined based on hardness of calcite and clinker. The former is 4.60 GPa which is the largest hardness of calcite found in seashells (Merkel et al., 2009). The latter is 8.70 GPa which is the hardness of Ca_3SiO_5 found in Velez et al. (2001). Thus, $m_{H,3} \in [4.60, 6.65, 8.70]$ GPa, see also Table 2.A.7.

The initial search interval for the standard deviation of the indentation hardness of high LND is defined by analogy to that of the indentation modulus, i.e. as 10% of the middle value 6.65 GPa, see the previous paragraph, plus/minus 5 percent points. This yields $s_{H,3} \in [0.33, 0.67, 1.00]$ GPa. The search interval for medium LND and the low LND are

defined based on the histogram shown in Fig. 2.4(b), as $s_{H,2} \in [0.50, 1.00, 1.50]$ GPa and $s_{H,1} \in [0.125, 0.250, 0.375]$ GPa, see also Table 2.A.7.

Once the initial search intervals of the $m_{X,c}$, $s_{X,c}$ are defined, they are translated into corresponding values of $\mu_{X,c}$ and $\sigma_{X,c}$ based on Eq. (2.A.1) and Eq. (2.A.2). These values enter the solution procedure of the optimization problem as described in Appendix 2.A.

Appendix 2.B Continuum micromechanics

Methods of continuum micromechanics (Zaoui, 2002) provide access to bounds and estimates of the homogenized “effective” stiffness of RVEs of microheterogeneous materials. To this end, the microstructure of Biodentine is represented as an arrangement of C isotropic constituents. Every constituent occupies a specific fraction of the volume of the material, see Eq. (2.17), and has a specific elastic stiffness tensor

$$\mathbb{C}_c = 3k_c \mathbb{I}_{vol} + 2\mu_c \mathbb{I}_{dev}, \quad c = 1, 2, \dots, C, \quad (2.B.1)$$

where k_c and μ_c stand for the bulk and the shear modulus of the c^{th} constituent, while \mathbb{I}_{vol} and \mathbb{I}_{dev} denote the volumetric and the deviatoric part of the symmetric fourth-order identity tensor \mathbb{I} , with components

$$I_{ijkl} = \frac{1}{2}(\delta_{ik}\delta_{jl} + \delta_{il}\delta_{jk}). \quad (2.B.2)$$

More specifically, \mathbb{I}_{vol} and \mathbb{I}_{dev} read as

$$\mathbb{I}_{vol} = \frac{1}{3}(\mathbf{1} \otimes \mathbf{1}), \quad (2.B.3)$$

and

$$\mathbb{I}_{dev} = \mathbb{I} - \mathbb{I}_{vol}, \quad (2.B.4)$$

where $\mathbf{1}$ denotes the second-order identity tensor with components equal to the Kronecker delta δ_{ij} with $\delta_{ij} = 1$ for $i = j$, and 0 otherwise. The bulk and the shear moduli are determined from

$$k_c = \frac{E_c}{3(1 - 2\nu_c)}, \quad (2.B.5)$$

$$\mu_c = \frac{E_c}{2(1 + \nu_c)}, \quad (2.B.6)$$

with the elastic modulus E_c following from Eq. (2.8), while Poisson’s ratio values are adopted from the open literature: For the reasons detailed in Section 2.3, the low and medium LNDs are associated with a value of 0.24, which is representative for C-S-H (Lavergne et al., 2018); while the high LND is associated with a value of 0.30, which is representative for clinker (Lavergne et al., 2018).

An upper bound for the homogenized stiffness, introduced by Voigt (1889), is the volume average of the stiffness tensors of the constituents (Zaoui, 2002; Dormieux et al., 2006)

$$\mathbb{C}^{UB} = \sum_{c=1}^n f_c \mathbb{C}_c. \quad (2.B.7)$$

A lower bound for the homogenized stiffness, introduced by Reuss (1929), is the inverse of the volume average of the compliance tensors of the constituents (Zaoui, 2002; Dormieux et al., 2006)

$$\mathbb{C}^{LB} = \left(\sum_{c=1}^n f_c \mathbb{C}_c^{-1} \right)^{-1}. \quad (2.B.8)$$

The self-consistent estimate of the homogenized stiffness of a microheterogeneous material consisting of constituents with spherical phase shapes reads as (Zaoui, 2002; Hill, 1965b)

$$\mathbf{C}_{sc} = 3 k_{hom} \mathbb{I}_{vol} + 2 \mu_{hom} \mathbb{I}_{dev}, \quad (2.B.9)$$

with (Hellmich and Mang, 2005)

$$k_{hom} = \left(\sum_{c=1}^n \frac{f_c k_c}{1 + \frac{S_{vol}(k_c - k_{hom})}{k_{hom}}} \right) \times \left(\sum_{c=1}^n \frac{f_c}{1 + \frac{S_{vol}(k_c - k_{hom})}{k_{hom}}} \right)^{-1}, \quad (2.B.10)$$

$$\mu_{hom} = \left(\sum_{c=1}^n \frac{f_c \mu_c}{1 + \frac{S_{dev}(\mu_c - \mu_{hom})}{\mu_{hom}}} \right) \times \left(\sum_{c=1}^n \frac{f_c}{1 + \frac{S_{dev}(\mu_c - \mu_{hom})}{\mu_{hom}}} \right)^{-1}, \quad (2.B.11)$$

and (Zaoui, 2002; Eshelby, 1957)

$$S_{vol} = \frac{3 k_{hom}}{3 k_{hom} + 4 \mu_{hom}}, \quad (2.B.12)$$

$$S_{dev} = \frac{6 (k_{hom} + 2 \mu_{hom})}{5 (3 k_{hom} + 4 \mu_{hom})}. \quad (2.B.13)$$

The implicit definition of k_{hom} and μ_{hom} necessitates an iterative computation (Hellmich and Mang, 2005).

Appendix 2.C Experimental data

Table 2.C.8

Numerical details of the histogram of indentation hardness shown in Fig. 2.4 (a).

Int. no.	Cent. val. H_i [GPa]	Count of ind. [-]	Int. no.	Cent. val. H_i [GPa]	Count of ind. [-]
1	0.075	54	51	7.575	21
2	0.225	47	52	7.725	17
3	0.375	54	53	7.875	17
4	0.525	46	54	8.025	12
5	0.675	56	55	8.175	16
6	0.825	46	56	8.325	10
7	0.975	52	57	8.475	12
8	1.125	65	58	8.625	11
9	1.275	66	59	8.775	12
10	1.425	108	60	8.925	8
11	1.575	146	61	9.075	9
12	1.725	191	62	9.225	10
13	1.875	179	63	9.375	11
14	2.025	252	64	9.525	6
15	2.175	303	65	9.675	7
16	2.325	292	66	9.825	10

Continued on next page

Table 2.C.8 – continued from previous page

Ind. no.	Cent. val. H_i [GPa]	Count of ind. [-]	Ind. no.	Cent. val. H_i [GPa]	Count of ind. [-]
17	2.475	295	67	9.975	14
18	2.625	300	68	10.125	14
19	2.775	298	69	10.275	7
20	2.925	264	70	10.425	6
21	3.075	262	71	10.575	7
22	3.225	216	72	10.725	13
23	3.375	184	73	10.875	6
24	3.525	170	74	11.025	3
25	3.675	172	75	11.175	7
26	3.825	136	76	11.325	6
27	3.975	109	77	11.475	4
28	4.125	97	78	11.625	2
29	4.275	102	79	11.775	1
30	4.425	82	80	11.925	4
31	4.575	75	81	12.075	5
32	4.725	86	82	12.225	0
33	4.875	61	83	12.375	3
34	5.025	54	84	12.525	1
35	5.175	63	85	12.675	0
36	5.325	49	86	12.825	1
37	5.475	39	87	12.975	3
38	5.625	39	88	13.125	0
39	5.775	46	89	13.275	0
40	5.925	26	90	13.425	2
41	6.075	33	91	13.575	0
42	6.225	27	92	13.725	0
43	6.375	36	93	13.875	1
44	6.525	29	94	14.025	1
45	6.675	19	95	14.175	0
46	6.825	25	96	14.325	0
47	6.975	16	97	14.475	1
48	7.125	22	98	14.625	1
49	7.275	16	99	14.775	0
50	7.425	25	100	14.925	0

Table 2.C.9

Numerical details of the histogram of indentation modulus shown in Fig. 2.4 (b).

Ind. no.	Cent. val. M_i [GPa]	Count of ind. [-]	Ind. no.	Cent. val. M_i [GPa]	Count of ind. [-]
1	1	8	51	101	48
2	3	10	52	103	33

Continued on next page

Table 2.C.9 – continued from previous page

Ind. no.	Cent. val. M_i [GPa]	Count of ind. [-]	Ind. no.	Cent. val. M_i [GPa]	Count of ind. [-]
3	5	10	53	105	32
4	7	12	54	107	26
5	9	11	55	109	30
6	11	14	56	111	30
7	13	14	57	113	20
8	15	14	58	115	20
9	17	13	59	117	19
10	19	20	60	119	16
11	21	19	61	121	14
12	23	17	62	123	15
13	25	24	63	125	10
14	27	24	64	127	10
15	29	16	65	129	5
16	31	32	66	131	7
17	33	25	67	133	2
18	35	39	68	135	2
19	37	34	69	137	2
20	39	31	70	139	4
21	41	42	71	141	1
22	43	92	72	143	5
23	45	116	73	145	4
24	47	147	74	147	3
25	49	179	75	149	1
26	51	198	76	151	2
27	53	247	77	153	2
28	55	286	78	155	1
29	57	292	79	157	0
30	59	270	80	159	2
31	61	286	81	161	0
32	63	297	82	163	1
33	65	284	83	165	1
34	67	259	84	167	1
35	69	242	85	169	4
36	71	227	86	171	0
37	73	199	87	173	0
38	75	185	88	175	1
39	77	179	89	177	0
40	79	141	90	179	0
41	81	136	91	181	0
42	83	103	92	183	2
43	85	98	93	185	0
44	87	98	94	187	0
45	89	69	95	189	0
46	91	89	96	191	0

Continued on next page

Table 2.C.9 – continued from previous page

Ind. no.	Cent. val. M_i [GPa]	Count of ind. [-]	Ind. no.	Cent. val. M_i [GPa]	Count of ind. [-]
47	93	66	97	193	0
48	95	57	98	195	0
49	97	54	99	197	0
50	99	42	100	199	0

Chapter 3

Stiffness and stress fluctuations in dental cement paste: A continuum micromechanics approach

Authored by: Petr Dohnalík, Christian Hellmich, Gilles Richard, Bernhard L.A. Pichler

Published in: *Mechanics of Advanced Materials and Structures*,
DOI: 10.1080/15376494.2022.2073493, 2022

The final publication is available at:
<https://doi.org/10.1080/15376494.2022.2073493>

Abstract: Calcite-reinforced hydrates provide the superior mechanical properties of Bio-dentine, a cementitious material used in dentistry. Herein, a self-consistent micromechanics model links two nanoindentation-probed, lognormally distributed microstiffness distributions of infinitely many hydrate phases, to the material's macrostiffness, quantified from longitudinal and transverse ultrasonic wave transmission experiments. Thereby, the model provides values for the Poisson's ratio of the hydrates and for a microcrack density reflecting grain boundary defects. Moreover, the model-predicted hydrate microstresses turn out as beta-distributed, while the overall stiffness can be equally well upscaled from only two, piecewise uniform, hydrate phases exhibiting median microstiffness values.

Contribution: Petr Dohnalík: Investigation, Methodology, Formal analysis, Software, Visualization, Writing – review & editing. Bernhard L.A. Pichler: Supervision, Conceptualization, Funding acquisition, Methodology, Formal analysis, Writing – original draft, Writing – review & editing. Gilles Richard: Conceptualization, Funding acquisition, Resources, Writing – review & editing. Christian Hellmich: Conceptualization, Funding acquisition, Formal analysis, Supervision, Writing – review & editing.

Keywords: Stiffness homogenization, Stiffness fluctuations, Stress fluctuations, Dental cement paste, Continuum Micromechanics, Lognormal microelasticity model, Piecewise uniform microelasticity mode

3.1 Introduction

Biodentine is a cementitious material used in dentistry. The main hydraulic component is tricalcium silicate (“clinker”), making up 74 wt% of the dry binder powder (Laurent et al., 2008, 2012). Calcite (16.5 wt%) acts as a filler and reinforcement (Dohnalík et al., 2021). Zirconium dioxide (“zirconia”, 5 wt%) provides X-ray opacity. The mixing liquid consists of water, a modified polycarboxylate polymer (= superplasticizer), and calcium chloride accelerating the setting reaction (Laurent et al., 2008, 2012). The present paper refers to micromechanics modeling of the elastic stiffness of well-hardened Biodentine, based on results from a grid nanoindentation testing campaign (Dohnalík et al., 2021).

Using results from grid nanoindentation as microscopic input for upscaling of the elastic stiffness of cement paste was introduced by Constantinides and Ulm (2004). They performed 200 indentation tests into the calcium-silicate-hydrate matrix. The 200 resulting values of indentation moduli were translated into moduli of elasticity, assuming a Poisson’s ratio of 0.24 (Constantinides, 2002). The histogram of the moduli of elasticity showed two peaks. They were represented by the superposition of two Gaussian probability density functions. Their mean values were used as input for upscaling of the elastic stiffness of cement paste, delivering a homogenized modulus of elasticity amounting to 23.2 GPa. As for validation, the speed of longitudinal ultrasonic waves passing through the tested material, its mass density, and its Poisson’s ratio (set equal to 0.24) were translated, based on the theory of elastic wave propagation through isotropic media, into the macroscopic modulus of elasticity: 22.8 GPa (Constantinides and Ulm, 2004). This success motivated follow-up developments, see the discussion section, and it provides the motivation for the present contribution. Focused on Biodentine, it is aimed at linking microstructural stiffness distributions by means of a micromechanics model to the macroscopic effective (= homogenized) stiffness of the material.

As regards microscopic characterization of Biodentine, results from a grid nanoindentation testing campaign are taken from Dohnalík et al. (2021). 5748 nanoindentation tests were performed with a Berkovich tip. Imposing maximum indentation forces of 1 mN resulted in maximum indentation depths of on average 140 nm. Only two experiments had to be excluded, because their maximum indentation depths were smaller than 45 nm and, therefore, did not satisfy the requirement of being at least 2.5-times larger than the root-mean-squared average surface roughness (Miller et al., 2008; Donnelly et al., 2006), which amounted to 18 nm (Dohnalík et al., 2021). 5746 force-displacement diagrams were evaluated based on the Oliver-Pharr formulae for nanoindentation into infinite halfspaces (Oliver and Pharr, 1992). The obtained histogram of the indentation modulus was represented by the superposition of three lognormal probability density functions, see Fig. 3.1. Lognormal distributions were used rather than Gaussians, because (i) indentation moduli are strictly positive quantities, and (ii) the large number of indentation experiments revealed skewed rather than symmetric stiffness distributions. The rightmost lognormal distribution in Fig. 3.1 refers to both clinker and zirconia, the central distribution to high-density calcite-reinforced hydrates (“HDCR hydrates”), and the leftmost to lower-density calcite-reinforced hydrates (“LDCR hydrates”), see Dohnalík et al. (2021) and Table 3.1. This reveals the existence of two types of hydrates reinforced by calcite particles of single-to-submicrometric size (Li et al., 2019). The two populations of hydrates are reminiscent of construction cement pastes in which inner and outer products (Taplin, 1959), phenograin and groundmass (Diamond and Bonen, 1993), low-density and high-density C-S-H (Tennis and Jennings, 2000; Jennings, 2000), as well as class-A and class-B C-S-H (Königsberger et al., 2016) are distinguished.

Evaluation of nanoindentation tests into the stiff clinker and zirconia grains, based on the

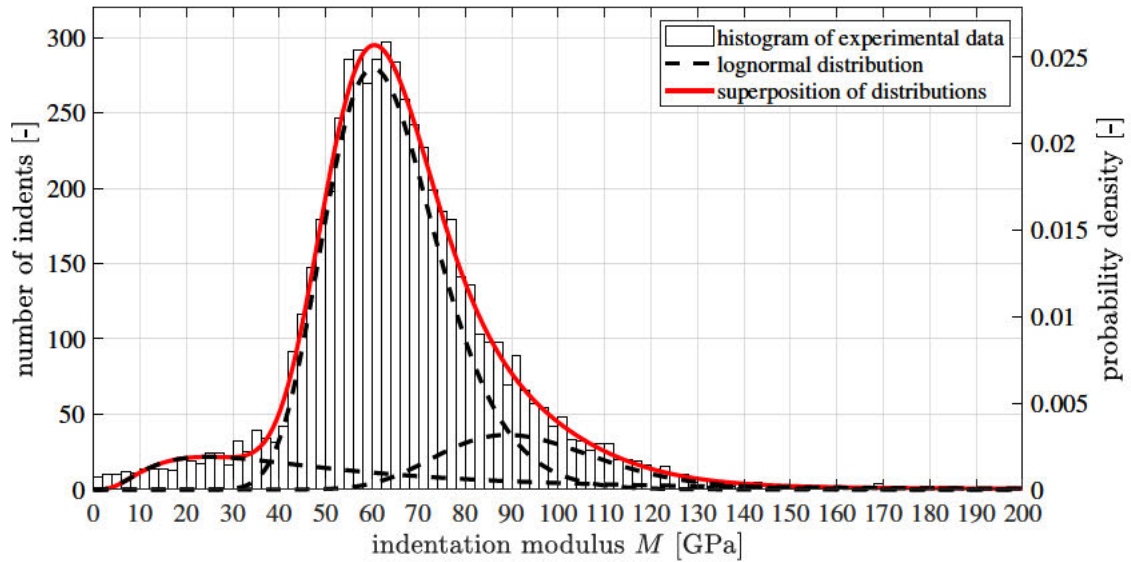


Fig. 3.1. Histogram of indentation modulus approximated by the superposition of three lognormal distributions; after Dohnalík et al. (2021).

Table 3.1

Results obtained from grid nanoindentation testing (Dohnalík et al., 2021): values of medians, modes, and volume fractions associated with the three lognormal distributions representing the histogram of indentation moduli in Fig. 3.1.

lognormal distribution	median [GPa]	mode [GPa]	volume fraction [-]
LDCR hydrates	45.1	24.5	0.1228
HDCR hydrates	62.6	60.2	0.7420
clinker and zirconia	92.2	89.0	0.1352
		sum:	1.0000

Oliver-Pharr formulae mentioned above, led to smaller-than-expected indentation moduli, because the grains acted as a kind of larger indenters pressed into the softer surrounding hydrated material. This effect has been shown explicitly by image-supported grid nanoindentation, applied to two different types of cementitious materials (Ma et al., 2017; Königsberger et al., 2021). Hence, we resort to the well known elastic properties of clinker and zirconia which are taken from the literature, see Table 3.2. The volume fractions of all four types of solid constituents are taken from Dohnalík et al. (2021).

Table 3.2

Input quantities of the solid material constituents: bulk moduli, k_i , shear moduli g_i , as well as lognormal parameters μ_i and σ_i which are consistent with median and mode values listed in Table 3.1; input values taken from Hussey and Wilson (1998); Pichler and Hellmich (2011); Dohnalík et al. (2021).

phase	index	stiffness properties		vol. fraction
zirconia	$i = 1$	$k_1 = 170.8$ GPa	$g_1 = 78.8$ GPa	$f_1 = 0.0182$
clinker	$i = 2$	$k_2 = 116.7$ GPa	$g_2 = 53.8$ GPa	$f_2 = 0.1170$
HDCR hydrates	$i = 3$	$\mu_3 = 4.14$	$\sigma_3 = 0.20$	$f_3 = 0.7420$
LDCR hydrates	$i = 4$	$\mu_4 = 3.81$	$\sigma_4 = 0.78$	$f_4 = 0.1228$

As regards macroscopic characterization of Biodentine, the speed of longitudinal ultrasonic waves and the mass density were reported in Dohnalík et al. (2021). Herein, also the speed of transversal ultrasonic waves sent through well-hardened Biodentine is provided, see Appendix 3.A. This allows for the *complete* characterization of the macroscopic isotropic stiffness of the material:

$$k_{bio}^{exp} = 38.4 \text{ GPa}, \quad (3.1)$$

$$g_{bio}^{exp} = 14.1 \text{ GPa}, \quad (3.2)$$

where k_{bio}^{exp} and g_{bio}^{exp} denote the macroscopic bulk and shear moduli of Biodentine; for details see Appendix 3.A.

The micromechanics model will also account for grain boundary defects. This is motivated as follows. Micromechanical stiffness bounds were computed for Biodentine, based on median stiffness values and volume fractions of the three lognormal distributions (Dohnalík et al., 2021). The *lower bound* for the stiffness tensor component C_{1111} turned out to be significantly *larger than* the value of C_{1111} derived from the ultrasonic longitudinal wave transmission experiments. This analysis indicated the existence of zero-volume microstructural defects such as imperfect grain boundaries.

The focus of the present contribution rests on the development of a micromechanics model which establishes a quantitative link between the microstructural stiffness properties (see Fig. 3.1 and Tables 3.1 and 3.2) and the macroscopic effective stiffness of Biodentine, see Eqs. (3.1) and (3.2), with two remarkable features:

- Grain boundary defects will be accounted for in a self-consistent homogenization approach. They will be modeled by means of closed circular cracks which are isotropically oriented in space. Budiansky and O’Connell’s dimensionless crack density parameter (Budiansky and O’Connell, 1976; Pensée et al., 2002) will be quantified from linking the micromechanical model to both nanoindentation and ultrasonic test results.

- The lognormal *distributions* of the indentation modulus of the two populations of calcite-reinforced hydrates will serve as input for the micromechanics model, rather than just one representative stiffness per population. Poisson's ratio of the two populations of calcite-reinforced hydrates will be quantified from linking the micromechanical model to both nanoindentation and ultrasonic test results.

The described micromechanics model will be used to illustrate quantitatively how *macroscopic uniform loading* imposed on a representative volume of Biodentine results in *microscopic stress and strain distributions* inside the two populations of hydrates.

The lognormal microelasticity model will also allow for assessing the potential and the limitations of piecewise uniform microelasticity models. The latter are based on just one representative stiffness per population of calcite-reinforced hydrates. This is particularly interesting in case of skewed probability density functions (Fig. 3.1) in which the mode (= most frequent value), the median (= 50%-quantile), and the mean value are different, while they are all the same in case of Gaussians.

The present paper is structured as follows: Section 3.2 presents the lognormal microelasticity model for Biodentine, accounting for the microstiffness distributions of the two populations of hydrates by means of two times infinitely many material phases. Section 3.3 is dedicated to stress and strain fluctuations within the hydrates of Biodentine, quantified by means of probability density functions of volumetric and deviatoric strain and stress concentration tensor components of the two populations of hydrates. Section 3.4 deals with piecewise uniform microelasticity models in which a representative uniform stiffness is assigned to each one of the two populations of hydrates. Section 3.5 contains a discussion. Section 3.6 closes the paper with conclusions drawn from results of the presented study.

3.2 Lognormal microelasticity model for Biodentine

3.2.1 Fundamentals of stiffness homogenization

Stiffness homogenization refers to a boundary value problem of the linear theory of elasticity. It is defined on a representative volume V of the microheterogeneous material of interest.

The field equations refer to all positions \underline{x} inside V . The linear geometric equations define the linearized strain tensor $\boldsymbol{\varepsilon}$ as the symmetric part of the displacement gradient. Denoting the displacement vector as \underline{u} , they read as $\boldsymbol{\varepsilon}(\underline{x}) = \frac{1}{2}[\nabla\underline{u}(\underline{x}) + \nabla\underline{u}^T(\underline{x})]$. The linear constitutive relations refer to linear elastic material behavior. Denoting Cauchy's stress tensor as $\boldsymbol{\sigma}$ and the elasticity tensor as \mathbf{C} , they read as $\boldsymbol{\sigma}(\underline{x}) = \mathbf{C}(\underline{x}) : \boldsymbol{\varepsilon}(\underline{x})$. The stresses must fulfill the equilibrium conditions, reading as $\text{div}\boldsymbol{\sigma}(\underline{x}) = 0$.

The boundary conditions refer to all positions \underline{x} at the surface ∂V of the representative volume. Herein, uniform strain boundary conditions are used (Hashin, 1983). Denoting the imposed macroscopic strain state as \mathbf{E} , they read as

$$\underline{u}(\underline{x}) = \mathbf{E} \cdot \underline{x}. \quad (3.3)$$

Homogenization of the elastic stiffness is facilitated based on the introduction of quasi-homogeneous constituents of the microheterogeneous material. Denoted as material phases, they occupy specific subvolumes V_i of the representative volume V . Their volume fractions read as $f_i = V_i/V$, with $i = 1, 2, \dots, N$, where N denotes the number of material phases. In addition, material phases are characterized by specific elastic stiffness tensors \mathbf{C}_i . Average

phase strains and stresses are introduced:

$$\boldsymbol{\varepsilon}_i = \frac{1}{V_i} \int_{V_i} \boldsymbol{\varepsilon}(\underline{x}) \, dV, \quad i = 1, 2, \dots, N, \quad (3.4)$$

$$\boldsymbol{\sigma}_i = \frac{1}{V_i} \int_{V_i} \boldsymbol{\sigma}(\underline{x}) \, dV, \quad i = 1, 2, \dots, N. \quad (3.5)$$

Boundary conditions (3.3) and the principle of virtual power (Königsberger et al., 2020) imply the existence of the following strain and stress average rules:

$$\mathbf{E} = \sum_{i=1}^N f_i \boldsymbol{\varepsilon}_i, \quad (3.6)$$

$$\boldsymbol{\Sigma} = \sum_{i=1}^N f_i \boldsymbol{\sigma}_i, \quad (3.7)$$

where $\boldsymbol{\Sigma}$ denotes the macroscopic stress state. Because the stiffness is uniform inside the phase volumes V_i , the phase-specific version of the elasticity law reads as:

$$\boldsymbol{\sigma}_i = \mathbf{C}_i : \boldsymbol{\varepsilon}_i, \quad i = 1, 2, \dots, N. \quad (3.8)$$

Macro-to-micro and micro-to-macro scale transitions are made possible by so-called strain concentration tensors \mathbb{A}_i . They establish links between the macrostrain and the average phase strains (Hill, 1963, 1965a,b; Zaoui, 2002):

$$\boldsymbol{\varepsilon}_i = \mathbb{A}_i : \mathbf{E}, \quad i = 1, 2, \dots, N. \quad (3.9)$$

Strain concentration tensors also allow for bottom-up stiffness homogenization, as will be explained next. Inserting $\boldsymbol{\varepsilon}_i$ according to Eq. (3.9) into Eq. (3.8), and the resulting expression for $\boldsymbol{\sigma}_i$ into Eq. (3.7) yields a relation between the macrostress $\boldsymbol{\Sigma}$ and the macrostrain \mathbf{E} . Comparing it with the macroscopic version of the elasticity law,

$$\boldsymbol{\Sigma} = \mathbf{C}_{hom} : \mathbf{E}, \quad (3.10)$$

delivers the following expression for the homogenized stiffness tensor (Hill, 1963; Zaoui, 2002)

$$\mathbf{C}_{hom} = \sum_{i=1}^N f_i \mathbf{C}_i : \mathbb{A}_i. \quad (3.11)$$

Stress concentration tensors \mathbb{B}_i establish links between the macrostress and the average phase stresses:

$$\boldsymbol{\sigma}_i = \mathbb{B}_i : \boldsymbol{\Sigma}, \quad i = 1, 2, \dots, N. \quad (3.12)$$

The stress concentration tensors are related to the strain concentration tensors, as will be shown next. The macroscopic elasticity law (3.10) is solved for the macrostrain: $\mathbf{E} = (\mathbf{C}_{hom})^{-1} : \boldsymbol{\Sigma}$. Inserting it into Eq. (3.9) and the resulting expression for $\boldsymbol{\varepsilon}_i$ into Eq. (3.8) yields a relation between the microstresses $\boldsymbol{\sigma}_i$ and the macrostress $\boldsymbol{\Sigma}$. Comparing this relation with Eq. (3.12) yields

$$\mathbb{B}_i = \mathbf{C}_i : \mathbb{A}_i : (\mathbf{C}_{hom})^{-1}, \quad i = 1, 2, \dots, N. \quad (3.13)$$

Eqs. (3.9), (3.11), and (3.13) underline that strain concentration tensors enable scale transitions in continuum micromechanics. These strain concentration tensors are estimated based on Eshelby/Laws-type matrix-inclusion problems (Eshelby, 1957; Laws, 1977). This will be explained in more detail in the context of the following development of a lognormal microelasticity model for Biodentine.

3.2.2 Tensorial formulation of lognormal microelasticity model for Biodentine

Continuum micromechanics models account for key features of microheterogeneous materials: the stiffness constants of the material phases, their volume fractions, their characteristic phase shapes, and the specific type of interaction between the phases. Biodentine consists of five types of constituents: zirconia (index $i = 1$), clinker ($i = 2$), HDCR hydrates ($i = 3$), LDCR hydrates ($i = 4$), and grain boundary defects modeled as closed microcracks ($i = 5$). The microstructure of Biodentine is represented as a highly disordered (“polycrystalline”) arrangement of material constituents which exhibit direct phase-to-phase interaction, see Fig. 3.2.

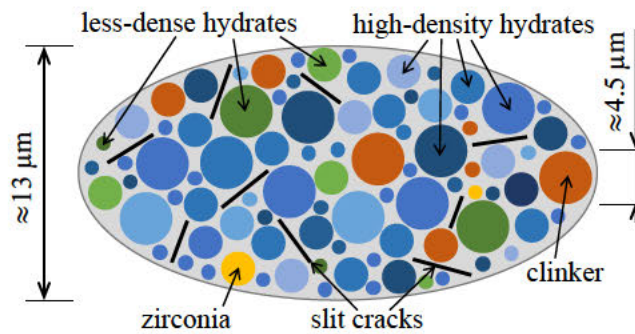


Fig. 3.2. Micromechanical representation of Biodentine (“material organogram”): the two-dimensional sketch shows qualitative properties of a three-dimensional representative volume element of the *lognormal* microelasticity model which accounts for stiffness *distributions* of two populations of hydrates.

As regards phase shapes, all four types of solid constituents are represented as spherical phases. The microcracks are introduced as thin oblate spheroids.¹ Because they are isotropically oriented in space, they will be represented as a population of infinitely many material phases (Dormieux et al., 2006; Zhu et al., 2011).

Zirconia and clinker are isotropic and have universal stiffness properties

$$\mathbb{C}_i = 3k_i \mathbb{I}^{vol} + 2g_i \mathbb{I}^{dev}, \quad i = 1, 2, \quad (3.14)$$

where k_i and g_i denote the bulk and shear moduli, see Table 3.2. \mathbb{I}^{vol} and \mathbb{I}^{dev} stand for the volumetric and deviatoric parts of the symmetric fourth-order identity tensor \mathbb{I} . Their components read as $I_{ijkl} = (\delta_{ik}\delta_{jl} + \delta_{il}\delta_{jk})/2$, $I_{ijkl}^{vol} = (\delta_{ij}\delta_{kl})/3$, and $I_{ijkl}^{dev} = I_{ijkl} - I_{ijkl}^{vol}$, where δ_{ij} is the Kronecker delta which is equal to 1 for $i = j$, and equal to 0 otherwise. \mathbb{I}^{vol} and \mathbb{I}^{dev} satisfy the following relations:

$$\mathbb{I}^{vol} : \mathbb{I}^{vol} = \mathbb{I}^{vol}, \quad (3.15)$$

$$\mathbb{I}^{dev} : \mathbb{I}^{dev} = \mathbb{I}^{dev}, \quad (3.16)$$

$$\mathbb{I}^{vol} : \mathbb{I}^{dev} = 0, \quad (3.17)$$

$$\mathbb{I}^{dev} : \mathbb{I}^{vol} = 0. \quad (3.18)$$

¹The transition to flat circular slit cracks will be explained in Subsection 3.2.3.

The two populations of hydrates exhibit lognormal stiffness distributions, see Table 3.1. The probability distribution functions of their indentation moduli M read as:

$$\varphi_i(M) = \frac{1}{M\sigma_i\sqrt{2\pi}} \exp\left(-\frac{1}{2}\left[\frac{\ln(M) - \mu_i}{\sigma_i}\right]^2\right), \quad i = 3, 4. \quad (3.19)$$

By definition, the area under the graphs of the probability density functions (3.19) is equal to one:

$$\int_0^{\infty} \varphi_i(M) dM = 1, \quad i = 3, 4. \quad (3.20)$$

The continuous stiffness distributions of both populations of hydrates are accounted for in the continuum micromechanics model by representing each one of the two populations of hydrates as infinitely many material phases, each with an infinitesimally small volume fraction. The phases inside the RVE are complemented by two additional phases with finite volume fractions, representing zirconia and clinker, and by infinitely many crack phases.

The self consistent scheme is well suited for homogenization of materials with highly disordered “polycrystalline” microstructure (Zaoui, 2002). One Eshelby-type matrix-inclusion problem is formulated for each and every material phase, irrespective of whether they exhibit finite or infinitesimal volume fractions, see Fig. 3.3. The inclusion has the stiffness, the shape,

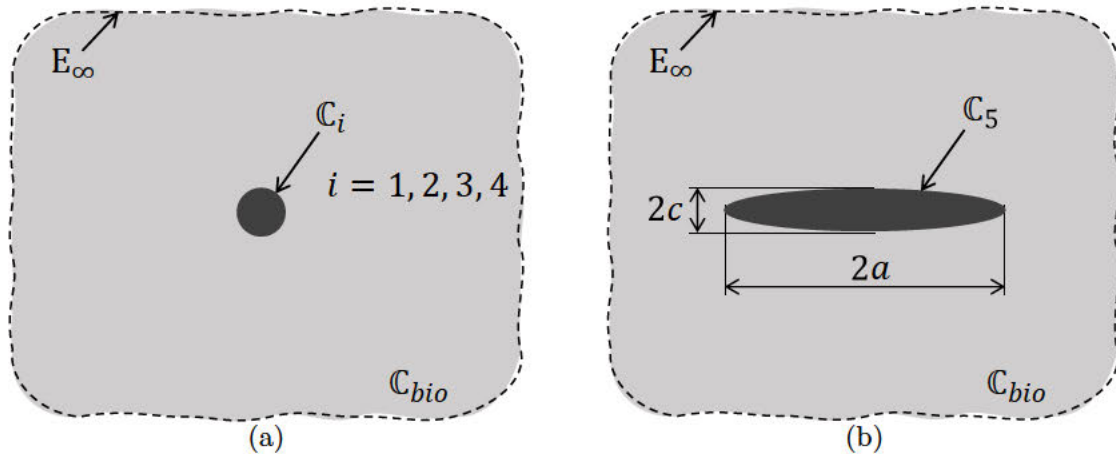


Fig. 3.3. Eshelby-type matrix inclusion problems: (a) spherical inclusion, and (b) oblate spheroid embedded in an infinite matrix with isotropic stiffness \mathbb{C}_{bio} subjected remotely to auxiliary uniform strains \mathbf{E}_∞ .

and the orientation of the material phase it is representing. The stiffness of the infinitely large matrix is equal to that of the homogenized composite (here: Biodentine, index *bio*). This specific property of the self-consistent scheme expresses that the material phases are directly interacting with all constituents of the microheterogeneous material (Zaoui, 2002). Remotely, the matrices of all of the infinitely many Eshelby problems are subjected to *the same* auxiliary strain state \mathbf{E}_∞ . The strains in the inclusions are spatially uniform and read as (Eshelby, 1957)

$$\varepsilon_i = [\mathbb{I} + \mathbb{P}_{sph} : (\mathbb{C}_i - \mathbb{C}_{bio})]^{-1} : \mathbf{E}_\infty, \quad i = 1, 2, \quad (3.21)$$

$$\varepsilon_i(M) = [\mathbb{I} + \mathbb{P}_{sph} : (\mathbb{C}_i(M) - \mathbb{C}_{bio})]^{-1} : \mathbf{E}_\infty, \quad i = 3, 4, \quad M \in \mathbb{R}^{0,+}, \quad (3.22)$$

$$\varepsilon_5(\psi, \vartheta) = [\mathbb{I} + \mathbb{P}_{obl}(\psi, \vartheta) : (\mathbb{C}_5 - \mathbb{C}_{bio})]^{-1} : \mathbf{E}_\infty, \quad \psi \in [0, 2\pi], \quad \vartheta \in [0, \pi]. \quad (3.23)$$

where $\mathbb{R}^{0,+}$ denotes all positive real numbers including zero. \mathbb{P}_{sph} and \mathbb{P}_{obl} denote the Hill tensors of spherical and oblate phases, respectively. \mathbb{P}_{obl} is a function of Euler angles ψ and ϑ , see Pichler et al. (2007) and Fig. 3.4. The stiffness tensors of hydrates, see $\mathbb{C}_i(M)$

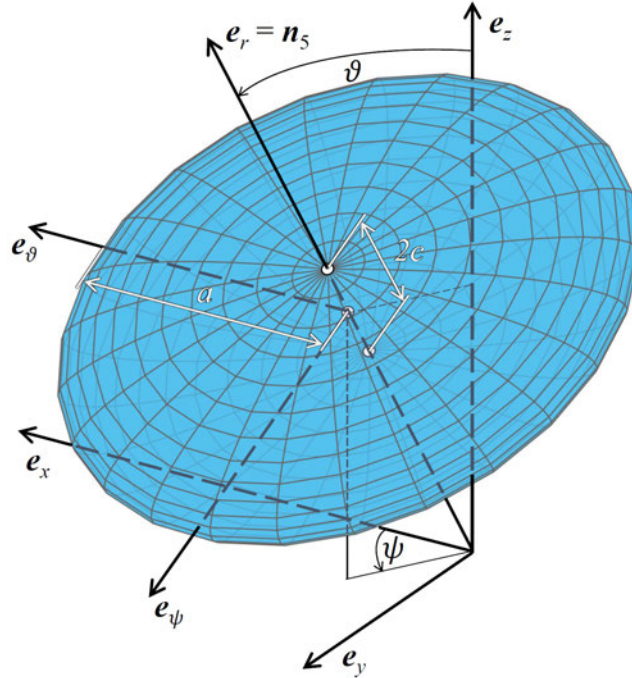


Fig. 3.4. Thin oblate spheroid oriented in ψ, ϑ -direction.

in Eq. (3.22), are parametrized using the indentation modulus M , see Subsection 3.2.6 for details. The stiffness tensor of the microcracks, see \mathbb{C}_5 in Eq. (3.23), is purely volumetric, see Subsection 3.2.3 for more details.

It is a key step to establish relations between the auxiliary Eshelby problems described above and the real representative volume of Biodentine (Zaoui, 2002). To this end, the Eshelby-problem-related inclusion strains according to Eqs. (3.21)–(3.23) are used as estimates of the average strains of the corresponding material phases inside the real representative volume of Biodentine, see Eq. (3.4). The latter satisfy the strain average rule, see Eq. (3.6). When inserting Eqs. (3.21)–(3.23) into Eq. (3.6), the sum extending over two populations of infinitely many hydrate phases turns into integrals, and the sum extending over infinitely many crack phases turns into a double-integral:

$$\begin{aligned} \mathbf{E} &= \sum_{j=1}^2 f_j [\mathbb{I} + \mathbb{P}_{sph} : (\mathbb{C}_j - \mathbb{C}_{bio})]^{-1} : \mathbf{E}_\infty \\ &+ \sum_{j=3}^4 f_j \int_0^\infty \varphi_j(M) [\mathbb{I} + \mathbb{P}_{sph} : (\mathbb{C}_j(M) - \mathbb{C}_{bio})]^{-1} dM : \mathbf{E}_\infty \\ &+ f_5 \int_0^\pi \int_0^{2\pi} [\mathbb{I} + \mathbb{P}_{obl}(\psi, \vartheta) : (\mathbb{C}_5 - \mathbb{C}_{bio})]^{-1} \frac{\sin \vartheta}{4\pi} d\psi d\vartheta : \mathbf{E}_\infty. \end{aligned} \quad (3.24)$$

Eq. (3.24) establishes a link between the loading of the representative volume of Biodentine (= the macrostrain \mathbf{E}) and the loading of the auxiliary Eshelby problems (= the auxiliary

strain \mathbf{E}_∞). Solving Eq. (3.24) for \mathbf{E}_∞ yields

$$\begin{aligned} \mathbf{E}_\infty = & \left\{ \sum_{j=1}^2 f_j [\mathbb{I} + \mathbf{P}_{sph} : (\mathbf{C}_j - \mathbf{C}_{bio})]^{-1} \right. \\ & + \sum_{j=3}^4 f_j \int_0^\infty \varphi_j(M) [\mathbb{I} + \mathbf{P}_{sph} : (\mathbf{C}_j(M) - \mathbf{C}_{bio})]^{-1} dM \\ & \left. + f_5 \int_0^\pi \int_0^{2\pi} [\mathbb{I} + \mathbf{P}_{obl}(\psi, \vartheta) : (\mathbf{C}_5 - \mathbf{C}_{bio})]^{-1} \frac{\sin \vartheta}{4\pi} d\psi d\vartheta \right\}^{-1} : \mathbf{E}. \end{aligned} \quad (3.25)$$

Inserting Eq. (3.25) into Eqs. (3.21)–(3.23) and comparing the results with Eq. (3.9) yields the following estimates for the strain concentration tensors of clinker and zirconia

$$\begin{aligned} \mathbf{A}_i = & [\mathbb{I} + \mathbf{P}_{sph} : (\mathbf{C}_i - \mathbf{C}_{bio})]^{-1} \\ & : \left\{ \sum_{j=1}^2 f_j [\mathbb{I} + \mathbf{P}_{sph} : (\mathbf{C}_j - \mathbf{C}_{bio})]^{-1} \right. \\ & + \sum_{j=3}^4 f_j \int_0^\infty \varphi_j(M) [\mathbb{I} + \mathbf{P}_{sph} : (\mathbf{C}_j(M) - \mathbf{C}_{bio})]^{-1} dM \\ & \left. + f_5 \int_0^\pi \int_0^{2\pi} [\mathbb{I} + \mathbf{P}_{obl}(\psi, \vartheta) : (\mathbf{C}_5 - \mathbf{C}_{bio})]^{-1} \frac{\sin \vartheta}{4\pi} d\psi d\vartheta \right\}^{-1}, \\ & i = 1, 2, \end{aligned} \quad (3.26)$$

of the hydrate phases

$$\begin{aligned} \mathbf{A}_i(M) = & [\mathbb{I} + \mathbf{P}_{sph} : (\mathbf{C}_i(M) - \mathbf{C}_{bio})]^{-1} \\ & : \left\{ \sum_{j=1}^2 f_j [\mathbb{I} + \mathbf{P}_{sph} : (\mathbf{C}_j - \mathbf{C}_{bio})]^{-1} \right. \\ & + \sum_{j=3}^4 f_j \int_0^\infty \varphi_j(N) [\mathbb{I} + \mathbf{P}_{sph} : (\mathbf{C}_j(N) - \mathbf{C}_{bio})]^{-1} dN \\ & \left. + f_5 \int_0^\pi \int_0^{2\pi} [\mathbb{I} + \mathbf{P}_{obl}(\psi, \vartheta) : (\mathbf{C}_5 - \mathbf{C}_{bio})]^{-1} \frac{\sin \vartheta}{4\pi} d\psi d\vartheta \right\}^{-1}, \\ & i = 3, 4, \quad M \in \mathbb{R}^{0,+}, \end{aligned} \quad (3.27)$$

and of the microcracks

$$\begin{aligned}
\mathbb{A}_5(\varphi, \vartheta) &= [\mathbb{I} + \mathbb{P}_{obl}(\psi, \vartheta) : (\mathbb{C}_5 - \mathbb{C}_{bio})]^{-1} \\
&: \left\{ \sum_{j=1}^2 f_j [\mathbb{I} + \mathbb{P}_{sph} : (\mathbb{C}_j - \mathbb{C}_{bio})]^{-1} \right. \\
&\quad + \sum_{j=3}^4 f_j \int_0^\infty \varphi_j(M) [\mathbb{I} + \mathbb{P}_{sph} : (\mathbb{C}_j(M) - \mathbb{C}_{bio})]^{-1} dM \\
&\quad \left. + f_5 \int_0^\pi \int_0^{2\pi} [\mathbb{I} + \mathbb{P}_{obl}(\psi, \vartheta) : (\mathbb{C}_5 - \mathbb{C}_{bio})]^{-1} \frac{\sin \vartheta}{4\pi} d\psi d\vartheta \right\}^{-1}, \\
\psi &\in [0, 2\pi], \quad \vartheta \in [0, \pi].
\end{aligned} \tag{3.28}$$

The homogenized stiffness of Biodentine follows from inserting Eqs. (3.26)–(3.28) into Eq. (3.11) as

$$\begin{aligned}
\mathbb{C}_{bio} &= \left\{ \sum_{i=1}^2 f_i \mathbb{C}_i : [\mathbb{I} + \mathbb{P}_{sph} : (\mathbb{C}_i - \mathbb{C}_{bio})]^{-1} \right. \\
&\quad + \sum_{i=3}^4 f_i \int_0^\infty \varphi_i(M) \mathbb{C}_i(M) : [\mathbb{I} + \mathbb{P}_{sph} : (\mathbb{C}_i(M) - \mathbb{C}_{bio})]^{-1} dM \\
&\quad \left. + f_5 \mathbb{C}_5 : \int_0^\pi \int_0^{2\pi} [\mathbb{I} + \mathbb{P}_{obl}(\psi, \vartheta) : (\mathbb{C}_5 - \mathbb{C}_{bio})]^{-1} \frac{\sin \vartheta}{4\pi} d\psi d\vartheta \right\} \\
&: \left\{ \sum_{j=1}^2 f_j [\mathbb{I} + \mathbb{P}_{sph} : (\mathbb{C}_j - \mathbb{C}_{bio})]^{-1} \right. \\
&\quad + \sum_{j=3}^4 f_j \int_0^\infty \varphi_j(M) [\mathbb{I} + \mathbb{P}_{sph} : (\mathbb{C}_j(M) - \mathbb{C}_{bio})]^{-1} dM \\
&\quad \left. + f_5 \int_0^\pi \int_0^{2\pi} [\mathbb{I} + \mathbb{P}_{obl}(\psi, \vartheta) : (\mathbb{C}_5 - \mathbb{C}_{bio})]^{-1} \frac{\sin \vartheta}{4\pi} d\psi d\vartheta \right\}^{-1}.
\end{aligned} \tag{3.29}$$

3.2.3 Transition to flat circular slit cracks

Microcracks are invisible in micrographs of Biodentine (Dohnalík et al., 2021). This implies that the cracks are closed. Their volume fraction is zero. Thus, the effect of closed cracks on the overall material behavior cannot be traced back to their volume fraction. Instead, the crack density parameter of Budiansky and O’Connell (1976) is introduced, see also Pensée et al. (2002); Deudé et al. (2002). To this end, cracks are first represented as thin oblate spheroids, with a as the larger half-diameter, c as the smaller half-diameter, and very small aspect ratio $X = c/a \ll 1$. The volume of one such spheroid reads as: $4\pi a^2 c/3$. Thus, the

volume fraction of thin spheroidal cracks inside a representative volume of Biodentine amounts to

$$f_5 = \frac{N_{cr}}{V_{bio}} \frac{4\pi a^2 c}{3}, \quad (3.30)$$

where N_{cr} denotes to number of cracks within one representative volume V_{bio} of Biodentine. Introducing the dimensionless crack density parameter as $\omega = N_{cr} a^3 / V_{bio}$, Eq. (3.30) can be re-written as

$$f_5 = \frac{4\pi\omega}{3} X. \quad (3.31)$$

The Hill tensor \mathbb{P}_{obl} can be expressed as the Eshelby tensor \mathbb{S}_{obl} double-contracted with the inverse of the stiffness tensor of Biodentine (Dormieux et al., 2006):

$$\mathbb{P}_{obl} = \mathbb{S}_{obl} : (\mathbb{C}_{bio})^{-1}, \quad (3.32)$$

where \mathbb{S}_{obl} is a function of the aspect ratio X , see [Appendix 3.C](#). The stiffness tensor \mathbb{C}_5 is purely volumetric, because the shear stiffness of closed cracks vanishes (Dormieux et al., 2006)

$$\mathbb{C}_5 = 3k_5 \mathbb{I}^{vol}. \quad (3.33)$$

Because of the following limit case $X \rightarrow 0$, the actual value of k_5 does not matter, as long as it is positive and finite: $0 < k_5 < \infty$, see Dormieux et al. (2006). Inserting Eqs. (3.31)–(3.33) into the expression in the last line of Eq. (3.29), and subjecting the result to the limit $X \rightarrow 0$, which expresses that the volume occupied by closed cracks is negligibly small, yields (Dormieux et al., 2006)

$$\begin{aligned} \lim_{X \rightarrow 0} f_5(X) & \int_0^\pi \int_0^{2\pi} \left[\mathbb{I} + \mathbb{P}_{obl}(X, \psi, \vartheta) : (\mathbb{C}_5 - \mathbb{C}_{bio}) \right]^{-1} \frac{\sin \vartheta}{4\pi} d\psi d\vartheta \\ & = \frac{4\pi\omega}{3} T_{dev} \mathbb{I}^{dev}, \end{aligned} \quad (3.34)$$

with

$$T_{dev} = \frac{8(3k_{bio} + 4g_{bio})}{15\pi(3k_{bio} + 2g_{bio})}. \quad (3.35)$$

The third line in Eq. (3.29) vanishes, because it is equal to the *volumetric* stiffness tensor \mathbb{C}_5 , see Eq. (3.33), double-contracted with the expression on the left-hand-side of Eq. (3.34), which is *deviatoric*, see also Eq. (3.17). Thus Eq. (3.29) reads for closed cracks with crack

density parameter ω :

$$\begin{aligned}
\mathbf{C}_{bio} = & \left\{ \sum_{i=1}^2 f_i \mathbf{C}_i : [\mathbb{I} + \mathbb{P}_{sph} : (\mathbf{C}_i - \mathbf{C}_{bio})]^{-1} \right. \\
& + \left. \sum_{i=3}^4 f_i \int_0^\infty \varphi_i(M) \mathbf{C}_i(M) : [\mathbb{I} + \mathbb{P}_{sph} : (\mathbf{C}_i(M) - \mathbf{C}_{bio})]^{-1} dM \right\} \\
& : \left\{ \sum_{j=1}^2 f_j [\mathbb{I} + \mathbb{P}_{sph} : (\mathbf{C}_j - \mathbf{C}_{bio})]^{-1} \right. \\
& + \left. \sum_{j=3}^4 f_j \int_0^\infty \varphi_j(M) [\mathbb{I} + \mathbb{P}_{sph} : (\mathbf{C}_j(M) - \mathbf{C}_{bio})]^{-1} dM \right. \\
& \left. + \frac{4\pi\omega}{3} T_{dev} \mathbb{I}^{dev} \right\}^{-1}. \tag{3.36}
\end{aligned}$$

3.2.4 Scalar expressions for the homogenized bulk and shear moduli

The Hill tensor \mathbb{P}_{sph} can be expressed as the Eshelby tensor \mathbb{S}_{sph} double-contracted with the inverse of the stiffness tensor of Biodentine (Dormieux et al., 2006):

$$\mathbb{P}_{sph} = \mathbb{S}_{sph} : (\mathbf{C}_{bio})^{-1}. \tag{3.37}$$

Because \mathbb{S}_{sph} is isotropic, it can be expressed as

$$\mathbb{S}_{sph} = S_{vol} \mathbb{I}^{vol} + S_{dev} \mathbb{I}^{dev}, \tag{3.38}$$

with

$$S_{vol} = \frac{3k_{bio}}{3k_{bio} + 4g_{bio}}, \tag{3.39}$$

$$S_{dev} = \frac{6(k_{bio} + 2g_{bio})}{5(3k_{bio} + 4g_{bio})}. \tag{3.40}$$

All tensors in Eqs. (3.36) and (3.37) are isotropic. They can be subdivided into volumetric and deviatoric parts. Consideration of Eqs. (3.15)–(3.18) together with Eqs. (3.14), (3.37),

and (3.40) in Eq. (3.36) yields

$$k_{bio} = \left\{ \sum_{i=1}^2 \frac{f_i k_i}{1 + \frac{S_{vol}(k_i - k_{bio})}{k_{bio}}} + \sum_{i=3}^4 f_i \int_0^\infty \frac{\varphi_i(M) k_i(M)}{1 + \frac{S_{vol}(k_i(M) - k_{bio})}{k_{bio}}} dM \right\} \\ \times \left\{ \sum_{i=1}^2 \frac{f_i}{1 + \frac{S_{vol}(k_i - k_{bio})}{k_{bio}}} + \sum_{i=3}^4 f_i \int_0^\infty \frac{\varphi_i(M)}{1 + \frac{S_{vol}(k_i(M) - k_{bio})}{k_{bio}}} dM \right\}^{-1}, \quad (3.41)$$

$$g_{bio} = \left\{ \sum_{i=1}^2 \frac{f_i g_i}{1 + \frac{S_{dev}(g_i - g_{bio})}{g_{bio}}} + \sum_{i=3}^4 f_i \int_0^\infty \frac{\varphi_i(M) g_i(M)}{1 + \frac{S_{dev}(g_i(M) - g_{bio})}{g_{bio}}} dM \right\} \\ \times \left\{ \sum_{i=1}^2 \frac{f_i}{1 + \frac{S_{dev}(g_i - g_{bio})}{g_{bio}}} + \sum_{i=3}^4 f_i \int_0^\infty \frac{\varphi_i(M)}{1 + \frac{S_{dev}(g_i(M) - g_{bio})}{g_{bio}}} dM \right. \\ \left. + \frac{4\pi\omega}{3} T_{dev} \right\}^{-1}. \quad (3.42)$$

The *scalar* Eqs. (3.41) and (3.42) allow for an iterative determination of the homogenized bulk and shear moduli of Biodentine.

3.2.5 Scalar expressions for volumetric and deviatoric strain and stress tensor components

The strain concentration tensors of the spherical solid phases are also isotropic

$$\mathbb{A}_i = A_{vol,i} \mathbb{I}^{vol} + A_{dev,i} \mathbb{I}^{dev}. \quad (3.43)$$

The volumetric and deviatoric components of the strain concentrations tensors of zirconia ($i = 1$) and clinker ($i = 2$) follow from Eq. (3.26) as

$$A_{vol,i} = \frac{1}{1 + \frac{S_{vol}(k_i - k_{bio})}{k_{bio}}} \left\{ \sum_{i=1}^2 \frac{f_i}{1 + \frac{S_{vol}(k_i - k_{bio})}{k_{bio}}} \right. \\ \left. + \sum_{i=3}^4 f_i \int_0^\infty \frac{\varphi_i(M)}{1 + \frac{S_{vol}(k_i(M) - k_{bio})}{k_{bio}}} dM \right\}^{-1}, \quad (3.44)$$

$$A_{dev,i} = \frac{1}{1 + \frac{S_{dev}(g_i - g_{bio})}{g_{bio}}} \left\{ \sum_{i=1}^2 \frac{f_i}{1 + \frac{S_{dev}(g_i - g_{bio})}{g_{bio}}} \right. \\ \left. + \sum_{i=3}^4 f_i \int_0^\infty \frac{\varphi_i(M)}{1 + \frac{S_{dev}(g_i(M) - g_{bio})}{g_{bio}}} dM + \frac{4\pi\omega}{3} T_{dev} \right\}^{-1}. \quad (3.45)$$

The volumetric and deviatoric components of the strain concentrations tensors of HDCR ($i = 3$) and LDCR ($i = 4$) hydrates follow from Eq. (3.27) as

$$A_{vol,i}(M) = \frac{1}{1 + \frac{S_{vol}(k_i(M) - k_{bio})}{k_{bio}}} \left\{ \sum_{i=1}^2 \frac{f_i}{1 + \frac{S_{vol}(k_i - k_{bio})}{k_{bio}}} + \sum_{i=3}^4 f_i \int_0^\infty \frac{\varphi_i(M)}{1 + \frac{S_{vol}(k_i(M) - k_{bio})}{k_{bio}}} dM \right\}^{-1}, \quad (3.46)$$

$$A_{dev,i}(M) = \frac{1}{1 + \frac{S_{dev}(g_i(M) - g_{bio})}{g_{bio}}} \left\{ \sum_{i=1}^2 \frac{f_i}{1 + \frac{S_{dev}(g_i - g_{bio})}{g_{bio}}} + \sum_{i=3}^4 f_i \int_0^\infty \frac{\varphi_i(M)}{1 + \frac{S_{dev}(g_i(M) - g_{bio})}{g_{bio}}} dM + \frac{4\pi\omega}{3} T_{dev} \right\}^{-1}, \quad (3.47)$$

where $M \in \mathbb{R}^{0,+}$. Strain concentration tensors of the closed cracks will be discussed in Subsection 3.3.4.

The stress concentration tensors of the spherical solid phases are also isotropic

$$\mathbb{B}_i = B_{vol,i} \mathbb{I}^{vol} + B_{dev,i} \mathbb{I}^{dev}. \quad (3.48)$$

Accounting for the isotropy of the tensors in Eq. (3.13) delivers

$$B_{vol,i} = \frac{k_i}{k_{bio}} A_{vol,i}, \quad (3.49)$$

$$B_{dev,i} = \frac{g_i}{g_{bio}} A_{dev,i}, \quad (3.50)$$

with k_i and g_i being the bulk and shear moduli of i -th phase, k_{bio} and g_{bio} are bulk and shear moduli of the homogenized composite Biodentine. The volumetric and deviatoric components of the stress concentrations tensors of zirconia ($i = 1$) and clinker ($i = 2$) follow from insertion of Eqs. (3.44) and (3.45) into Eqs. (3.49) and (3.50), respectively, as

$$B_{vol,i} = \frac{k_i/k_{bio}}{1 + \frac{S_{vol}(k_i - k_{bio})}{k_{bio}}} \left\{ \sum_{i=1}^2 \frac{f_i}{1 + \frac{S_{vol}(k_i - k_{bio})}{k_{bio}}} + \sum_{i=3}^4 f_i \int_0^\infty \frac{\varphi_i(M)}{1 + \frac{S_{vol}(k_i(M) - k_{bio})}{k_{bio}}} dM \right\}^{-1}, \quad (3.51)$$

$$B_{dev,i} = \frac{g_i/g_{bio}}{1 + \frac{S_{dev}(g_i - g_{bio})}{g_{bio}}} \left\{ \sum_{i=1}^2 \frac{f_i}{1 + \frac{S_{dev}(g_i - g_{bio})}{g_{bio}}} + \sum_{i=3}^4 f_i \int_0^\infty \frac{\varphi_i(M)}{1 + \frac{S_{dev}(g_i(M) - g_{bio})}{g_{bio}}} dM + \frac{4\pi\omega}{3} T_{dev} \right\}^{-1}. \quad (3.52)$$

The volumetric and deviatoric components of the stress concentrations tensors of HDCR ($i = 3$) and LDCR ($i = 4$) hydrates from insertion of Eqs. (3.46) and (3.47) into Eqs. (3.49)

and (3.50), respectively, as

$$B_{vol,i}(M) = \frac{k_i(M)/k_{bio}}{1 + \frac{S_{vol}(k_i(M)-k_{bio})}{k_{bio}}} \left\{ \sum_{i=1}^2 \frac{f_i}{1 + \frac{S_{vol}(k_i-k_{bio})}{k_{bio}}} + \sum_{i=3}^4 f_i \int_0^{\infty} \frac{\varphi_i(M)}{1 + \frac{S_{vol}(k_i(M)-k_{bio})}{k_{bio}}} dM \right\}^{-1}, \quad (3.53)$$

$$B_{dev,i}(M) = \frac{g_i(M)/g_{bio}}{1 + \frac{S_{dev}(g_i(M)-g_{bio})}{g_{bio}}} \left\{ \sum_{i=1}^2 \frac{f_i}{1 + \frac{S_{dev}(g_i-g_{bio})}{g_{bio}}} + \sum_{i=3}^4 f_i \int_0^{\infty} \frac{\varphi_i(M)}{1 + \frac{S_{dev}(g_i(M)-g_{bio})}{g_{bio}}} dM + \frac{4\pi\omega}{3} T_{dev} \right\}^{-1}, \quad (3.54)$$

where $M \in \mathbb{R}^{0,+}$.

3.2.6 Bulk and shear moduli of the hydrates, as functions of the indentation modulus

Evaluation of the integrals in Eqs. (3.41), (3.42), (3.44)–(3.47), and (3.51)–(3.54) requires expressions for the bulk and shear moduli of the hydrates, as functions of the indentation modulus. The latter is a function of the elastic stiffness properties of the nanoindentation-probed domain and of the diamond tip of the indenter. For an isotropic domain, this function reads as (Oliver and Pharr, 1992)

$$\frac{1}{M} = \frac{1 - \nu_h^2}{E} + \frac{1 - 0.07^2}{1141 \text{ GPa}}, \quad (3.55)$$

where E and ν_h denote the modulus of elasticity and Poisson's ratio of the hydrates. Herein, ν_h is assumed to be constant.² In other words, the distribution of indentation modulus is related to a corresponding distribution of the modulus of elasticity, E . The latter distribution follows from solving Eq. (3.55) for E :

$$E(M) = \frac{1 - \nu_h^2}{\frac{1}{M} - \frac{1 - 0.07^2}{1141 \text{ GPa}}}. \quad (3.56)$$

The sought bulk moduli $k_i(M)$ and the shear moduli $g_i(M)$ follow from standard relations for isotropic elastic media:

$$k_i(M) = \frac{E(M)}{3(1 - 2\nu_h)}, \quad i = 3, 4, \quad (3.57)$$

$$g_i(M) = \frac{E(M)}{2(1 + \nu_h)}, \quad i = 3, 4, \quad (3.58)$$

see also Fig. 3.5.

²The value of ν_h will be identified in Subsection 3.2.7.

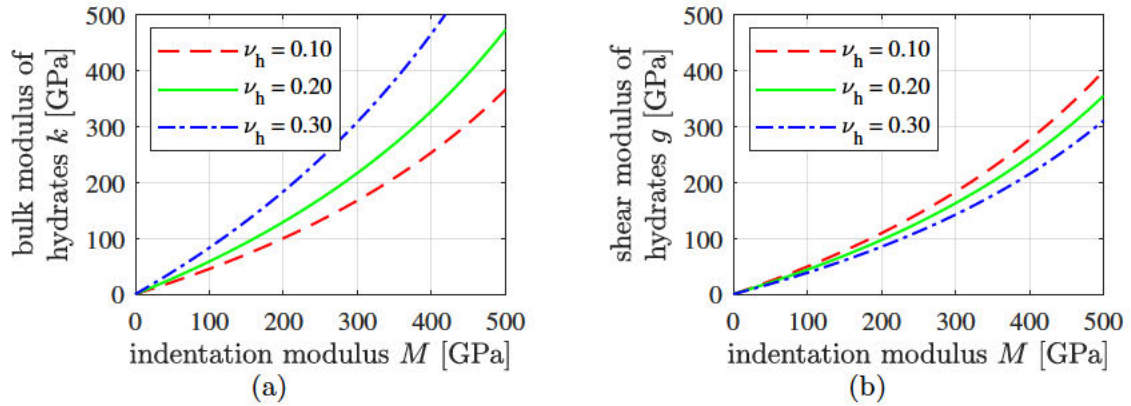


Fig. 3.5. (a) bulk and (b) shear modulus of the hydrates as a function of the indentation modulus, for three different values of Poisson's ratio of the hydrates.

3.2.7 Identification of crack density of Biodentine and Poisson's ratio of hydrates

In order to identify the values of the crack density of Biodentine and of Poisson's ratio of the hydrates, the search intervals $\omega = [0.5 ; 2.0]$ and $\nu_h = [0.15 ; 0.30]$ are subdivided into 7 equidistant values, defining a search grid. For all 49 combination of values (= grid points), $k_{bio}(\omega, \nu_h)$ and $g_{bio}(\omega, \nu_h)$ are computed according to Eqs. (3.41) and (3.42). Because they are implicit expressions of the homogenized bulk and shear moduli of Biodentine, k_{bio} and g_{bio} are quantified iteratively, as outlined in the flowchart given in Table 3.3.

Table 3.3

Flowchart for the computation of k_{bio} and g_{bio} according to Eqs. (3.41) and (3.42), respectively.

1. Define numerical values of the crack density parameter ω and of Poisson's ratio of the hydrates, ν_h .
2. Define initial values of k_{bio} and g_{bio} as arbitrary positive numbers; for example $k_{bio} = 4.2$ GPa and $g_{bio} = 2.5$ GPa.
3. Set the tolerance value tol equal to 10^{-10} .
4. Save k_{bio} as k_{bio}^{old} and g_{bio} as g_{bio}^{old} .
5. Compute T_{dev} , S_{vol} , S_{dev} according to Eqs. (3.35), (3.39), (3.40).
6. Evaluate the integrals in Eqs. (3.41) and (3.42) based on $\varphi_3(M)$ and $\varphi_4(M)$ according to Eq. (3.19) with values of μ_3 , σ_3 , μ_4 , σ_4 from Table 3.2, as well as $k_3(M)$, $g_3(M)$, $k_4(M)$, $g_4(M)$ according to Eqs. (3.57) and (3.58), with $E(M)$ according to Eq. (3.56).
7. Evaluate the sums in Eqs. (3.41) and (3.42) based on f_1 , f_2 , f_3 , f_4 , k_1 , g_1 , k_2 , g_2 from Table 3.2.
8. Quantify k_{bio} and g_{bio} according to Eqs. (3.41) and (3.42).
9. Determine the convergence ratio according to

$$c = \frac{\|k_{bio} - k_{bio}^{old}\|}{k_{bio}^{old}} + \frac{\|g_{bio} - g_{bio}^{old}\|}{g_{bio}^{old}}.$$

10. If $c < tol$ then stop the iteration; else go to 4. (= start the next iteration step).

For every grid point, the square root of the sum of squared errors is quantified based

on the computed homogenized stiffness moduli and their experimental counterparts, see the ultrasonics-derived values in Eqs. (3.1) and (3.2):

$$\varepsilon_{SRSS} = \sqrt{\left[k_{bio}^{exp} - k_{bio}(\omega, \nu_h)\right]^2 + \left[g_{bio}^{exp} - g_{bio}(\omega, \nu_h)\right]^2}. \quad (3.59)$$

The obtained error surface exhibits one minimum in the vicinity of $\omega \approx 0.78$ and $\nu_h \approx 0.20$, see also Fig. 3.6. The optimal solution is found iteratively, using a method based on search intervals

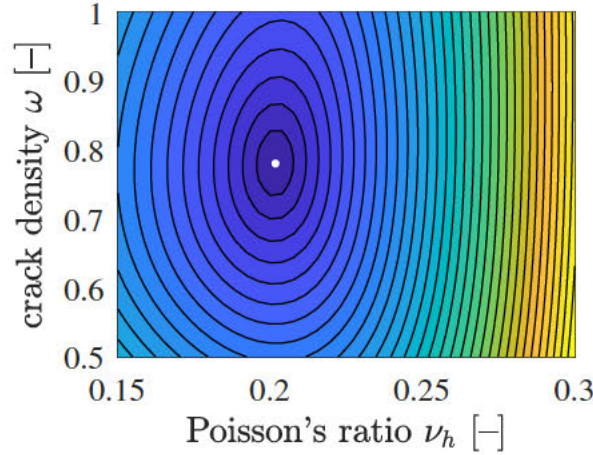


Fig. 3.6. Square root of the sum of squared errors (3.59), quantifying the difference between computed homogenized stiffness moduli, see Eqs. (3.41) and (3.42) as well as Table 3.3, and their experimental counterparts, see Eqs. (3.1) and (3.2).

which are progressively refined and shifted, see Irfan-ul-Hassan et al. (2016); Dohnalík et al. (2021). The lognormal microelasticity model reproduces the ultrasonics-derived macrostiffness moduli when using the following values of the crack density parameter and of Poisson's ratio of LDCR and HDCR hydrates as input:

$$\omega = 0.7802, \quad (3.60)$$

$$\nu_h = 0.2017, \quad (3.61)$$

see also Fig. 3.7. The numerical values of the integrals in Eqs. (3.41), (3.42) and (3.44)–(3.47), obtained with $k_{bio} = 38.4$ GPa, $g_{bio} = 14.1$ GPa, and $\nu_h = 0.2017$, are listed in Appendix 3.B.

3.3 Application of the lognormal microelasticity model: strain and stress fluctuations

3.3.1 Distributions of strain concentration tensor components of the two populations of hydrates

Probability distribution functions for strain concentration tensor components of both populations of hydrates are computed as follows. Eq. (3.19) provides access to the probability density as a function of the indentation modulus. Eqs. (3.46) and (3.47) allow for computing the volumetric and deviatoric components of the strain concentration tensor as a function of the indentation modulus. Combining Eq. (3.19) with Eq. (3.46) and Eq. (3.47), respectively, allows for producing parameter plots showing probability density over strain concentration

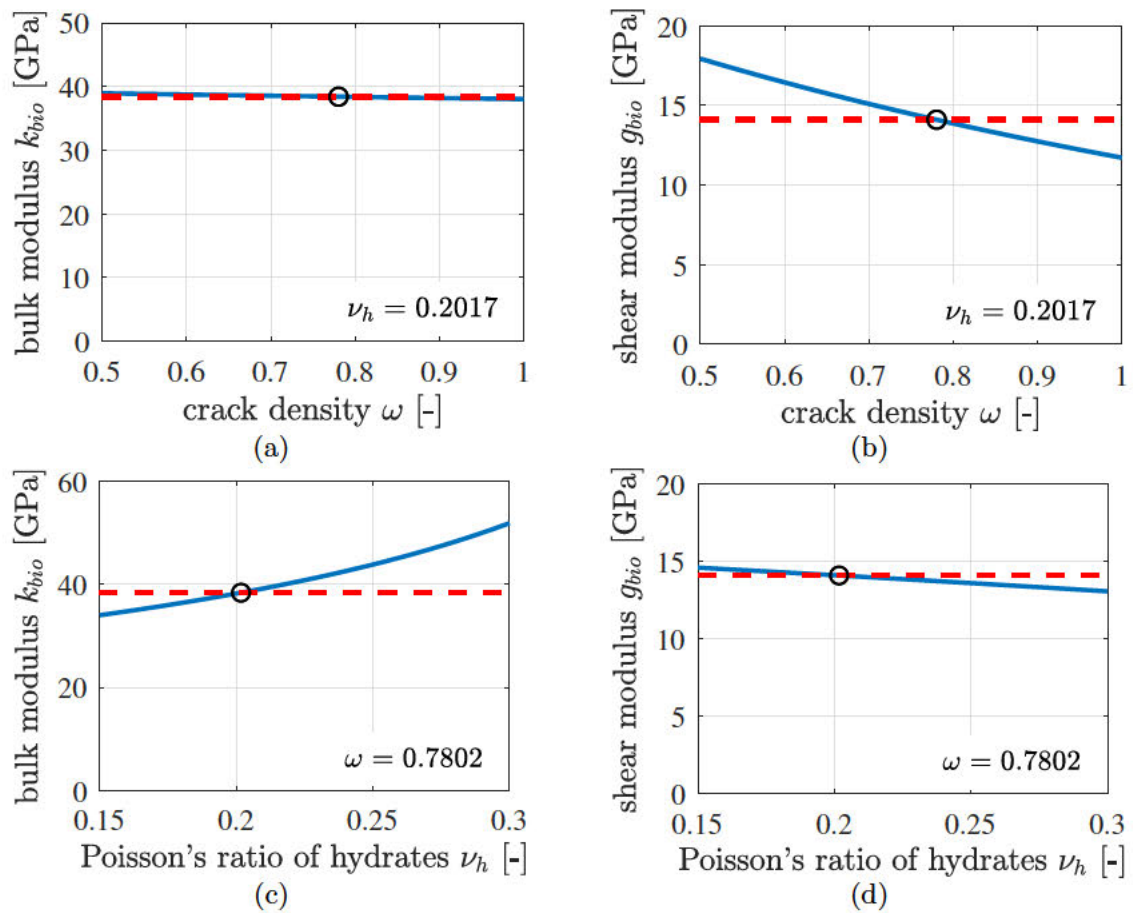


Fig. 3.7. Homogenized stiffness moduli k_{bio} and g_{bio} according to Eqs. (3.41) and (3.42), as functions of the crack density of Biodentine and Poisson's ratio of the hydrates, see the solid blue lines, and ultrasonics-derived counterparts according to Eqs. (3.1) and (3.2), see the red dashed lines; the circles mark the optimal solutions, see also Eqs. (3.60) and (3.61).

tensor components, with the indentation modulus as the parameter. Normalizing the obtained parameter plots such that the area under the graphs becomes equal to 1, delivers probability density functions for the strain concentration tensor components, see Fig. 3.8. The probability

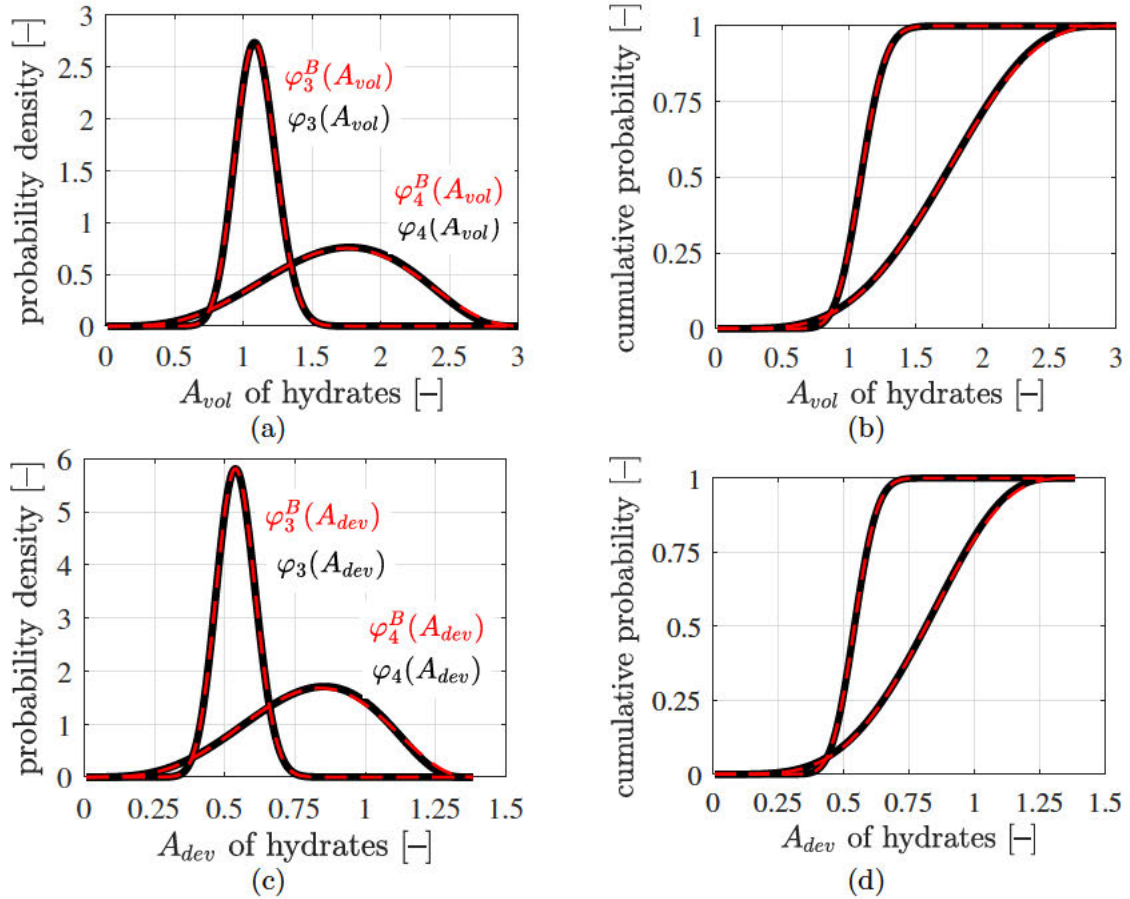


Fig. 3.8. Results of the lognormal microelasticity model (black graphs): statistical distributions of volumetric and deviatoric components of the strain concentration tensors of LDCR hydrates and of HDCR hydrates: (a) and (c) show probability density distributions, (b) and (d) cumulative distribution functions. The best fits of generalized beta-distributions to the statistical distributions are the red dashed graphs, see Eqs. (3.70) and (3.71) as well as the Beta distributions parameters listed in Table 3.6.

densities of A_{vol} and A_{dev} of the LDCR hydrates are left-skewed functions. The corresponding results obtained for the HDCR hydrates, in turn, are reminiscent of Gaussian distributions.

It is interesting to quantify the strain concentration tensor components averaged over each one of the two populations of hydrates. Notably, the volume average rule applies for strain concentration tensors (Zaoui, 2002). Thus, the population-averaged volumetric and deviatoric strain concentration tensor components read as

$$\overline{A_{vol,j}} = \int_0^{\infty} \varphi_j(M) A_{vol,j}(M) dM \quad j = 3, 4, \quad (3.62)$$

$$\overline{A_{dev,j}} = \int_0^{\infty} \varphi_j(M) A_{dev,j}(M) dM \quad j = 3, 4. \quad (3.63)$$

Inserting $A_{vol,j}(M)$ and $A_{dev,j}(M)$ according to Eqs. (3.46) and (3.47), respectively, into Eqs. (3.62) and (3.63) yields

$$\overline{A_{vol,j}} = \int_0^{\infty} \frac{\varphi_j(M)}{1 + \frac{S_{vol}(k_i(M) - k_{bio})}{k_{bio}}} dM \times \left\{ \sum_{i=1}^2 \frac{f_i}{1 + \frac{S_{vol}(k_i - k_{bio})}{k_{bio}}} + \sum_{i=3}^4 f_i \int_0^{\infty} \frac{\varphi_i(M)}{1 + \frac{S_{vol}(k_i(M) - k_{bio})}{k_{bio}}} dM \right\}^{-1}, \quad (3.64)$$

$$\overline{A_{dev,j}} = \int_0^{\infty} \frac{\varphi_j(M)}{1 + \frac{S_{dev}(g_i(M) - g_{bio})}{g_{bio}}} dM \times \left\{ \sum_{i=1}^2 \frac{f_i}{1 + \frac{S_{dev}(g_i - g_{bio})}{g_{bio}}} + \sum_{i=3}^4 f_i \int_0^{\infty} \frac{\varphi_i(M)}{1 + \frac{S_{dev}(g_i(M) - g_{bio})}{g_{bio}}} dM + \frac{4\pi\omega}{3} T_{dev} \right\}^{-1}. \quad (3.65)$$

Evaluation of the strain concentration tensor components A_{vol} and A_{dev} of zirconia and clinker according to Eqs. (3.44) and (3.45), as well as the average strain concentration tensor components $\overline{A_{vol}}$ and $\overline{A_{dev}}$ of HDCR and LDCR hydrates according to Eqs. (3.64) and (3.65), yields numerical values listed in Table 3.4. These values quantify the expected trend that the

Table 3.4

Results of the lognormal microelasticity model: (population-averaged) strain concentration tensors components of the four types of solid constituents of Biodentine.

constituent of Biodentine	(average) strain concentration tensor components		source
zirconia	$A_{vol,1} = 0.3017$	$A_{dev,1} = 0.2352$	Eqs. (3.44) and (3.45)
clinker	$A_{vol,2} = 0.4223$	$A_{dev,2} = 0.3192$	Eqs. (3.44) and (3.45)
HDCR hydrates	$\overline{A_{vol,3}} = 1.0551$	$\overline{A_{dev,3}} = 0.5248$	Eqs. (3.64) and (3.65)
LDCR hydrates	$\overline{A_{vol,4}} = 1.3207$	$\overline{A_{dev,4}} = 0.6428$	Eqs. (3.64) and (3.65)

strains experienced by the material constituents increase with decreasing stiffness.

3.3.2 Distributions of stress concentration tensor components of the two populations of hydrates

Combining Eq. (3.19) with Eq. (3.53) and Eq. (3.54), respectively, allows for producing parameter plots showing probability density over stress concentration tensor components, with the indentation modulus as the parameter. Normalizing the obtained parameter plots such that the area under the graphs becomes equal to 1, delivers probability density functions for the stress concentration tensor components, see Fig. 3.9. The probability densities of B_{vol} and B_{dev} of the LDCR hydrates are right-skewed functions. The corresponding results obtained for the HDCR hydrates, in turn, are reminiscent of Gaussian distributions.

The stress concentration tensor components averaged over each one of the two populations of hydrates are quantified based on the volume average rule for stress concentration tensors

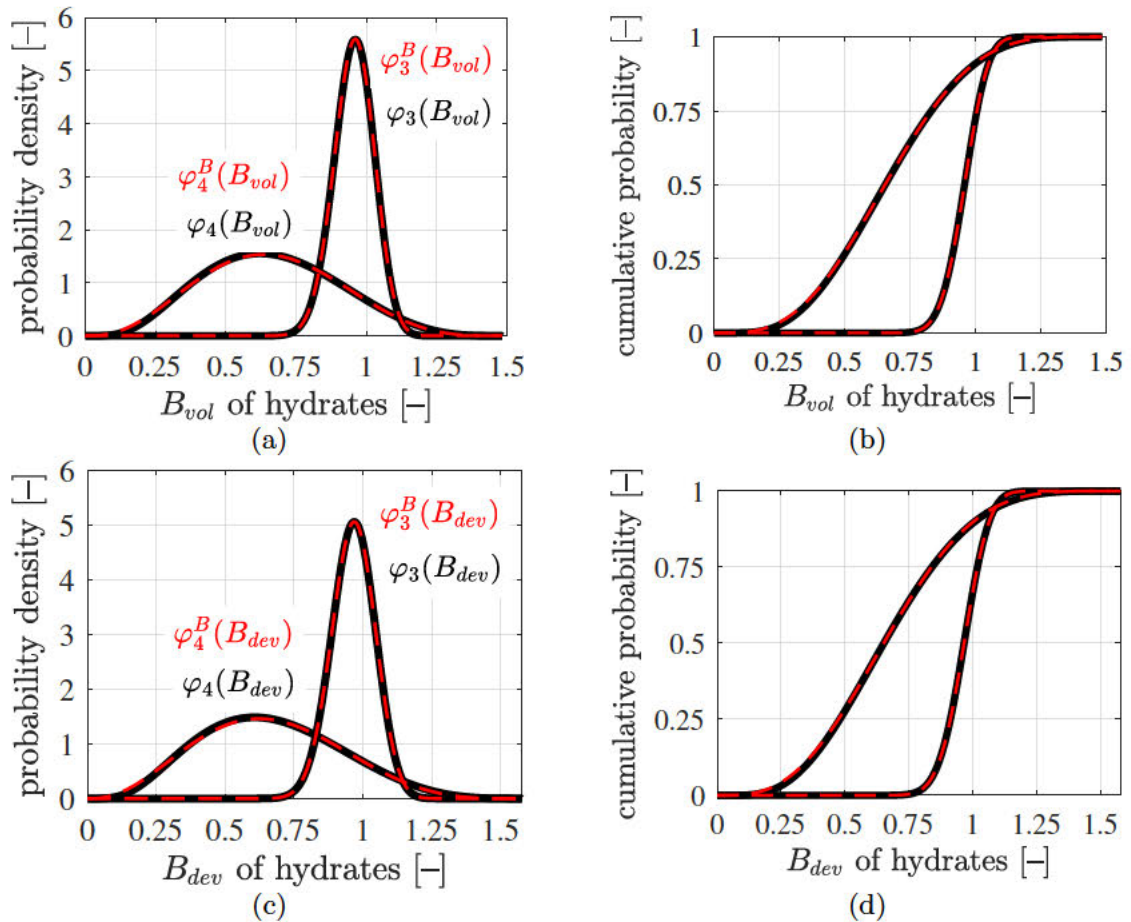


Fig. 3.9. Results of the lognormal microelasticity model (black graphs): statistical distributions of volumetric and deviatoric components of the stress concentration tensors of LDCR hydrates and of HDCR hydrates: (a) and (c) show probability density distributions, (b) and (d) cumulative distribution functions. The best fits of generalized beta-distributions to the statistical distributions are the red dashed graphs, see Eqs. (3.70) and (3.71) as well as the Beta distributions parameters listed in Table 3.7.

(Zaoui, 2002):

$$\overline{B_{vol,j}} = \int_0^{\infty} \varphi_j(M) B_{vol,j}(M) dM, \quad j = 3, 4, \quad (3.66)$$

$$\overline{B_{dev,j}} = \int_0^{\infty} \varphi_j(M) B_{dev,j}(M) dM, \quad j = 3, 4. \quad (3.67)$$

Inserting $B_{vol,j}(M)$ and $B_{dev,j}(M)$ according to Eqs. (3.53) and (3.54), respectively, into Eqs. (3.66) and (3.67) yields

$$\overline{B_{vol,j}} = \frac{1}{k_{bio}} \int_0^{\infty} \frac{\varphi_j(M) k_j(M)}{1 + \frac{S_{vol}(k_i(M) - k_{bio})}{k_{bio}}} dM \times \left\{ \sum_{i=1}^2 \frac{f_i}{1 + \frac{S_{vol}(k_i - k_{bio})}{k_{bio}}} + \sum_{i=3}^4 f_i \int_0^{\infty} \frac{\varphi_i(M)}{1 + \frac{S_{vol}(k_i(M) - k_{bio})}{k_{bio}}} dM \right\}^{-1}, \quad (3.68)$$

$$\overline{B_{dev,j}} = \frac{1}{g_{bio}} \int_0^{\infty} \frac{\varphi_j(M) g_j(M)}{1 + \frac{S_{dev}(g_i(M) - g_{bio})}{g_{bio}}} dM \times \left\{ \sum_{i=1}^2 \frac{f_i}{1 + \frac{S_{dev}(g_i - g_{bio})}{g_{bio}}} + \sum_{i=3}^4 f_i \int_0^{\infty} \frac{\varphi_i(M)}{1 + \frac{S_{dev}(g_i(M) - g_{bio})}{g_{bio}}} dM + \frac{4\pi\omega}{3} T_{dev} \right\}^{-1}. \quad (3.69)$$

Evaluation of the stress concentration tensor components B_{vol} and B_{dev} of zirconia and clinker according to Eqs. (3.51) and (3.52), as well as the average stress concentration tensor components $\overline{B_{vol}}$ and $\overline{B_{dev}}$ of HDCR and LDCR hydrates according to Eqs. (3.68) and (3.69), yields numerical values listed in Table 3.5. These values quantify the expected trend that

Table 3.5

Results of the lognormal microelasticity model: (population-averaged) stress concentration tensors components of the four types of solid constituents of Biodentine.

constituent of Biodentine	(average) stress concentration tensor components		source
zirconia	$B_{vol,1} = 1.3419$	$B_{dev,1} = 1.3152$	Eqs. (3.49) and (3.50)
clinker	$B_{vol,2} = 1.2828$	$B_{dev,2} = 1.2188$	Eqs. (3.49) and (3.50)
HDCR hydrates	$\overline{B_{vol,3}} = 0.9730$	$\overline{B_{dev,3}} = 0.9830$	Eqs. (3.68) and (3.69)
LDCR hydrates	$\overline{B_{vol,4}} = 0.8430$	$\overline{B_{dev,4}} = 0.8476$	Eqs. (3.68) and (3.69)

stresses experienced by the material constituents decrease with decreasing stiffness.

3.3.3 Reproducing the distributions of strain and stress concentration tensor components based on generalized beta-distributions

Probability density functions $\varphi_i(A_{vol})$, $\varphi_i(A_{dev})$, $\varphi_i(B_{vol})$ and $\varphi_i(B_{dev})$ of both populations of hydrates ($i = 3, 4$) can be approximated by means of generalized beta-distributions:

$$\varphi_i^B(y) = \frac{\left(\frac{y-a}{c-a}\right)^{\alpha-1} \left(\frac{c-y}{c-a}\right)^{\beta-1}}{(c-a) \times B(\alpha, \beta)}, \quad (3.70)$$

where y denotes the statistical variable ranging in the interval $[a; c]$, and $B(\alpha, \beta)$ denotes the beta-distribution evaluated for parameters α and β :

$$B(\alpha, \beta) = \frac{\Gamma(\alpha) \Gamma(\beta)}{\Gamma(\alpha + \beta)}, \quad (3.71)$$

where Γ denotes the gamma function (Johnson, 1997; Chaudhry et al., 1997).

Optimal α and β parameters are identified by means of the “Nonlinear Least Squares” method of Matlab, see Tables 3.6 and 3.7 for the results. The lowest coefficient of determina-

Table 3.6

Optimal parameters of generalized beta-distributions, see Eqs. (3.70) and (3.71), approximating the distributions of the volumetric and deviatoric strain concentration tensor components of both populations of hydrates, see also the dashed red lines in Fig. 3.8; R^2 denotes coefficients of determination.

parameter	HDCR hydrates		LDCR hydrates	
	$\varphi_3(A_{vol})$	$\varphi_3(A_{dev})$	$\varphi_4(A_{vol})$	$\varphi_4(A_{dev})$
a	0.0136	0.0071	0.0136	0.0071
c	3.0427	1.3816	3.0427	1.3816
α	35.2406	37.0711	4.6942	4.9316
β	63.8869	58.4258	3.7593	3.5650
R^2	1.0000	1.0000	0.9995	0.9992

Table 3.7

Optimal parameters of generalized beta-distributions, see Eqs. (3.70) and (3.71), approximating the distributions of the volumetric and deviatoric stress concentration tensor components of both populations of hydrates, see also the dashed red lines in Fig. 3.9; R^2 denotes coefficients of determination.

parameter	HDCR hydrates		LDCR hydrates	
	$\varphi_3(B_{vol})$	$\varphi_3(B_{dev})$	$\varphi_4(B_{vol})$	$\varphi_4(B_{dev})$
a	$4.3 \cdot 10^{-5}$	$3.9 \cdot 10^{-5}$	$4.3 \cdot 10^{-5}$	$3.9 \cdot 10^{-5}$
c	1.4829	1.5768	1.4829	1.5768
α	63.8869	58.4258	3.7593	3.5650
β	35.2406	37.0711	4.6942	4.9316
R^2	1.0000	1.0000	0.9995	0.9992

tion, R^2 , amounts to 0.9992 and is obtained for the deviatoric components of strain as well as stress concentration tensors of LDCR hydrates, see Tables 3.6 and 3.7 as well as Figs. 3.8 and 3.9. Notably, the α parameters found for the strain concentration tensor components are identical to the β parameters of the corresponding stress concentration tensor components, and vice versa, because strain and stress concentration tensor components are linearly related via Eqs. (3.49) and (3.50).

3.3.4 Contribution of the microcracks to the stress and strain average rules

Closed microcracks do neither contribute to the stress average rule nor to the *volumetric* part of the strain average rule. Still, they contribute significantly to the *deviatoric* compliance of Biodentine, as will be shown next.

Insertion of Eq. (3.12), into Eq. (3.5) yields the stress average rule expressed in terms of stress concentration tensors:

$$\sum_{i=1}^N f_i \mathbb{B}_i = \mathbb{I}. \quad (3.72)$$

Closed microcracks transfer finite stresses across their microcrack planes. Therefore, their stress concentration tensor components are finite. The volume fraction of closed microcracks is equal to zero. Therefore, closed microcracks have a vanishing contribution to Eq. (3.72). Subdividing this equation into volumetric and deviatoric parts, and consideration of volume fractions according to Table 3.2 as well as (hydrate population-averaged) stress concentration tensor components according to Table 3.5, yields

$$f_1 B_{vol,1} + f_2 B_{vol,2} + f_3 \overline{B_{vol,3}} + f_4 \overline{B_{vol,4}} = 1, \quad (3.73)$$

$$f_1 B_{dev,1} + f_2 B_{dev,2} + f_3 \overline{B_{dev,3}} + f_4 \overline{B_{dev,4}} = 1. \quad (3.74)$$

Similarly, insertion Eq. (3.9) into Eq. (3.4) yields the strain average rule expressed in terms of strain concentration tensors:

$$\sum_{i=1}^N f_i \mathbb{A}_i = \mathbb{I}. \quad (3.75)$$

Because closed microcracks occupy a vanishing volume and because they remain closed also under macroscopic loading, they have a vanishing contribution to the volumetric part of Eq. (3.75):

$$f_1 A_{vol,1} + f_2 A_{vol,2} + f_3 \overline{A_{vol,3}} + f_4 \overline{A_{vol,4}} = 1, \quad (3.76)$$

where volume fractions according to Table 3.2 and (hydrate population-averaged) strain concentration tensor components according to Table 3.4 were used. However, the same approach applied to the deviatoric part of Eq. (3.75) yields:

$$f_1 A_{dev,1} + f_2 A_{dev,2} + f_3 \overline{A_{dev,3}} + f_4 \overline{A_{dev,4}} = 0.5100 \neq 1. \quad (3.77)$$

Eq. (3.77) underlines that closed cracks contribute to the deviatoric compliance of the homogenized material.

In order to quantify the contribution of the microcracks missing in Eq. (3.77), their population-averaged (= orientation-averaged) strain concentration tensor is introduced, while

the cracks are still considered as thin but slightly open oblate spheroids:

$$\begin{aligned} \bar{\mathbb{A}}_5 &= \int_0^\pi \int_0^{2\pi} [\mathbb{I} + \mathbb{P}_{obl}(\psi, \vartheta) : (\mathbb{C}_5 - \mathbb{C}_{bio})]^{-1} \frac{\sin \vartheta}{4\pi} d\psi d\vartheta \\ &: \left\{ \sum_{j=1}^2 f_j [\mathbb{I} + \mathbb{P}_{sph} : (\mathbb{C}_j - \mathbb{C}_{bio})]^{-1} \right. \\ &\quad + \sum_{j=3}^4 f_j \int_0^\infty \varphi_j(M) [\mathbb{I} + \mathbb{P}_{sph} : (\mathbb{C}_j(M) - \mathbb{C}_{bio})]^{-1} dM \\ &\quad \left. + f_5 \int_0^\pi \int_0^{2\pi} [\mathbb{I} + \mathbb{P}_{obl}(\psi, \vartheta) : (\mathbb{C}_5 - \mathbb{C}_{bio})]^{-1} \frac{\sin \vartheta}{4\pi} d\psi d\vartheta \right\}^{-1}. \end{aligned} \quad (3.78)$$

The transition to circular slit cracks refers to the limit case that the aspect ratio of the microcracks approaches zero: $X \rightarrow 0$. In this limit case, the deviatoric component of $\bar{\mathbb{A}}_5$ approaches infinity (Dormieux et al., 2006), while the volume fraction of the population of microcracks, f_5 , approaches zero, such that the product of f_5 and $\bar{\mathbb{A}}_5$ remains finite:

$$\begin{aligned} \lim_{X \rightarrow 0} f_5 \bar{\mathbb{A}}_5 &= \frac{4\pi\omega}{3} T_{dev} \left\{ \sum_{i=1}^2 \frac{f_i}{1 + \frac{S_{dev}(g_i - g_{bio})}{g_{bio}}} \right. \\ &\quad \left. + \sum_{i=3}^4 f_i \int_0^\infty \frac{\varphi_i(M)}{1 + \frac{S_{dev}(g_i(M) - g_{bio})}{g_{bio}}} dM + \frac{4\pi\omega}{3} T_{dev} \right\}^{-1} \mathbb{I}^{dev}. \end{aligned} \quad (3.79)$$

Evaluation of Eq. (3.79) based on $k_{bio} = 38.4$ GPa, $g_{bio} = 14.1$ GPa, T_{dev} from Eq. (3.35), S_{dev} from Eq. (3.40), together with ω from Eq. (3.60), and volume fractions from Table 3.2 yields, under consideration of Eqs. (3.B.7) and (3.B.8):

$$\lim_{X \rightarrow 0} f_5 \bar{\mathbb{A}}_5 = f_5 \bar{A}_{dev,5} \mathbb{I}^{dev} = 0.4899 \mathbb{I}^{dev}. \quad (3.80)$$

Adding $f_5 \bar{A}_{dev,5}$ according to Eq. (3.80) to Eq. (3.77) yields

$$f_1 A_{dev,1} + f_2 A_{dev,2} + f_3 \bar{A}_{dev,3} + f_4 \bar{A}_{dev,4} + f_5 \bar{A}_{dev,5} = 1. \quad (3.81)$$

Eqs. (3.80) and (3.81) underline that almost 50% of the deviatoric compliance of Biodentine results from shear-dislocations of closed microcracks.

3.4 Comparison with piecewise uniform microelasticity models

The developed lognormal microelasticity model accounts for stiffness *distributions* of hydrates, as characterized in a grid nanoindentation testing campaign. Standardly used multiscale models for cementitious materials, in turn, assign characteristic stiffness *constants* to a small number of considered hydrate phases, typically two. This provides the motivation to identify characteristic stiffness constants of HDCR hydrates and LDCR hydrates such that a

piecewise uniform microelasticity model, based on four solid phases and infinitely many crack phases, reproduces the same homogenized stiffness as the *lognormal* microelasticity model described above. In the piecewise uniform microelasticity model, Biodentine is represented as a composite with polycrystalline microstructure in which four spherical solid phases (zirconia, clinker, HDCR hydrates, and LDCR hydrates) and infinitely many crack phases (which are isotropically oriented in space) directly interact with each other, see Fig. 3.10.

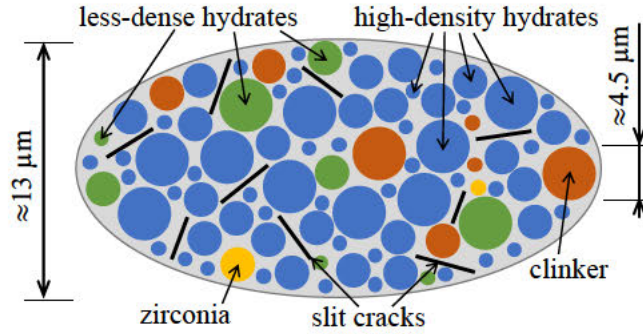


Fig. 3.10. Micromechanical representation of Biodentine (“material organogram”): the two-dimensional sketch shows qualitative properties of a three-dimensional representative volume element of the *piecewise uniform* microelasticity models which account for characteristic stiffness *constants* of two populations of hydrates.

The stiffness constants of zirconia and clinker, the volume fractions of the four solid phases, and the crack density are the same as before, see Table 3.2 and Eq. (3.60). Denoting the characteristic bulk and shear moduli assigned to the two populations of hydrates as k_3 and k_4 as well as g_3 and g_4 , respectively, the expressions for the homogenized bulk and shear moduli according to Eqs. (3.41) and (3.42), those for the strain concentration tensor components according to Eqs. (3.44)–(3.47), and those for the stress concentration tensor components according to Eqs. (3.51)–(3.54) simplify to

$$k_{bio} = \left\{ \sum_{i=1}^4 \frac{f_i k_i}{1 + \frac{S_{vol}(k_i - k_{bio})}{k_{bio}}} \right\} \times \left\{ \sum_{i=1}^4 \frac{f_i}{1 + \frac{S_{vol}(k_i - k_{bio})}{k_{bio}}} \right\}^{-1}, \quad (3.82)$$

$$g_{bio} = \left\{ \sum_{i=1}^4 \frac{f_i g_i}{1 + \frac{S_{dev}(g_i - g_{bio})}{g_{bio}}} \right\} \times \left\{ \sum_{i=1}^4 \frac{f_i}{1 + \frac{S_{dev}(g_i - g_{bio})}{g_{bio}}} + \frac{4\pi\omega}{3} T_{dev} \right\}^{-1}, \quad (3.83)$$

$$A_{vol,j} = \frac{1}{1 + \frac{S_{vol}(k_j - k_{bio})}{k_{bio}}} \times \left\{ \sum_{i=1}^4 \frac{f_i}{1 + \frac{S_{vol}(k_i - k_{bio})}{k_{bio}}} \right\}^{-1}, \quad (3.84)$$

$$A_{dev,j} = \frac{1}{1 + \frac{S_{dev}(g_j - g_{bio})}{g_{bio}}} \times \left\{ \sum_{i=1}^4 \frac{f_i}{1 + \frac{S_{dev}(g_i - g_{bio})}{g_{bio}}} + \frac{4\pi\omega}{3} T_{dev} \right\}^{-1}, \quad (3.85)$$

$$B_{vol,j} = \frac{k_j/k_{bio}}{1 + \frac{S_{vol}(k_j - k_{bio})}{k_{bio}}} \times \left\{ \sum_{i=1}^4 \frac{f_i}{1 + \frac{S_{vol}(k_i - k_{bio})}{k_{bio}}} \right\}^{-1}, \quad (3.86)$$

$$B_{dev,j} = \frac{g_j/g_{bio}}{1 + \frac{S_{dev}(g_j - g_{bio})}{g_{bio}}} \times \left\{ \sum_{i=1}^4 \frac{f_i}{1 + \frac{S_{dev}(g_i - g_{bio})}{g_{bio}}} + \frac{4\pi\omega}{3} T_{dev} \right\}^{-1}. \quad (3.87)$$

3.4.1 Piecewise uniform microelastic properties equivalent to the stiffness distributions of both populations of hydrates

Equivalent bulk and shear moduli of the two populations of hydrates are identified such that the piecewise uniform microelastic model delivers the same homogenized stiffness and the same (population-averaged) strain and stress concentration tensor components as the lognormal model.

Equivalent bulk moduli k_3 and k_4 are derived as follows. Equating $A_{vol,j}$ according to Eq. (3.84) and $\overline{A_{vol,j}}$ according to Eq. (3.64) yields the conditions

$$\frac{1}{1 + \frac{S_{vol}(k_j - k_{bio})}{k_{bio}}} = \int_0^{\infty} \frac{\varphi_j(M)}{1 + \frac{S_{vol}(k_j(M) - k_{bio})}{k_{bio}}} dM, \quad j = 3, 4. \quad (3.88)$$

Equating $B_{vol,j}$ according to Eq. (3.86) and $\overline{B_{vol,j}}$ according to Eq. (3.68) yields the conditions

$$\frac{k_j}{1 + \frac{S_{vol}(k_j - k_{bio})}{k_{bio}}} = \int_0^{\infty} \frac{\varphi_j(M) k_j(M)}{1 + \frac{S_{vol}(k_j(M) - k_{bio})}{k_{bio}}} dM, \quad j = 3, 4. \quad (3.89)$$

Notably, the conditions (3.88) and (3.89) also imply the equality of k_{bio} according to Eqs. (3.41) and (3.82). The equivalent bulk moduli k_3 and k_4 are obtained from dividing Eq. (3.89) by Eq. (3.88) as

$$k_j = \frac{\int_0^{\infty} \frac{\varphi_j(M) k_j(M)}{1 + \frac{S_{vol}(k_j(M) - k_{bio})}{k_{bio}}} dM}{\int_0^{\infty} \frac{\varphi_j(M)}{1 + \frac{S_{vol}(k_j(M) - k_{bio})}{k_{bio}}} dM}, \quad j = 3, 4. \quad (3.90)$$

Evaluating Eq. (3.90) for $j = 3$ and for $j = 4$, respectively, yields under consideration of Eqs. (3.B.1)–(3.B.4):

$$k_3 = 35.41 \text{ GPa}, \quad (3.91)$$

$$k_4 = 24.51 \text{ GPa}. \quad (3.92)$$

Equivalent shear moduli g_3 and g_4 are derived in an analogous way. Equating $A_{dev,j}$ according to Eq. (3.85) and $\overline{A_{dev,j}}$ according to Eq. (3.65) yields the conditions

$$\frac{1}{1 + \frac{S_{dev}(g_j - g_{bio})}{g_{bio}}} = \int_0^{\infty} \frac{\varphi_j(M)}{1 + \frac{S_{dev}(g_j(M) - g_{bio})}{g_{bio}}} dM, \quad j = 3, 4. \quad (3.93)$$

Equating $B_{dev,j}$ according to Eq. (3.87) and $\overline{B_{dev,j}}$ according to Eq. (3.69) yields the conditions

$$\frac{g_j}{1 + \frac{S_{dev}(g_j - g_{bio})}{g_{bio}}} = \int_0^{\infty} \frac{\varphi_j(M) g_j(M)}{1 + \frac{S_{dev}(g_j(M) - g_{bio})}{g_{bio}}} dM, \quad j = 3, 4. \quad (3.94)$$

Notably, the conditions (3.93) and (3.94) also imply the equality of g_{bio} according to Eqs. (3.42) and (3.83). The equivalent shear moduli g_3 and g_4 are obtained from dividing Eqs. (3.94) by Eq. (3.93) as

$$g_j = \frac{\int_0^{\infty} \frac{\varphi_j(M) g_j(M)}{1 + \frac{S_{dev}(g_j(M) - g_{bio})}{g_{bio}}} dM}{\int_0^{\infty} \frac{\varphi_j(M)}{1 + \frac{S_{dev}(g_j(M) - g_{bio})}{g_{bio}}} dM}, \quad j = 3, 4. \quad (3.95)$$

Evaluating Eq. (3.95) for $j = 3$ and for $j = 4$, respectively, yields under consideration of Eqs. (3.B.5)–(3.B.8):

$$g_3 = 26.41 \text{ GPa}, \quad (3.96)$$

$$g_4 = 18.59 \text{ GPa}. \quad (3.97)$$

Equivalent stiffness properties, according to Eqs. (3.91), (3.92), (3.96), and (3.97) reproduce the homogenized stiffness as well as the (population-averaged) stress and strain concentration tensor components of the lognormal model, see Tables 3.4 and 3.5. According to Eqs (3.90) and (3.95), the equivalent moduli are functions of (i) the stiffness distributions to which they are equivalent *and* (ii) the interaction of the phase population with all other constituents of the microheterogeneous material.

3.4.2 Comparison of the equivalent piecewise uniform microelastic properties with their probability density functions

The equivalent piecewise uniform microelastic properties, see Eqs. (3.91), (3.92), (3.96), and (3.97), are compared with the probability density functions of the bulk and shear moduli of the two populations of hydrates. These functions are determined as follows: bulk and shear moduli are obtained as a function of the indentation modulus from inserting Eqs. (3.56) and (3.61) into Eqs. (3.57) and (3.58), respectively. Combining the obtained expressions with Eq. (3.19) allows for producing parameter plots showing probability densities over bulk and shear moduli, with the indentation modulus as the parameter. Normalizing the parameter plots, such that the area under the graphs becomes equal to 1, delivers probability density functions for the bulk and shear moduli, see Fig. 3.11. The modes (= most frequent values) and the medians (= 50%-quantiles) of bulk and shear moduli of the two populations of hydrates are determined numerically:

$$\text{mode}(k_3) = 34.14 \text{ GPa}, \quad \text{mode}(g_3) = 25.42 \text{ GPa}, \quad (3.98)$$

$$\text{mode}(k_4) = 13.46 \text{ GPa}, \quad \text{mode}(g_4) = 10.02 \text{ GPa}, \quad (3.99)$$

$$\text{median}(k_3) = 35.61 \text{ GPa}, \quad \text{median}(g_3) = 26.52 \text{ GPa}, \quad (3.100)$$

$$\text{median}(k_4) = 25.19 \text{ GPa}, \quad \text{median}(g_4) = 18.76 \text{ GPa}. \quad (3.101)$$

The modes according to Eqs. (3.98) and (3.99) are marked in Fig. 3.11 by dotted ordinate-parallel lines, the medians according to Eqs. (3.100) and (3.101) by solid lines, and the equivalent piecewise uniform microelastic values according to Eqs. (3.91), (3.92), (3.96), and (3.97) by dash-dotted lines.

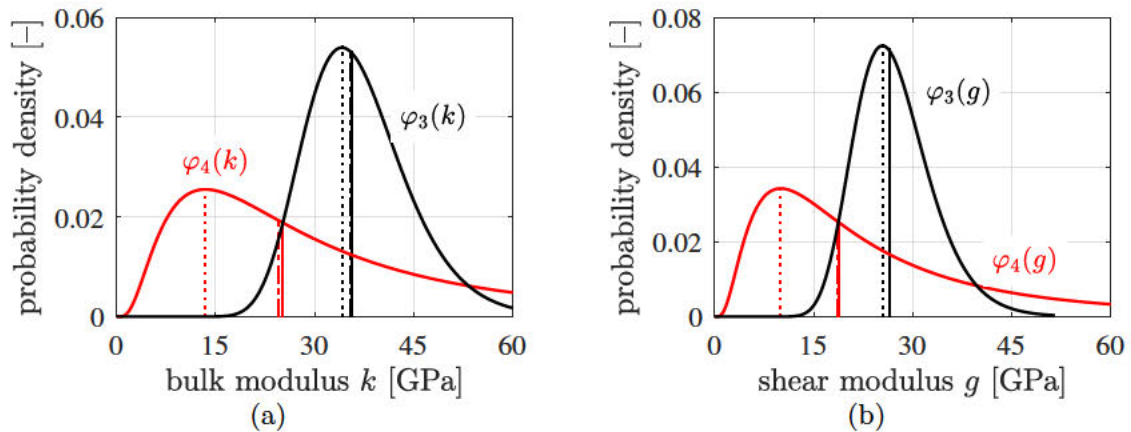


Fig. 3.11. Probability density functions of (a) the bulk and (b) the shear moduli of the LDCR hydrates (red solid graphs) and of the HDCR hydrates (black solid graphs), as well as characteristic stiffness properties: equivalent stiffnesses (dash-dotted lines), mode values (dotted lines), and median values (solid lines).

The equivalent piecewise uniform microelastic values are very close to the median values. This provides the motivation to use the median values as input for the piecewise uniform microelastic model.

3.4.3 Piecewise uniform microelastic model based on median values of bulk and shear moduli of both populations of hydrates

The median values of Eqs. (3.100) and (3.101) are assigned to the LDCR and to the HDCR hydrates. The elastic properties of zirconia and clinker as well as the volume fractions of all constituents are taken from Table 3.2, the crack density parameter from Eq. (3.60). Corresponding homogenized stiffness properties of Biodentine are obtained for the stiffness moduli from Eqs. (3.82) and (3.83):

$$k_{bio} = 38.72 \text{ GPa}, \quad g_{bio} = 14.17 \text{ GPa}. \quad (3.102)$$

These median-based values are by only 0.8% and 0.5% smaller than the corresponding values of the lognormal microelasticity model: $k_{bio} = 38.4 \text{ GPa}$, and $g_{bio} = 14.1 \text{ GPa}$, respectively. The (population-averaged) strain and stress concentration tensor components of the piecewise uniform median-based microelasticity model, computed according to Eqs. (3.84)–(3.87), are listed in Tables 3.8 and 3.9. They differ from the reference values of the lognormal microelasticity model, see Tables 3.4 and 3.5, by only up to 1.05%.

3.5 Discussion

Herein, the solid constituents of Biodentine were modeled as spherical phases, such as introduced in the first micromechanics models for cementitious materials (Bernard et al., 2003; Constantinides and Ulm, 2004). Stora et al. (2006) scrutinized this approach and found that spherical shapes are suitable for hardened cement pastes, but questionable for leached pastes with porosities of up to 40%. Sanahuja et al. (2007) identified specific aspect ratios of oblate nanoscopic solid C-S-H building blocks, in order to model setting (= transition from a gel-like suspension to a solid material). Pichler et al. (2009) compared spherical and

Table 3.8

Results of the median-based piecewise uniform microelasticity model: strain concentration tensors components of the four types of solid constituents of Biodentine according to Eqs. (3.84) and (3.85). The differences of the $A_{vol,i}$, and $A_{dev,i}$ values to the lognormal model are given in brackets.

constituent of Biodentine	strain concentration tensor components and deviations from lognormal microelasticity model			
zirconia	$A_{vol,1} = 0.3036$	(-0.63%)	$A_{dev,1} = 0.2362$	(-0.43%)
clinker	$A_{vol,2} = 0.4250$	(-0.64%)	$A_{dev,2} = 0.3204$	(-0.38%)
HDCR hydrates	$A_{vol,3} = 1.0570$	(-0.18%)	$A_{dev,3} = 0.5250$	(-0.04%)
LDCR hydrates	$A_{vol,4} = 1.3068$	$(+1.05\%)$	$A_{dev,4} = 0.6414$	$(+0.22\%)$

Table 3.9

Results of the median-based piecewise uniform microelasticity model: stress concentration tensors components of the four types of solid constituents of Biodentine according to Eqs. (3.86) and (3.87). The differences of the $B_{vol,i}$, and $B_{dev,i}$ values to the lognormal model are given in brackets.

constituent of Biodentine	stress concentration tensor components and deviations from lognormal microelasticity model			
zirconia	$B_{vol,1} = 1.3397$	$(+0.16\%)$	$B_{dev,1} = 1.3397$	$(+0.06\%)$
clinker	$B_{vol,2} = 1.2805$	$(+0.18\%)$	$B_{dev,2} = 1.2805$	$(+0.08\%)$
HDCR hydrates	$B_{vol,3} = 0.9722$	$(+0.08\%)$	$B_{dev,3} = 0.9722$	$(+0.01\%)$
LDCR hydrates	$B_{vol,4} = 0.8503$	(-0.87%)	$B_{dev,4} = 0.8503$	(-0.20%)

prolate shapes assigned to micron-sized gel-porous hydrates and found significant differences at early ages, when the porosity is quite large, but small differences at mature ages, when the microstructure is already rather dense. Because the present paper refers to *well-hardened* Biodentine, spherical phase shapes are suitable for micromechanical modeling.

The identified value of Poisson's ratio of the calcite-reinforced hydrates of Biodentine ($\nu_h = 0.20$) is smaller than 0.24 which is the value standardly assumed for low-density and high-density C-S-H of construction cement pastes (Constantinides, 2002). The difference can be explained based on different microstructures. Low-density and high-density C-S-H consist of solid C-S-H building blocks and pores (Constantinides et al., 2003). Calcite-reinforced hydrates of Biodentine, in turn, consist of solid C-S-H building blocks, pores, calcium hydroxide, and calcite. Thus, they are somewhat reminiscent of a composite initially referred to as "ultra-high-density C-S-H" (Vandamme and Ulm, 2009), which turned out to be a high-density C-S-H reinforced by small crystals of calcium hydroxide (Chen et al., 2010), see also Da Silva et al. (2014); Brown et al. (2018); Ford et al. (2020).

The present paper continues the line of studies in which results from nanoindentation were combined with micromechanical homogenization approaches. Sorelli et al. (2008) applied the method of Constantinides and Ulm (2004) to an ultra high performance concrete, Němeček et al. (2013) to cement paste, gypsum, and an aluminum alloy, and Göbel et al. (2018) to polymer-modified cement paste. Other complementary research approaches combined grid nanoindentation and stiffness homogenization at different scales of observation and with different targets, as will be discussed next. As for the smallest scales, scanning electron microscopy, energy dispersive spectroscopy, and X-ray diffraction were combined to gain access to the composition at nanoindented material points, and this knowledge was upscaled by means of homogenization methods in order to predict the stiffness at the indented material points, see e.g. Li et al. (2017); Brown et al. (2018). At the next larger scale, microstructural properties of cement paste determined by means of grid nanoindentation were used as input for stiffness upscaling, in order to predict stiffness properties determined by means of microindentation, see e.g. Gao et al. (2017). As for stiffness homogenization up to the material scale of concrete, grid nanoindentation, used for quantifying microstructural properties of cement paste, was combined with microindentation, used for the characterization of interfacial transition zones surrounding aggregates, see e.g. Li et al. (2021).

The present study shares two aspects of emerging developments regarding stiffness upscaling based on results obtained from grid nanoindentation. The first one relates to using probability density functions describing stiffness distributions of two populations of hydrate phases as input for micromechanical modeling, as realized by Stefaniuk et al. (2019) for symmetric, Gaussian stiffness distributions. In this context, our current approach goes three steps further, (i) employing lognormal rather than Gaussian distributions, (ii) evaluating corresponding concentration relations revealing the microstresses to follow generalized beta distributions, and (iii) identifying that median values of the skewed stiffness distributions are representative piecewise uniform stiffness properties governing the overall stiffness of Biodentine. The second aspect relates to weak interfaces. Liang et al. (2017) and Damien et al. (2019) have used a modified Eshelby tensor in the context of cementitious matrix-inclusion composites homogenized by means of the Mori-Tanaka scheme (Benveniste, 1987), in order to account for weak *tangential* bond in interfaces between spherical phases and the surrounding matrix. Herein, we have modeled weak grain boundaries by means of closed circular microcracks which are isotropically oriented in space, in the context of homogenizing the "polycrystalline" microstructure of Biodentine by means of the self-consistent scheme (Zaoui, 2002). This approach allowed us to show that almost 50% of the compliance of hardened Biodentine refers

to shear-dislocations of weak grain boundaries.

3.6 Conclusions

A lognormal microelasticity model for hardened Biodentine was based on the results of a grid nanoindentation campaign. Poisson's ratio of the two populations of hydrates and the crack density parameter were identified such that the model reproduces macroscopic stiffness properties derived from ultrasonic pulse velocity measurements. Based on the results of the presented study, the following conclusions are drawn:

- The identified value of Poisson's ratio of the lower-density and high-density calcite-reinforced hydrates of Biodentine, $\nu_h = 0.20$, is smaller than Poisson's ratio used for the low-density and high-density calcium-silicate-hydrates of Portland cements: $\nu = 0.24$, see Constantinides and Ulm (2004). The difference is attributed to a reinforcement effect of calcite and calcium hydroxide.
- Grain boundary defects (modeled as microcracks) are responsible for almost 50% of the deviatoric compliance of Biodentine. In other words, virtually half of the deformations of Biodentine subjected to macroscopic shear loading originate from microstructural defects. The corresponding value of the crack density parameter was identified as $\omega = 0.78$.
- *Bottom-up* stiffness homogenization, accounting for microscopic stiffness *distributions* of the hydrates, is virtually equivalent to upscaling of piecewise uniform stiffness properties, provided that *medians* of the microscopic stiffness distributions are assigned to the hydrates. Corresponding differences regarding the homogenized stiffness of Biodentine were found to be smaller than 1.1%. This corroborates the validity of standard homogenization models for the elastic stiffness of cementitious materials, because these models are based on piecewise uniform stiffness properties.
- As for *top-down* strain and stress quantification, there are important differences between the lognormal microelasticity model and the alternative which is based on piecewise uniform microscopic stiffness values. The latter approach leads to volume-averaged values of the stresses experienced by the two populations of hydrates. The statistical homogenization approach, in turn, provides direct access to microscopic stress fluctuations. These fluctuations are expected to be valuable for future strength modeling going beyond the scope of the present paper.

Acknowledgments

This project has received funding from the European Union's Horizon 2020 research and innovation programme under the Marie Skłodowska-Curie Grant Agreement No. 764691. The authors gratefully acknowledge the support of Olaf Lahayne from the Institute for Mechanics of Materials and Structures, TU Wien, concerning the ultrasound experiments.

Appendix 3.A Macrostiffness characterization by means of ultrasonic pulse velocity measurements

The ultrasonic pulse transmission method was used as non-destructive technique to characterize the macroscopic elastic properties of hardened Biodentine. Here, both longitudinal and shear

waves, with excitation frequencies ranging from 50 kHz to 20 MHz, were sent through cylindrical Biodentine samples with 5 mm diameter and 10 mm height.

The test setup consisted of a serial arrangement of a pulse generator, a layer of coupling medium (honey), a plastic foil, the specimen, another plastic foil, another layer of honey, and a pulse detector. The plastic foils protected the sample against contamination of its open porosity with the coupling medium. The specimens, the equipment, and its surrounding environment were conditioned to 37°C.

The wave velocities v of Biodentine are equal to the height b of the tested specimens divided by the time of flight t_f of the ultrasonic pulse through the tested specimen,

$$v = \frac{b}{t_f}. \quad (3.A.1)$$

Direct measurement of t_f is not possible; however, it results from the difference of two other time measurements,

$$t_f = t_{tot} - t_d, \quad (3.A.2)$$

where t_{tot} is the travel time of the pulse from the transducer – through the coupling medium, the plastic foils, *and* the specimen – to the receiver, while the delay time t_d is needed by the pulse to just travel from the generator, through honey and plastic foils (without specimen), to the receiver.

325 measurements of longitudinal waves were performed at material ages from 7 to 28 days (Dohnalík et al., 2021). The central excitation frequencies amounted to 50 kHz, 500 kHz, 1 MHz, 2.25 MHz, 5 MHz, 10 MHz, and 20 MHz. The longitudinal wave velocities were fairly independent of the material age as well as the testing frequency. On average, they amount to $\bar{v}_L = 4.977$ km/s, see (Dohnalík et al., 2021) and Fig. 3.A.12.

122 measurements of shear waves were performed at material ages from 7 to 28 days. The central excitation frequencies amounted to 2.25 MHz and 5 MHz, see Table 3.A.10. The shear

Table 3.A.10

Ultrasonic shear wave transducers used for characterization of hardened Biodentine.

frequency [MHz]	shear transducer
2.25	V154-RM
5	V155-RM

wave velocities are also fairly independent of the material age and the testing frequency. On average, they amount to $\bar{v}_S = 2.473$ km/s, see Fig. 3.A.12.

The separation of scales principle states that the wavelengths λ must be significantly larger than the size ℓ_{rve} of a representative volume element of the tested material (Zaoui, 2002; Kohlhauser and Hellmich, 2013), and that ℓ_{rve} must be significantly larger than the characteristic size ℓ_{het} of the microheterogeneities:

$$\lambda \gg \ell_{rve} \gg \ell_{het}. \quad (3.A.3)$$

Residual clinker grains are the largest microheterogeneities of hardened Biodentine. Their characteristic size amounts to 4.3 μm (Dohnalík et al., 2021). Thus, $\ell_{het} = 4.3$ μm . The characteristic size of a representative volume of Biodentine is some three times larger (Drugan and Willis, 1996; Pensée and He, 2007). Thus, $\ell_{rve} = 12.9$ μm . This size is to be compared with the wavelengths of the ultrasonic pulses.

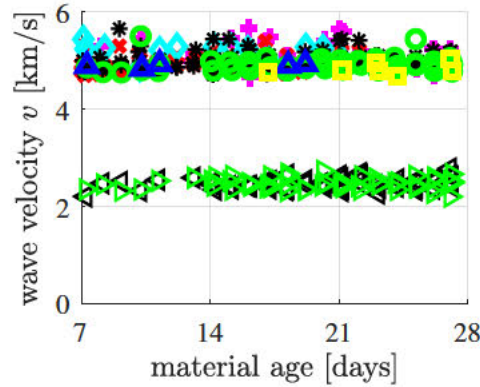


Fig. 3.A.12. Longitudinal and shear wave velocities sent at different frequencies through cylindrical samples of Biodentine, with 5 mm diameter and 10 mm height; the mean longitudinal wave velocity is equal to $\bar{v}_L = 4.977$ km/s (upper data points cluster) and the mean shear wave velocity amounts to $\bar{v}_S = 2.473$ km/s (lower data points cluster). The pink markers correspond to 50 kHz transducers central frequency, red to 500 kHz, cyan to 1 MHz, black to 2.25 MHz, green to 5 MHz, blue to 10 MHz, and yellow to 20 MHz transducers' central frequency, after (Dohnalík et al., 2021).

The wavelength is indirectly proportional to the ultrasonic frequency. Therefore, the largest testing frequency yields a lower bound for the wavelengths. As for the longitudinal waves, this lower bound follows as

$$\lambda_L \geq \frac{\bar{v}_L}{\max f} = \frac{4.977 \text{ km/s}}{20 \text{ MHz}} = 249 \mu\text{m} . \quad (3.A.4)$$

As for the shear waves, it follows as

$$\lambda_S \geq \frac{\bar{v}_S}{\max f} = \frac{2.473 \text{ km/s}}{5 \text{ MHz}} = 495 \mu\text{m} . \quad (3.A.5)$$

Eqs. (3.A.4) and (3.A.5) underline that the wavelengths were by a factor of 19 (longitudinal waves) and 38 (shear waves) larger than $\ell_{rve} = 12.9 \mu\text{m}$. The principle of separation of scales, see Eq. (3.A.3), is fulfilled (Zaoui, 2002; Kohlhauser and Hellmich, 2013). This provides evidence that wave velocities of Fig. 3.A.12 are representative for the homogenized composite Biodentine.

According to the theory of wave propagation through isotropic linear-elastic media, longitudinal and shear wave velocities, together with the mass density ρ of the tested material, allow for quantifying the bulk modulus, k , and the shear modulus, g , as (Kohlhauser and Hellmich, 2012; Carcione, 2007; Achenbach, 1973),

$$k^{exp} = \frac{\rho}{3} (3 v_L^2 - 4 v_S^2) , \quad (3.A.6)$$

$$g^{exp} = \rho v_S^2 , \quad (3.A.7)$$

respectively. Evaluation of Eqs. (3.A.6) and (3.A.7) based on $\rho = 2.311 \text{ kg/dm}^3$ (Dohnalík et al., 2021) and the wave velocities of Fig. 3.A.12 gives access to constant isotropic elastic properties, namely to a bulk modulus of 38.4 GPa and a shear modulus of 14.1 GPa.

Appendix 3.B Numerical values of integrals involving the lognormal distributions of the two populations of hydrates

Numerical evaluation of the integrals in Eqs. (3.41), (3.42), (3.44)–(3.47), and (3.51)–(3.54), based on $k_{bio} = 38.4$ GPa, $g_{bio} = 14.1$ GPa, and $\nu_h = 0.2017$, delivers the following numerical results:

$$\int_0^{\infty} \frac{\varphi_3(M) k_3(M)}{1 + \frac{S_{vol}(k_3(M) - k_{bio})}{k_{bio}}} dM = 37.36450836 \text{ GPa}, \quad (3.B.1)$$

$$\int_0^{\infty} \frac{\varphi_4(M) k_4(M)}{1 + \frac{S_{vol}(k_4(M) - k_{bio})}{k_{bio}}} dM = 32.37198195 \text{ GPa}, \quad (3.B.2)$$

$$\int_0^{\infty} \frac{\varphi_3(M)}{1 + \frac{S_{vol}(k_3(M) - k_{bio})}{k_{bio}}} dM = 1.05507934, \quad (3.B.3)$$

$$\int_0^{\infty} \frac{\varphi_4(M)}{1 + \frac{S_{vol}(k_4(M) - k_{bio})}{k_{bio}}} dM = 1.32063926, \quad (3.B.4)$$

$$\int_0^{\infty} \frac{\varphi_3(M) g_3(M)}{1 + \frac{S_{dev}(g_3(M) - g_{bio})}{g_{bio}}} dM = 18.77600304 \text{ GPa}, \quad (3.B.5)$$

$$\int_0^{\infty} \frac{\varphi_4(M) g_4(M)}{1 + \frac{S_{dev}(g_4(M) - g_{bio})}{g_{bio}}} dM = 16.19052283 \text{ GPa}, \quad (3.B.6)$$

$$\int_0^{\infty} \frac{\varphi_3(M)}{1 + \frac{S_{dev}(g_3(M) - g_{bio})}{g_{bio}}} dM = 0.71090769, \quad (3.B.7)$$

$$\int_0^{\infty} \frac{\varphi_4(M)}{1 + \frac{S_{dev}(g_4(M) - g_{bio})}{g_{bio}}} dM = 0.87075413. \quad (3.B.8)$$

Appendix 3.C Components of the Eshelby tensor of thin oblate spheroids

Consider a thin oblate spheroid with the unit normal to the “crack” plane parallel to \mathbf{e}_3 . The non-vanishing components of the Eshelby tensor \mathbb{S}_{obl} read as (Pichler et al., 2007)

$$\begin{aligned}
 S_{1111} &= \frac{3}{16} \frac{9k_{bio} + 7g_{bio}}{3k_{bio} + 4g_{bio}} \pi X, & S_{2211} &= S_{1122}, \\
 S_{1122} &= \frac{9}{16} \frac{k_{bio} - g_{bio}}{3k_{bio} + 4g_{bio}} \pi X, & S_{2222} &= S_{1111}, \\
 S_{1133} &= \frac{3}{4} \frac{-g_{bio}}{3k_{bio} + 4g_{bio}} \pi X, & S_{2233} &= S_{1133}, \\
 S_{3311} &= \frac{3}{4} \frac{g_{bio} - 3k_{bio}}{4g_{bio} + 3k_{bio}} \pi X - \frac{2g_{bio} - 3k_{bio}}{4g_{bio} + 3k_{bio}}, & S_{1212} &= \frac{3}{16} \frac{3k_{bio} + 5g_{bio}}{3k_{bio} + 4g_{bio}} \pi X, \\
 S_{3322} &= S_{3311} & S_{2323} &= \frac{1}{2} \left(1 - \frac{3}{4} \frac{3k_{bio} + 2g_{bio}}{3k_{bio} + 4g_{bio}} \pi X \right), \\
 S_{3333} &= 1 - \frac{3g_{bio}}{2(3k_{bio} + 4g_{bio})} \pi X, & S_{3131} &= S_{2323},
 \end{aligned} \tag{3.C.1}$$

with $S_{ijkl} = S_{jikl} = S_{ijlk}$. Notably, $X = c/a$ denotes the aspect ratio.

Chapter 4

Strength of dental cement paste: Early age testing and micromechanical explanation at mature ages

Authored by: Petr Dohnalík, Christian Hellmich, Gilles Richard, Bernhard L.A. Pichler

Publication outlook: At the time of finalizing the thesis, this is to be submitted soon to *Frontiers in Bioengineering and Biotechnology*

Abstract: The compressive strength evolution of Biodentine, a cementitious material used in dentistry, is quantified by crushing cylindrical specimens with length-to-diameter ratios amounting to 1.84 and 1.34, respectively, at nine different material ages ranging from 1 hour to 28 days. Significant pre-peak nonlinearities of axial stress-strain relations are obtained in the first few hours after production. At more mature material ages, the stress-strain relations are virtually linear up to the compressive strength, at which the specimens break into many fragments. The strength evolution of 37 centigrade-cured Biodentine can be well described as the exponential of a function involving the square root of the inverse of the normalized time, as given in the *fib* Model Code 2010. The genuine *uniaxial* compressive strength, associated with a length-to-diameter ratio of two, follows the correction formula of ASTM C39, irrespective of the material age. The macroscopic strength of Biodentine is explained by a micromechanics model accounting for lognormal stiffness and strength distributions of two types of calcite-reinforced hydrates occupying, in total, some 85% of the volume of mature Biodentine. The analysis suggests that microscopic hydrates exhibit shear failure under virtually uniaxial compression. As many as 63% of the overall material volume, all occupied by dense calcite-reinforced hydration products, fail virtually simultaneously. This underlines the highly optimized nature of the studied material.

Contribution: Petr Dohnalík: Investigation, Methodology, Formal analysis, Software, Visualization, Writing – review & editing. Bernhard L.A. Pichler: Supervision, Conceptualization, Funding acquisition, Methodology, Formal analysis, Writing – original draft, Writing – review & editing. Gilles Richard: Conceptualization, Funding acquisition, Resources, Writing – review & editing. Christian Hellmich: Conceptualization, Funding acquisition, Formal analysis,

Supervision, Writing – review & editing.

Keywords: Dental cement paste, Compressive strength, Early-age strength evolution, Continuum micromechanics, Lognormal stiffness distribution, Lognormal strength distribution, Degree of utilization

4.1 Introduction

The present study refers to “Biodentine”, a dental cement paste made from a cementitious powder and a mixing liquid. The powder consists of tricalcium silicate (Ca_3SiO_5) and dicalcium silicate (Ca_2SiO_4), representing the two hydraulic components, as well as of zirconium dioxide (ZrO_2) ensuring radiopacity (= clear visibility on radiographs), and calcium carbonate (CaCO_3) acting as a filler (Li et al., 2019) and as a microstructural reinforcement (Dohnalík et al., 2021). The mixing liquid contains water (H_2O), calcium chloride (CaCl_2) accelerating the transition of freshly-mixed Biodentine from a moldable gel into a solid material, and a hydrosoluble polycarboxylate-based polymer improving workability at small initial liquid-to-solid mass ratios (Laurent et al., 2008; Bronnec et al., 2010; Laurent et al., 2012).

The existing literature documents several compressive strength studies regarding Biodentine exposed to different curing environments:

- Specimens cured in distilled water for one hour, as well as for one, seven, and 28 days, exhibited strengths amounting to 140 ± 1 MPa, 171 ± 1 MPa, 269 ± 1 MPa, and 305 ± 3 MPa, respectively (Butt et al., 2014). Similar values were obtained by Franquin et al. (2010).
- Specimens cured for seven days under acidic conditions with pH values amounting to 4.4, 5.4, 6.4, and 7.4 exhibited strengths amounting to 59 ± 5 MPa, 74 ± 7 MPa, 81 ± 8 MPa, and 95 ± 9 MPa (Elnaghy, 2014).
- Specimens cured for three days under *in vivo* conditions, i.e. in molds contaminated with blood or saliva, exhibited strengths amounting to 177 ± 28 MPa, and 157 ± 57 MPa, respectively (Subramanyam and Vasantharajan, 2017). Corresponding control specimens cured in clean molds were stronger, with strength amounting to 205 ± 22 MPa. Similarly, casting Biodentine into molds filled with blood, and testing at material ages of 6 hours, 1, 3, and 7 days, delivered strength values amounting to 34 ± 9 MPa, 50 ± 13 MPa, 36 ± 15 MPa, 39 ± 12 MPa, respectively (Sheykhrezae et al., 2018).

Cylindrical molds with length = 6 mm and inner diameter = 4 mm (length-to-diameter ratio = 1.5) are typically used to produce specimens for strength testing of Biodentine, because this complies with the requirement of the standard ISO 9917-1:2007 for testing of powder/liquid dental cements intended for permanent cementation, lining, and restoration (International Organization for Standardization, 2007). From cementitious materials used in building construction, however, it is known that the “genuine” uniaxial compressive strength is obtained from cylindrical specimens with a length-to-diameter = 2, see ASTM C39 (American Society for Testing and Materials, 2021). Less slender specimens lead to larger strength values (Amieur, 1994; Keskin et al., 2019; Govindaraju et al., 2017; Atmeh, 2020), because of the lack of homogeneous stress states within the specimens (Fischer et al., 2014; Karte et al., 2015; Ausweger et al., 2019). To the best knowledge of the authors, this aspect has not been systematically studied yet, and provides the first motivation for the present paper, where specimens with height-over-diameter ratios of 1.34 and 1.84, respectively, are tested, in order

to find out whether the correction scheme of ASTM C39 (American Society for Testing and Materials, 2021) is applicable so as to determine the genuine compressive strength associated with the aforementioned ratio amounting to two. In parallel, the development of strength with material age is investigated, and quantified by means of the strength evolution formula of the *fib* Model Code 2010 (International Federation for Structural Concrete, 2010). While stress-strain characteristics are described in Section 4.2, the code-based developments are covered by Section 4.3. Stress-strain characteristics of specimens loaded up to failure are hardly discussed in the open literature. We also tackle this knowledge gap, when, in Section 4.4, a detailed micromechanical explanation for the failure behavior of mature Biodentine is provided, setting the present experimental results to an earlier nanoindentation campaign (Dohnalík et al., 2021) and its micromechanical evaluation (Dohnalík et al., 2022). Section 4.5 closes the paper with conclusions drawn from the presented results.

4.2 Compressive strength testing from early to mature material ages

In the following, compressive forces and stresses as well as the related shortening of the specimens are described with a positive mathematical sign.

4.2.1 Production and storage of cylindrical specimens

Specimens of Biodentine were produced according to the instructions of the manufacturer. Capsules containing the dry binder powder were opened. 173 μL of the mixing liquid were dripped onto the binder using a micropipette (Handy Step, Mettler Toledo, USA). The capsules were closed, shaken in the amalgamator for 30 seconds, and re-opened. The freshly produced cement paste was cast into cylindrical polytetrafluoroethylene molds with two different length-to-diameter ratios. The slenderer molds had a length = 10 mm and a diameter = 5 mm. The less slender molds had a length = 6 mm and a diameter = 4 mm. The corresponding specimens are referred to as “5/10 specimens” and “4/6 specimens”, respectively.

In order to allow the material to transform from a moldable gel into a solid, the molds were covered by glass plates (= microscope slides). The latter were secured by means of a U-shaped clamp and a screw, see Fig. 4.1(a). This assembly was stored inside a container, above a water bath tempered to 37°C, see Fig. 4.1(b). After 20 minutes, the solidified specimens were taken out of their molds.

In order to protect the specimens against drying and calcium leaching, they were inserted into test tubes filled with lime-saturated solution tempered to 37°C. The test tubes were closed and put into a beaker containing distilled water. The beaker was stored in a climate chamber (MOV-112F, Sanyo, Japan), see Fig. 4.1(c). Both the distilled water and the climate chamber were tempered to 37°C, see Fig. 4.1(c). In this configuration, the specimens hardened until they were scheduled for testing.

In order to prepare the specimens for destructive compressive testing, they were taken out of the lime-saturated solution and processed as follows. In order to come up with coplanarity of the two opposite circular surfaces, they were ground by means of a polishing machine (LaboPol-5, Struers, Germany) operated at 300 revolutions per minute, using silicon carbide grinding paper with a grain size of 15 μm (Struers Grit 1200). During grinding, the specimens were kept in a holder which was geometrically identical to the molds described above. In order to rinse the removed material off the revolving polishing paper, a moderate flow of water was poured on it from the built-in outlet. The length L and the diameter D of the

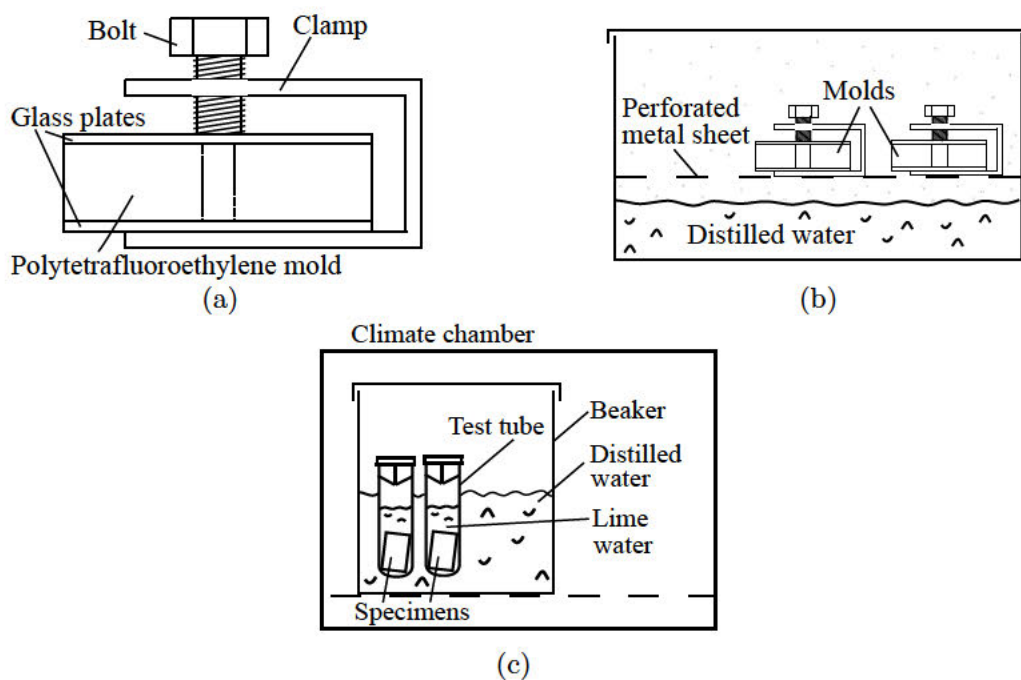


Fig. 4.1. (a), (b) Storage of specimens of Biodentine during their transition from a moldable gel into a solid: (a) specimen inside a polytetrafluoroethylene mold, covered by two glass plates which were secured by means of a U-shaped clamp and a screw, (b) the clamped molds were stored above a water bath tempered to 37°C. (c) Storage of solid specimens until they were scheduled for destructive compressive strength testing: the specimens were stored in lime-saturated solution inside a temperature-controlled environment.

ground specimens were measured using a digital sliding caliper (CD-S15CK, Mitutoyo, Japan). The 5/10 specimens had an average length = 9.22 mm, see Tables 4.1, and 4.2. The 4/6 specimens had an average length = 5.26 mm, see Tables 4.3, and 4.4. Thus, the average length-to-diameter ratios of the two types of specimens amounted to

$$5/10 \text{ specimens: } \Rightarrow L/D = 1.84, \quad (4.1)$$

$$4/6 \text{ specimens: } \Rightarrow L/D = 1.34. \quad (4.2)$$

Two photographs were taken after polishing, one each from opposite sides of the specimens. Finally, the specimens were placed, one after the other, onto the bottom load plate of a universal testing machine (Criterion C43.104Y, MTS Systems Corporation, USA). The crosshead was very slowly moved downwards, under visual control, until the upper load plate was very close to (but not yet in contact with) the specimen.

Table 4.1

Diameters of the 5/10 specimens measured after polishing of the contact surfaces; every listed value is the arithmetic mean of three measurements.

mat. age	diameter D [mm] of a specimen n						
	1	2	3	4	5	6	7
1 hr.	5.01	5.00	5.00	5.00	4.98	4.96	–
1.5 hrs.	5.01	5.00	5.01	5.00	5.02	5.00	4.99
3 hrs.	4.98	5.00	4.99	4.99	4.99	4.99	–
7.5 hrs.	4.99	5.00	5.01	5.02	5.00	4.98	4.98
25.5 hrs.	5.01	4.98	4.99	4.99	5.02	5.00	5.04
7 days	4.99	4.99	4.99	4.98	4.95	5.00	5.01
7 days*	4.98	4.98	5.01	5.00	5.00	4.98	5.02
14 days	4.97	5.01	4.99	4.99	4.99	5.03	4.99
14 days*	5.01	5.00	5.02	5.02	5.00	5.00	5.01
21 days	5.02	5.01	5.00	5.03	5.03	5.00	5.02
28 days	5.01	5.02	5.01	4.99	5.00	5.03	5.02

* the numbering of the specimens continues as $n + 7$.

4.2.2 Destructive compression testing

The destructive compression tests were performed by the testing machine under displacement control, realized through software TW Elite v4.6.0.23, MTS Systems Corporation, USA. In order to prescribe a strain rate of $\approx 1.5 \times 10^{-3}$ /s, the speed of the crosshead was set equal to 0.83 mm/min for the 5/10 specimens, and to 0.50 mm/min for the 4/6 specimens. As output, the software delivered measured histories of the displacement of the crosshead (= estimate of the shortening of the tested specimen), $\Delta L(t)$, and of the force $F(t)$ imposed on the tested specimen.

The evolution of the axial normal strain $\varepsilon(t)$ of a tested specimen follows from dividing

Table 4.2

Lengths of the 5/10 specimens measured after polishing of the contact surfaces; every listed value is the arithmetic mean of three measurements.

mat. age	length L [mm] of a specimen n						
	1	2	3	4	5	6	7
1 hr.	9.37	9.25	9.42	9.20	9.13	8.88	–
1.5 hrs.	9.30	9.33	9.33	9.46	9.37	9.30	9.35
3 hrs.	9.07	9.36	9.44	9.07	9.27	9.14	–
7.5 hrs.	9.47	8.54	9.32	9.25	9.31	8.98	8.74
25.5 hrs.	9.09	9.45	9.02	9.37	8.99	9.20	9.04
7 days	8.96	9.25	9.24	9.50	8.84	9.13	9.29
7 days*	9.21	9.29	9.07	9.28	9.36	9.32	9.26
14 days	8.84	9.32	9.25	9.15	9.11	9.14	9.27
14 days*	9.36	9.47	9.34	9.20	9.48	9.11	9.09
21 days	9.38	9.44	9.33	9.47	9.20	9.11	9.10
28 days	9.15	9.12	9.25	9.19	9.22	9.19	9.36

* the numbering of the specimens continues as $n + 7$.

Table 4.3

Diameters of the 4/6 specimens measured after polishing of the contact surfaces; every listed value is the arithmetic mean of three measurements.

mat. age	diameter d [mm] of a specimen n						
	1	2	3	4	5	6	7
1.5 hrs.	3.89	3.98	3.99	3.98	3.91	3.93	3.91
7.5 hrs.	–‡	3.88	3.86	3.95	3.99	3.94	3.98
25.5 hrs.	3.94	3.96	3.89	3.90	3.94	3.90	3.90
7 days	3.91	3.92	3.98	3.96	3.90	3.94	3.91
14 days	3.91	3.88	3.93	3.89	4.04	4.00	3.93
21 days	3.88	3.95	3.96	3.99	3.91	–‡	4.01
28 days	3.89	3.96	3.97	3.91	3.93	3.89	3.99

‡ specimens failed during handling, prior to testing

Table 4.4

Lengths of the 4/6 specimens measured after polishing of the contact surfaces; every listed value is the arithmetic mean of three measurements.

mat. age	length L [mm] of a specimen n						
	1	2	3	4	5	6	7
1.5 hrs.	5.04	4.97	5.32	5.48	5.43	5.41	4.99
7.5 hrs.	–‡	5.17	5.69	5.31	5.38	5.22	5.43
25.5 hrs.	5.63	5.27	5.46	5.45	5.41	5.44	5.68
7 days	5.27	5.51	5.34	5.45	5.25	5.51	5.13
14 days	5.47	4.30	5.09	5.18	5.36	5.01	4.73
21 days	5.25	5.12	5.24	4.60	5.26	–‡	5.49
28 days	5.17	5.21	5.49	5.17	5.10	5.14	5.17

‡ specimens failed during handling, prior to testing

$\Delta L(t)$ by the initial length of the specimens, L :

$$\varepsilon(t) = \frac{\Delta L(t)}{L}. \quad (4.3)$$

The evolution of the axial normal stress $\sigma(t)$ of a tested specimen follows from dividing $F(t)$ by the cross-sectional area $= d^2\pi/4$ of the specimen:

$$\sigma(t) = \frac{4F(t)}{d^2\pi}. \quad (4.4)$$

A total of 122 destructive compression tests were performed at material ages ranging from 1 hour to 28 days, see Tables 4.5 and 4.6. The material age is counted from the time instant when the mixing liquid got in contact with the dry binder powder.

4.2.3 Discarding tests influenced by imperfections

Miniaturized compressive strength tests on cylindrical specimens are a challenging task, because such experiments are prone to suffer from imperfections which reduce the ultimate loads sustained by the specimens. This provides the motivation to discard tests which were evidently affected either by geometric imperfections regarding coplanarity or by pores entrapped during casting, as described in the following two paragraphs.

Geometric imperfections, such as residual roughness or tilt, may lead to partial, rather than full-face, contact between the specimen and the load application system; in particular so during the initial phase of a compression test. This manifests itself in a positive curvature of stress-strain graphs at stress levels which are small to the finally reached strength, see Fig. 4.2(a). Given that geometric imperfections were “small”, progressive increase of compressive loading resulted in the transition to full-face contact and to a virtually linear stress-strain graph. In addition, stress fluctuations (rather than a uniform stress field) occurred inside several of the tested specimens, manifesting themselves by audible cracking events and/or visible spalling, however, in any case by a sudden drop of the sustained force, followed by its re-increase, sometimes even surpassing the level at which the local damage event took place, see Fig. 4.2(a). The ultimate force sustained by a specimen which suffered from a pre-peak cracking event

Table 4.5

Values of the ultimate compressive forces sustained by the 5/10 specimens, tested at specific material ages.

material age	ultimate force F_{ult} [N] of the specimen n						
	1	2	3	4	5	6	7
1 hour	1060	990	942	1095	810†	849	–
1.5 hours	1940	1369	1853	1896	1630	1998	1826
3.0 hours	3081	2979	2422*	2673†	2821	2790†	–
7.5 hours	3042	2951*	3201	2760*	2835*	3259	3262†
25.5 hours	3006†	2792*	3498*	3951	4154	3899	3807†
7 days	4616	5358	4024*	4504*	4805*	4518	4134*
7 days‡	5036	4815*	3160*	3570*	4082*	4322*	3900*
14 days	4787*	4878*	4446*	3523*	4832*	5371	5387
14 days‡	4967*	4786*	5371*	5150	4127*	4035†	5577*
21 days	5312†	5157	4841	4936	4333*	4208*	4570*
28 days	4637*	6220*	5355*	5082*	4538*	5026*	2815*

* experiment discarded because of pre-peak cracking event(s)

† experiment discarded because of visible microstructural imperfection(s)

‡ the numbering of the specimens continues as $n + 7$

Table 4.6

Values of the compressive ultimate forces sustained by the 4/6 specimens, tested at specific material ages.

material age	ultimate force F_{ult} [N] of the specimen n						
	1	2	3	4	5	6	7
1.5 hours	1466	1396	779*	1386	1402	1130	1504
7.5 hours	–‡	2116*	2307	2734	1550*	1839*	2375
25.5 hours	2290*	1951*	2779	2532	1648*	2696	2630†
7 days	2940*	2701*	2143*	2503*	3267	2898*	2467*
14 days	3178*	3057*	3714	2798*	3427	2960*	3059
21 days	1352*	3555	3590*	1662*	2820*	–‡	3244
28 days	2247*	3268*	2902*	3194	3236*	2288†	1985*

* experiment discarded because of pre-peak cracking event(s)

† experiment discarded because of visible microstructural imperfection(s)

‡ specimens failed during handling, prior to testing

is very likely smaller than the ultimate force the specimen would have reached without the damage event. Therefore, we discard all those tests with stress-strain graphs qualitatively similar to the ones shown in Fig. 4.2(a). Corresponding values of the ultimate forces are marked with a “★”-symbol in Tables 4.5 and 4.6.

Macropores entrapped unintentionally during casting result in stress concentrations that can trigger premature failure of a specimen. Therefore, the fragments of the specimens were checked for visible defects. In case a macropore was found to be intersected by a macrocrack, see e.g. Fig. 4.2(b), the test was discarded. Corresponding values of the ultimate forces are marked with a “†”-symbol in Tables 4.5 and 4.6.

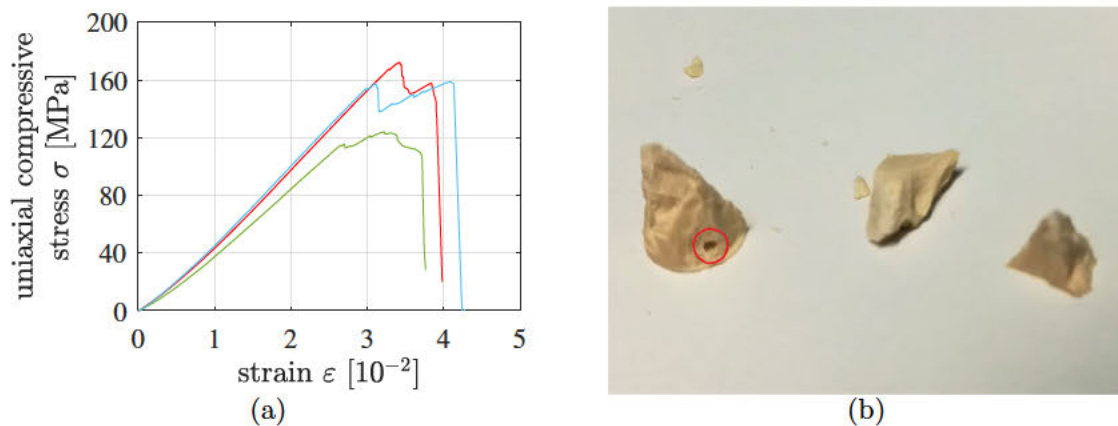


Fig. 4.2. (a) Three examples of stress-strain graphs referring to compression tests suffering from pre-peak cracking events: such tests were discarded. (b) Fragments of 5/10-specimen No. 7, tested 7.5 hours after production, showing a macropore intersected by one of the cracks that had split the specimen: such tests were discarded.

4.2.4 Stress-strain diagrams

31 tests on 5/10 specimens and 19 tests on 4/6 specimens are apparently free of significant imperfections, see Figs. 4.3 and 4.4 for the respective stress-strain diagrams. Some of the graphs exhibit a positive curvature in the first third of the loading interval, see e.g. the blue graph in Fig. 4.3(a). Although this is a sign of geometric imperfections (see above), such tests were nonetheless accepted as long as the stress-strain diagrams increased monotonically all the way up to the strength, without showing pre-peak damage events.

Pre-peak ductility is clearly visible in stress-strain graphs of specimens tested less than 2 hours after production, see the nonlinearities in the last thirds of the loading intervals in Figs. 4.3(a) and (b) as well as in Fig. 4.4(a). This ductility decreases with increasing age of Biodentine. One day after production, the material behavior is virtually linear all the way up to sudden brittle failure, see Figs. 4.3(e)–(h) and 4.4(c)–(g). Notably, pre-peak ductility has the potential to compensate for small imperfections regarding coplanarity. Accordingly, the portion of tests discarded because of pre-peak cracking events decreases with decreasing material age, see Tables 4.5 and 4.6.

4.2.5 Early-age strength evolution

The average strength of the 5/10 specimens tested 1 hour after production amounts to 50.4 MPa, it almost doubles to 90.9 MPa during the following 30 minutes, and it virtually doubles again to

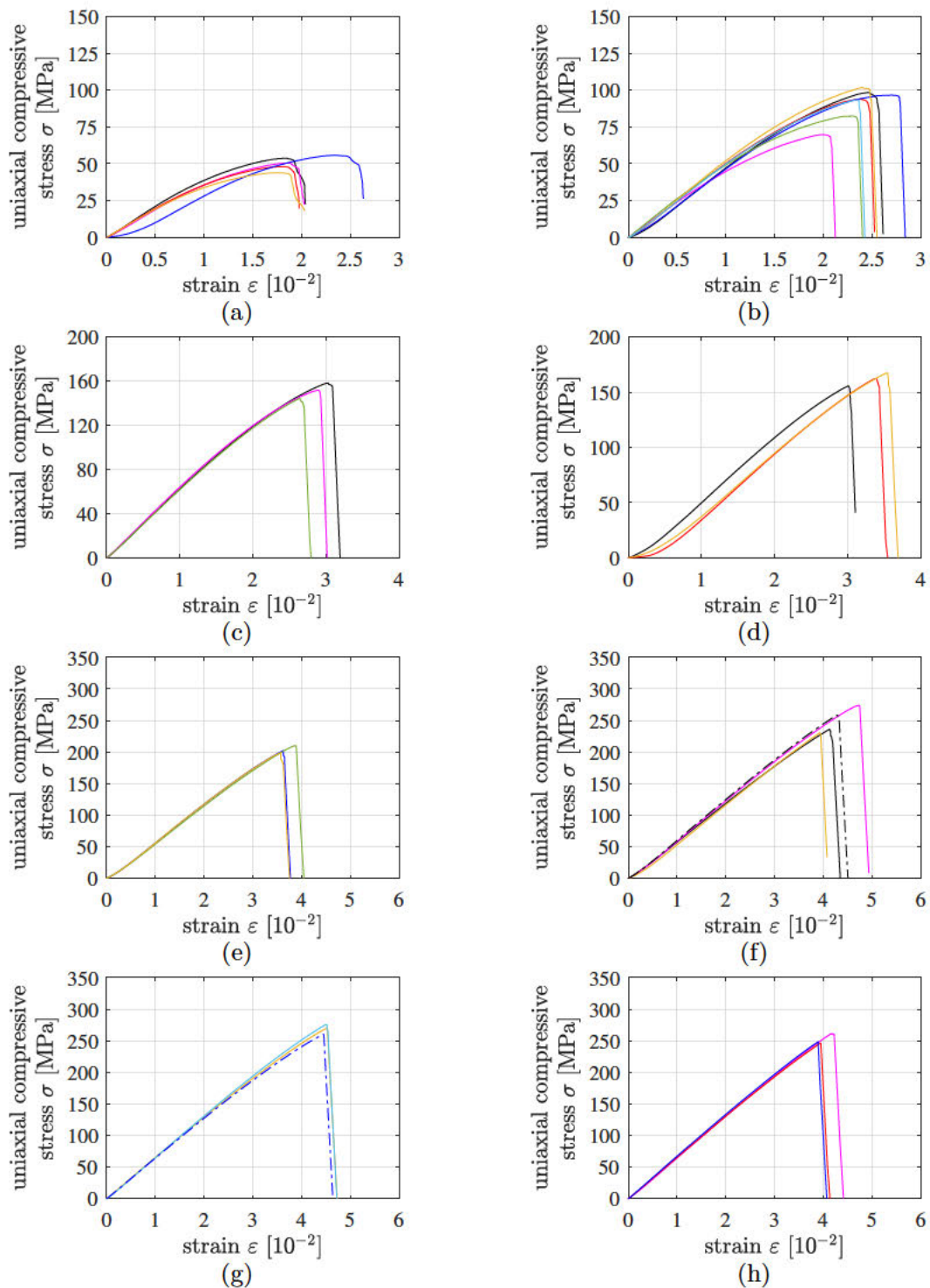


Fig. 4.3. Stress-strain diagrams from destructive compression experiments of 5/10 specimens tested (a) 1 hour, (b) 1.5 hours, (c) 3 hours, (d) 7.5 hours, (e) 25.5 hours, (f) 7 days, (g) 14 days, and (h) 21 days after production; specimen number #1: black solid lines, #2: pink, #3: red, #4: dark blue, #5: green, #6: yellow, #7: light blue, see also Tables 4.7, 4.1, and 4.2; the dash-dotted graphs refer to specimen numbers $n + 7$.

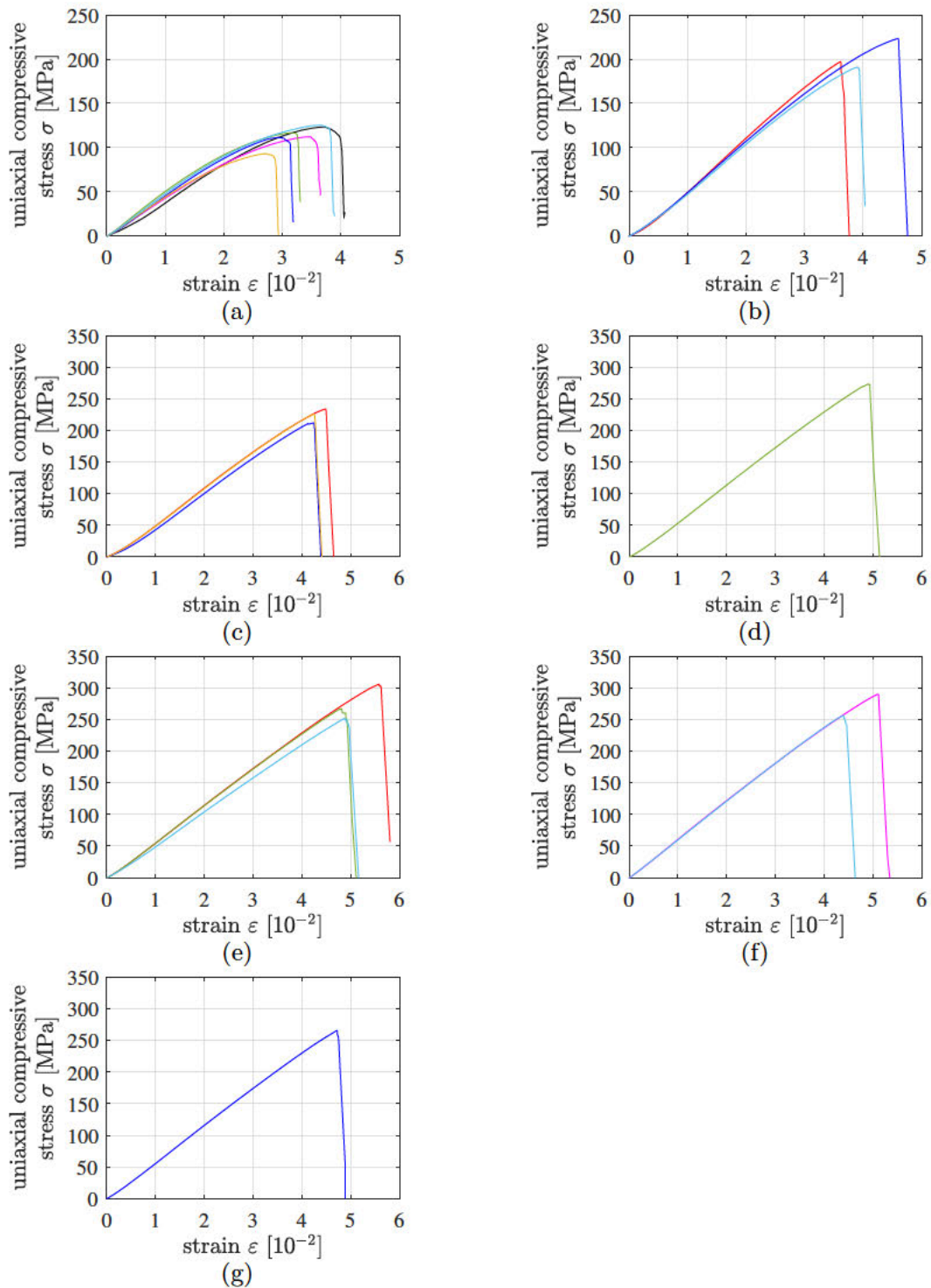


Fig. 4.4. Stress-strain diagrams from destructive compression experiments of 4/6 tested (a) 1.5 hours, (b) 7.5 hours, (c) 25.5 hours, (d) 7 days, (e) 14 days, and (f) 21 days after production; specimens number #1: black solid lines, #2: pink, #3: red, #4: dark blue, #5: green, #6: yellow, #7: light blue, see also Tables 4.8, 4.3, and 4.4.

Table 4.7

Compressive strength values of the 5/10 specimens, from tests which were apparently free of significant imperfections.

material age	comp. strength f_{cu} [MPa] of a specimen n						
	1	2	3	4	5	6	7
1 hour	53.8	50.4	48.0	55.8	–	43.9	–
1.5 hour	98.4	69.7	94.0	96.6	82.4	101.8	93.4
3 hours	158.2	151.7	–	–	144.2	–	–
7.5 hours	155.6	–	162.4	–	–	167.3	–
25.5 hours	–	–	–	202.0	209.9	198.6	–
7 days	236.0	274.0	–	–	–	230.1	–
7 days*	258.6	–	–	–	–	–	–
14 days	–	–	–	–	–	270.3	275.5
14 days*	–	–	–	261.6	–	–	–
21 days	–	261.6	246.5	248.4	–	–	–

* the numbering of the specimens continues as $n + 7$.

203.5 MPa in the subsequent 24 hours, see Table 4.7. Seven days after production, the average strength amounts to 249.7 MPa, 14 days after production to 268.7 MPa, and 21 days after production to 252.2 MPa. This decrease of strength values in the third week after production is unrealistic. It underlines that strength testing is very challenging at such mature material ages. This is corroborated by the test results obtained 28 days after material production, all of which had to be discarded because of pre-peak cracking events. For all other material ages there are at least three tests which were free of significant imperfections, see Table 4.7.

A similar early-age strength evolution is found for the 4/6 specimens. The average strength 1.5 hours after production amounts to 113.7 MPa, 6 hours later it is equal to 203.7 MPa, and 25.5 hours after production to 223.8 MPa, see Table 4.8. Both 7 and 28 days after production,

Table 4.8

Compressive strength values of the 4/6 specimens, from tests which were apparently free of significant imperfections.

material age	comp. strength f_{cu} [MPa] of a specimen n						
	1	2	3	4	5	6	7
1.5 hour	123.3	112.2	–	111.4	116.7	93.1	125.2
7.5 hours	–	–	197.1	223.1	–	–	190.9
25.5 hours	–	–	233.8	212.0	–	225.7	–
7 days	–	–	–	–	273.5	–	–
14 days	–	–	306.1	–	267.4	–	252.2
21 days	–	290.1	–	–	–	–	256.9
28 days	–	–	–	266.0	–	–	–

there is only one test which was apparently free of significant imperfections, 21 days after production there are two such tests, and 14 days after production there are three of them, see Table 4.8. At the latter material age, the average strength amounts to 275.2 MPa.

4.2.6 Failure modes

Both types of specimens exhibited similar failure modes. Axial splitting cracks were observed along the visible lateral surfaces of the specimens, particularly so in the central region of the specimens, i.e. surface cracks were propagating predominantly in loading direction, and only some of them ran across the full height of the specimens, see e.g. Fig. 4.5(a). In several tests, parts of the specimen spalled away during failure from the central region of its lateral surface, leaving behind fragments reminiscent of two cones, whereby the bases of the two cones were located at the interfaces between specimen and the load plates, and the two tips of the cones touched each other at the center of the specimen, see e.g. Fig. 4.5(b). These cones indicate that stresses were fluctuating inside the specimen rather than being uniform throughout the tested volume (Amieur, 1994). These stress fluctuations are known to result from the frictional interaction between the specimen and the load plates (Karte et al., 2015). Notably, the photos of Fig. 4.5 were taken at material ages amounting to 1 hour and to 7.5 hours, respectively. With increasing maturity, the material became more brittle, and the specimens disintegrated into many pieces. At material ages amounting to one day and older, the specimens broke into many fragments, so that classical categorizations concerning the propagation direction of single cracks are not useful anymore. This behavior, observed under *quasi-static* loading rates, is reminiscent of the failure mode usually observed under *high-dynamic* loading rates (Fischer et al., 2014; Binder et al., 2020).

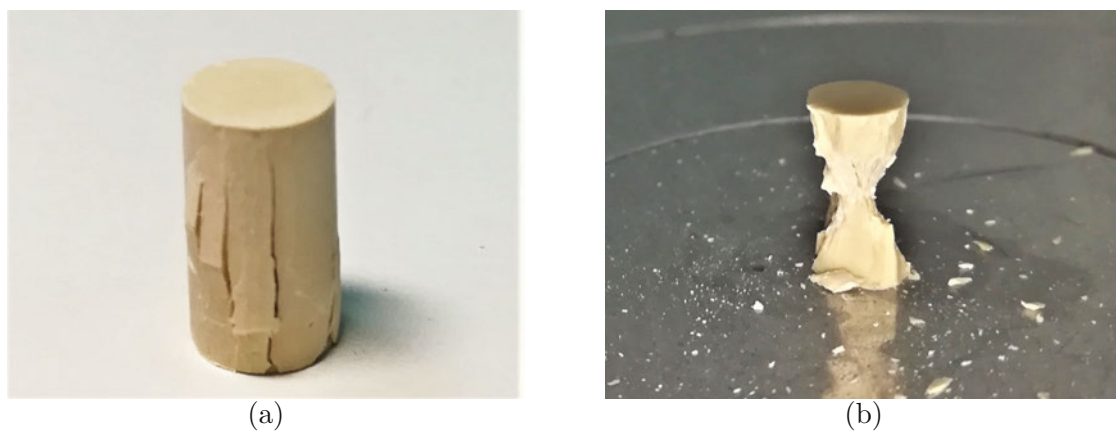


Fig. 4.5. Photos of 5/10 specimens tested at material ages amounting to (a) 1 hour, and (b) 7.5 hours.

4.3 Standards-based evaluation of experimental data

4.3.1 Early-age strength evolution

In order to interpolate between the strength values determined by means of testing, and in order to extrapolate to material ages at which no tests were performed, an empirical function is adopted from the *fib* Model Code 2010 (International Federation for Structural Concrete,

2010). Its original version is designed for the description of the early-age strength evolution of construction concretes curing at 20°C, and it reads as

$$f_c(t) = f_{c,28\text{d}} \times \exp \left[s \left(1 - \sqrt{\frac{28\text{ days}}{t}} \right) \right], \quad (4.5)$$

where f_c denotes the compressive strength, t the material age (in days), $f_{c,28\text{d}}$ the compressive strength reached 28 days after production, and s a dimensionless parameter accounting for the speed of the early-age strength evolution at 20°C. The value of s is the smaller the faster the early-age strength evolution, see e.g. (Ausweger et al., 2019) for a detailed discussion.

The strength of Biodentine curing at 37°C increases significantly up to a material age of 14 days, while it is virtually constant in the third and fourth week after production. This provides the motivation to reformulate Eq. (4.5) as

$$f_c(t) = f_{c,14\text{d}} \times \exp \left[s_{Bio} \left(1 - \sqrt{\frac{14\text{ days}}{t}} \right) \right], \quad (4.6)$$

where $f_{c,14\text{d}}$ denotes the compressive strength reached 14 days after production, and s_{Bio} is a dimensionless parameter accounting for the speed of the early-age strength evolution of Biodentine at 37°C.

The compressive strength reached 14 days after production, $f_{c,14\text{d}}$, is quantified separately for each one of the two types of specimens. Given that the strength was found to be virtually constant throughout the third and fourth week after production, $f_{c,14\text{d}}$ is set equal to the mean value of all strength values obtained 14, 21, and 28 days after production. In both cases, six strength values refer to that interval of material ages, see the last three lines in Tables 4.7 and 4.8. The corresponding mean values read as

$$5/10 \text{ specimens: } \Rightarrow f_{c,14\text{d}} = 260.4 \text{ MPa}, \quad (4.7)$$

$$4/6 \text{ specimens: } \Rightarrow f_{c,14\text{d}} = 273.1 \text{ MPa}, \quad (4.8)$$

see also the last line of Table 4.9 which lists average strength values as a function of specimen type and material age.

The early-age strength evolution of both types of specimens is fitted by means of one value of s_{Bio} :

$$s_{Bio} = 0.06, \quad (4.9)$$

see the solid lines in Fig. 4.6 for the satisfactory performance of Eqs. (4.6)–(4.9) after fitting.

4.3.2 Influence of the length-to-diameter ratio of cylindrical specimens on their compressive strength

The 5/10 specimens delivered smaller compressive strength values than the 4/6 specimens, throughout the interval of material ages covered by destructive compression tests, see Table 4.9. This raises the question how to quantify the *genuine uniaxial* compressive strength of Biodentine. It is recalled that the compressive strength of cylinders made of cementitious construction materials is known to increase with decreasing slenderness-ratio L/D , where L denotes the axial length of the specimen, and D its diameter. The ASTM C39 standard (American Society for Testing and Materials, 2021) provides correction factors which are to be multiplied with experimentally determined compressive strength values, in order to

Table 4.9

Average compressive strength values as a function of specimen type and material age; the underlying individual strength values are listed in Tables 4.7 and 4.8.

material age	5/10 specimens		4/6 specimens	
	mean [MPa]	st. dev. [MPa]	mean [MPa]	st. dev. [MPa]
1 hour	50.4	4.7	–	–
1.5 hour	90.9	11.1	113.7	11.5
3 hours	151.4	7.0	–	–
7.5 hours	161.8	5.9	203.7	17.1
25.5 hours	203.5	5.8	223.8	11.0
7 days	249.7	20.3	273.5	–
14–28 days	260.4	10.5	273.1	19.0

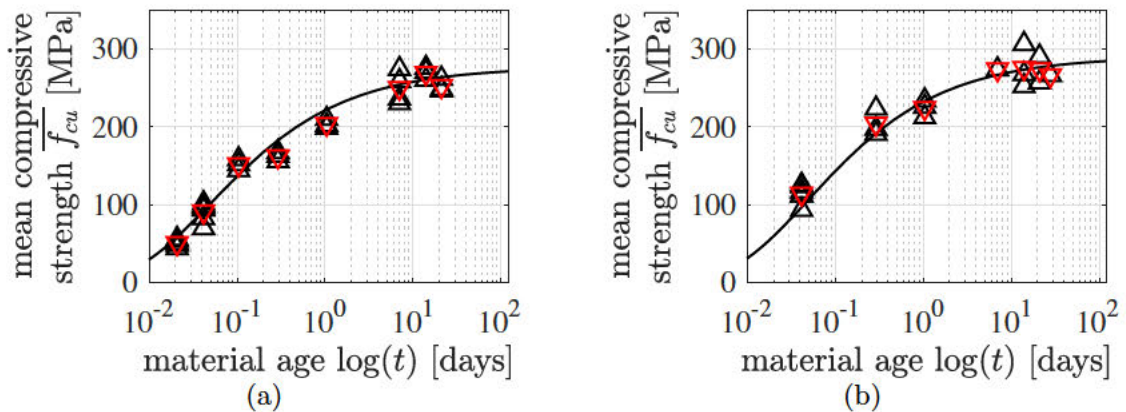


Fig. 4.6. Early-age strength evolution of (a) the 5/10 specimens and (b) the 4/6 specimens: the black \triangle symbols mark individual strength values of Tables 4.7 and 4.8, the red ∇ symbols mark the corresponding mean values of Table 4.9, and the black solid lines were obtained from the combination of Eqs. (4.6)–(4.9).

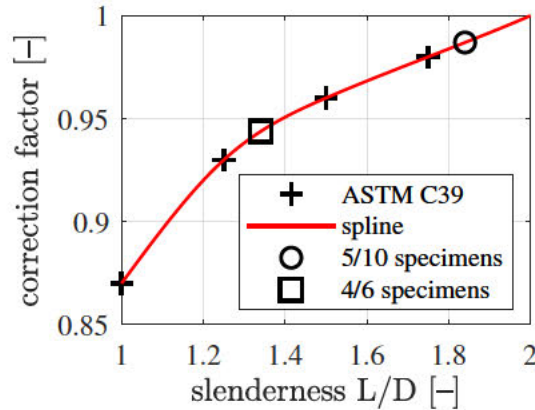


Fig. 4.7. Correction factors compensating the overestimation of the genuine uniaxial compressive strength of cementitious construction materials as a function of the slenderness-ratio: “+” symbols mark values taken from ASTM C39 standard (American Society for Testing and Materials, 2021), the red graph is a spline running through the data points of ASTM C39, the “□” symbol marks the correction factor referring to the slenderness-ratio of the 4/6 specimens, and the “o” symbol marks the correction factor referring to the slenderness-ratio of the 5/10 specimens.

quantify the genuine uniaxial compressive strength. The correction factor is equal to one for a slenderness-ratio of two, and for half this ratio, it decreases by some 13%, see Fig. 4.7.

In order to check whether the correction factors of ASTM C39 also apply to Biodentine, the 14 days-strength-values of Eqs. (4.7) and (4.8) are corrected. The correction factor of the 5/10 specimens (slenderness = 1.84) amounts to 0.9870, and that of the 4/6 specimens (slenderness = 1.34) to 0.9437, see Fig. 4.7. Related estimates of the genuine uniaxial compressive strength of Biodentine, reached 14 days after production, are obtained as

$$\text{5/10 specimens: } \Rightarrow f_{c,14d} \approx 260.4 \text{ MPa} \times 0.9870 = 257.0 \text{ MPa}, \quad (4.10)$$

$$\text{4/6 specimens: } \Rightarrow f_{c,14d} \approx 273.1 \text{ MPa} \times 0.9437 = 257.7 \text{ MPa}. \quad (4.11)$$

The two independent estimates differ by less than 0.3%. This suggests that the correction factors of ASTM C39 are applicable to Biodentine. The genuine uniaxial compressive strength of the material, reached 14 days after production, is set equal to the average value of the two values given in Eqs. (4.10) and (4.11):

$$f_{c,14d} = 257.4 \text{ MPa}. \quad (4.12)$$

The correction factors of Fig. 4.7 apply to strength values obtained at *any* material age of Biodentine, i.e. they are not limited to strength values obtained 14 days after production. This is underlined by Eqs. (4.6)–(4.9) which describe that the strength ratio between the 5/10 and the 4/6 specimens is, at *any* material age, *the same*, see also Figs. 4.6(a) and (b). Conclusively, cylindrical specimens with slenderness ratio smaller than two overestimate the genuine uniaxial compressive strength of Biodentine by a factor which is independent of material age. The latter is a function of the slenderness-ratio of the specimen. This underlines that the correction factors of Fig. 4.7 account for a structural (rather than for a material) effect.

Eq. (4.6) also suggest that the strength evolution does, strictly speaking, not come to an end. This is consistent with images of the microstructure of Biodentine taken 4 months

after production, which show a significant volume fraction of residual cement grains (see Fig. 6 of Dohnalík et al. (2021)), underlining that there is still hydratable matter left. In order to extrapolate the evolution of the uniaxial compressive strength of Biodentine beyond material ages of 14 days, $f_{c,14d}$ according to Eq. (4.12) and s_{Bio} according to Eq. (4.9) are inserted into Eq. (4.6). Evaluation of the resulting expression for a material age of four months ($t = 120$ days) delivers:

$$f_c(4 \text{ months}) = 257.4 \text{ MPa} \times \exp \left[0.06 \times \left(1 - \sqrt{\frac{14 \text{ days}}{120 \text{ days}}} \right) \right] = 267.8 \text{ MPa}. \quad (4.13)$$

Notably, at the material age of 4 months, grid nanoindentation tests were performed on Biodentine (Dohnalík et al., 2021).

4.4 Microscopic origin of the macroscopic uniaxial compressive strength of mature Biodentine

Grid nanoindentation testing of Biodentine and of chemically comparable construction cement pastes, respectively, have shown that both types of materials consist of two populations of hydrates (= products of the chemical reaction between binder and water). As for construction cement pastes, low-density calcium-silicate hydrates (C-S-H) are distinguished from high-density C-S-H (Tennis and Jennings, 2000; Jennings, 2000; Constantinides and Ulm, 2004). Biodentine, in turn, consists of lower-density calcite-reinforced (LDCR) hydrates and high-density calcite-reinforced (HDCR) hydrates (Dohnalík et al., 2021). The microstructure of construction cement pastes typically consists of two times more low-density than high-density C-S-H (Constantinides and Ulm, 2004), and the strength properties of low-density C-S-H (Sarris and Constantinides, 2013) can be upscaled to explain the macroscopic strength of construction cement pastes (Pichler et al., 2013; Pichler and Hellmich, 2011) and of related concretes (Königsberger et al., 2018). The microstructure of Biodentine, in turn, consists of six times more HDCR than LDCR hydrates (Dohnalík et al., 2021), and the macroscopic strength of Biodentine is significantly larger than that of construction cement pastes.

The described similarities and differences suggest that the superior macrostrength of Biodentine is triggered by microscopic failure of the HDCR rather than the LDCR hydrates. In addition, the sudden, well-spread brittle failure of Biodentine indicates that a large portion of the HDCR hydrates fail as soon as the macroscopic loading reaches the strength of the material. This provides the motivation to study mature Biodentine subjected to its uniaxial compressive strength, to downscale these macrostresses to microscopic stress states experienced by the HDCR population of hydrates, and to insert these microstresses into a microscopic failure criterion in order to determine the degree of utilization in the HDCR population of hydrates. Before doing so, two essential prerequisites are revisited: (i) results from a grid nanoindentation testing campaign performed on polished surfaces of mature Biodentine (Dohnalík et al., 2021), and (ii) a micromechanics model which allows for downscaling macrostresses imposed on a representative volume of mature Biodentine to microstresses experienced by the HDCR population of hydrates (Dohnalík et al., 2022).

4.4.1 Results from grid nanoindentation on mature Biodentine (Dohnalík et al., 2021)

5748 nanoindentation tests into mature Biodentine were performed with a Berkovich tip (Dohnalík et al., 2021). Imposing maximum indentation forces of 1 mN resulted in maximum

indentation depths of on average 140 nm. Only two experiments had to be excluded, because their maximum indentation depths were smaller than 45 nm and, therefore, did not satisfy the requirement of being at least 2.5-times larger than the root-mean-squared average surface roughness (Miller et al., 2008; Donnelly et al., 2006), which amounted to 18 nm (Dohnalik et al., 2021). 5746 force-displacement diagrams were evaluated based on the Oliver-Pharr formulae for nanoindentation into infinite halfspaces (Oliver and Pharr, 1992). The obtained histograms of the indentation modulus and of the indentation hardness were represented by the superposition of three lognormal probability density functions, see Fig. 4.8. Lognormal

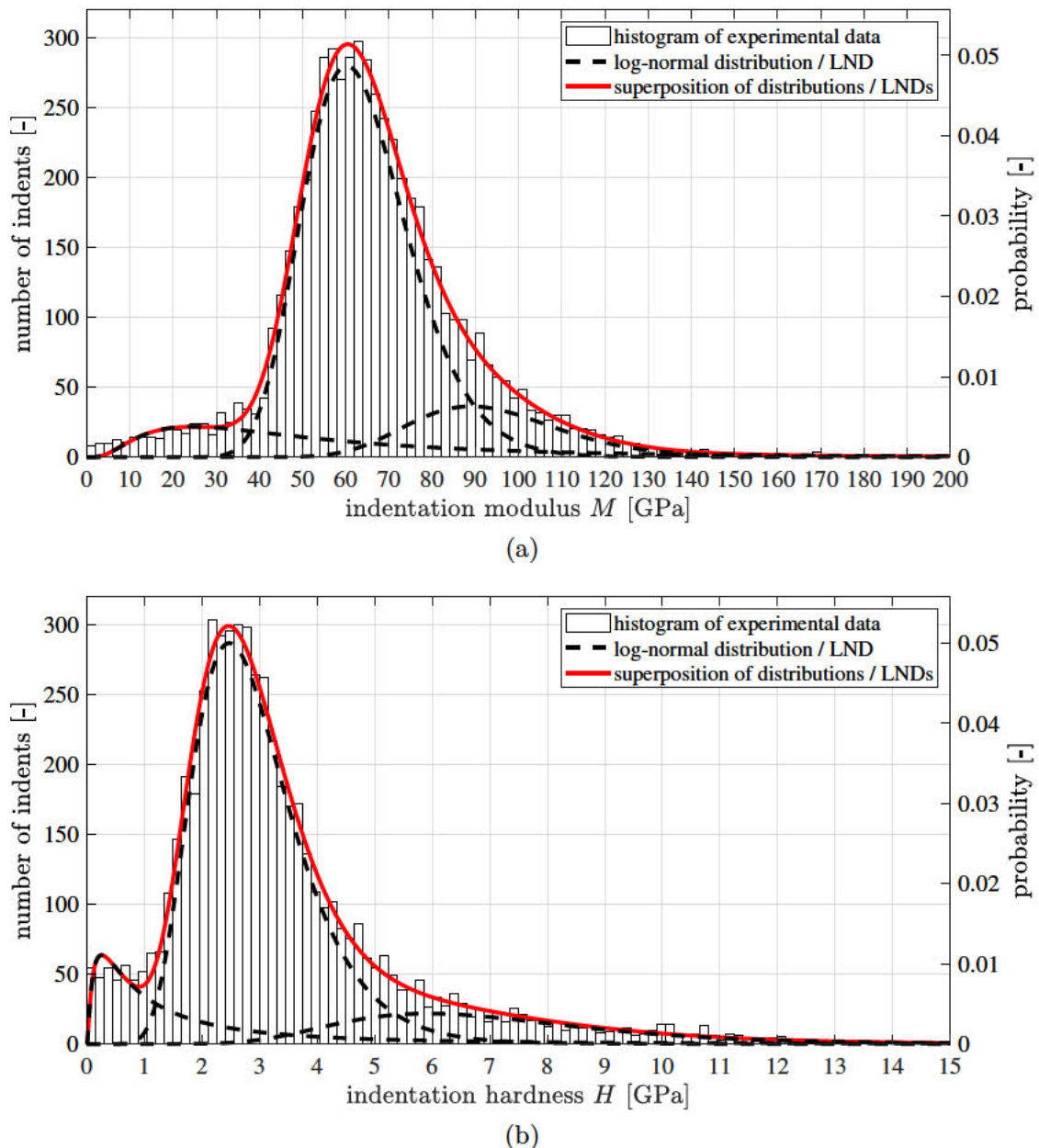


Fig. 4.8. Histograms (a) of indentation modulus and (b) of the indentation hardness, approximated by means of the superposition of three lognormal distributions; after Dohnalik et al. (2021).

distributions were used rather than Gaussians, because (i) the indentation moduli are strictly

positive quantities, and (ii) the large number of indentation experiments revealed skewed rather than symmetric stiffness distributions. The rightmost lognormal distributions in Fig. 4.8 refer to the stiff inclusions zirconia and clinker (indices $i = 1$ and $i = 2$, respectively), the central distributions to HDCR hydrates ($i = 3$), and the leftmost to LDCR hydrates ($i = 4$), see Dohnalík et al. (2021) and Table 4.8. This underlines the existence of two types of hydrates

Table 4.10

Results obtained from grid nanoindentation testing (Dohnalík et al., 2021): values of medians, modes, and volume fractions associated with the three lognormal distributions representing the histogram of indentation moduli in Fig. 4.8.

lognormal distribution	indentation modulus median/mode [GPa]	indentation hardness median/mode [GPa]	volume fraction [-]
LDCR hydrates	45.1/24.5	1.15/0.26	0.1228
HDCR hydrates	62.6/60.2	2.78/2.47	0.7420
clinker/zirconia	92.2/89.0	6.66/5.93	0.1352
		sum:	1.0000

reinforced by calcite particles of single-to-submicrometric size (Li et al., 2019). The two populations of hydrates are reminiscent of construction cement pastes in which inner and outer products (Taplin, 1959), phenograin and groundmass (Diamond and Bonen, 1993), low-density and high-density C-S-H (Tennis and Jennings, 2000; Jennings, 2000), as well as class-A and class-B C-S-H (Königsberger et al., 2016) are distinguished.

Evaluation of nanoindentation tests into the stiff clinker and zirconia grains, based on the Oliver-Pharr formulae mentioned above, led to smaller-than-expected indentation moduli, because the grains acted like larger indenters pressed into the softer surrounding hydrated material. This effect has been shown explicitly by image-supported grid nanoindentation, applied to two different types of cementitious materials (Ma et al., 2017; Königsberger et al., 2021). Hence, we resort to the well known elastic properties of clinker and zirconia which are taken from the literature, see Table 4.11. The volume fractions of all four types of solid constituents are taken from Dohnalík et al. (2021).

Table 4.11

Input quantities of the solid material constituents: bulk moduli, k_i , shear moduli g_i , as well as lognormal parameters μ_i and σ_i which are consistent with median and mode values listed in Table 4.10; input values taken from Hussey and Wilson (1998); Pichler and Hellmich (2011); Dohnalík et al. (2021).

phase	index	stiffness properties		vol. fraction
zirconia	$i = 1$	$k_1 = 170.8$ GPa	$g_1 = 78.8$ GPa	$f_1 = 0.0182$
clinker	$i = 2$	$k_2 = 116.7$ GPa	$g_2 = 53.8$ GPa	$f_2 = 0.1170$
HDCR hydrates	$i = 3$	$\mu_3 = 4.14$	$\sigma_3 = 0.20$	$f_3 = 0.7420$
LDCR hydrates	$i = 4$	$\mu_4 = 3.81$	$\sigma_4 = 0.78$	$f_4 = 0.1228$

The two populations of hydrates exhibit lognormal stiffness distributions, see Table 4.10.

The probability distribution functions of their indentation moduli M read as:

$$\varphi_i(M) = \frac{1}{M\sigma_i\sqrt{2\pi}} \exp\left(-\frac{1}{2}\left[\frac{\ln(M) - \mu_i}{\sigma_i}\right]^2\right), \quad i = 3, 4. \quad (4.14)$$

Indentation moduli are functions of the elastic stiffness properties of the nanoindentation-probed domain and of the diamond tip of the indenter. For an isotropic domain, this function reads as (Oliver and Pharr, 1992)

$$\frac{1}{M} = \frac{1 - \nu_h^2}{E} + \frac{1 - 0.07^2}{1141 \text{ GPa}}, \quad (4.15)$$

where E and ν_h denote the modulus of elasticity and Poisson's ratio of the hydrates. The latter is constant and amounts to (Dohnalík et al., 2022)

$$\nu_h = 0.2017. \quad (4.16)$$

In other words, the distribution of indentation modulus is related to a corresponding distribution of the modulus of elasticity, E . The latter distribution follows from solving Eq. (4.15) for E :

$$E(M) = \frac{1 - \nu_h^2}{\frac{1}{M} - \frac{1 - 0.07^2}{1141 \text{ GPa}}}. \quad (4.17)$$

The sought bulk moduli $k_i(M)$ and the shear moduli $g_i(M)$ follow from standard relations for isotropic elastic media:

$$k_i(M) = \frac{E(M)}{3(1 - 2\nu_h)}, \quad i = 3, 4, \quad (4.18)$$

$$g_i(M) = \frac{E(M)}{2(1 + \nu_h)}, \quad i = 3, 4. \quad (4.19)$$

4.4.2 Continuum micromechanics model for the elastic stiffness of mature Biodentine (Dohnalík et al., 2022)

Continuum micromechanics models account for key features of microheterogeneous materials: the stiffness constants of the material phases, their volume fractions, their characteristic phase shapes, and the specific type of interaction between the phases. Biodentine consists of five types of constituents: zirconia (index $i = 1$), clinker ($i = 2$), HDCCR hydrates ($i = 3$), LDCCR hydrates ($i = 4$), and grain boundary defects modeled as closed microcracks ($i = 5$). The microstructure of Biodentine is represented as a highly disordered (“polycrystalline”) arrangement of material constituents which exhibit direct phase-to-phase interaction, see Fig. 4.9. As regards phase shapes, all four types of solid constituents are represented as spherical phases. The microcracks are introduced as circular slit cracks isotropically oriented in space (Dormieux et al., 2006; Zhu et al., 2011).

The stiffness of all solid constituents is isotropic. Their elastic stiffness properties are fully described based on known values of their bulk moduli k_i and shear moduli g_i , see Table 4.11 as well as Eqs. (4.14)–(4.19).

Phase volume fractions of the solid constituents add up to 1, see Table 4.11, because the volume fraction of closed microcracks is zero. The effect of such microcracks on the overall material behavior is quantified by means of the dimensionless crack density parameter of

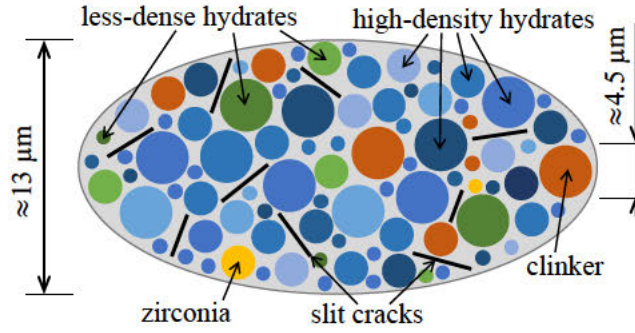


Fig. 4.9. Micromechanical representation of Biodentine (“material organogram”): the two-dimensional sketch shows qualitative properties of a three-dimensional representative volume element of the *lognormal* microelasticity model which accounts for stiffness *distributions* of two populations of hydrates.

Budiansky and O’Connell (1976), see also Pensée et al. (2002); Deudé et al. (2002). As for Biodentine, the crack density parameter amounts to (Dohnalík et al., 2022):

$$\omega = 0.7802, \quad (4.20)$$

Stress downscaling, from the macroscopic stress Σ imposed on a representative volume element of mature Biodentine, down to microscopic stresses of the two populations of hydrates is based on stress downscaling tensors $\mathbb{B}_3(M)$ and $\mathbb{B}_4(M)$

$$\sigma_i(M) = \mathbb{B}_i(M) : \Sigma, \quad i = 3, 4. \quad (4.21)$$

The stress downscaling tensors are isotropic

$$\mathbb{B}_i(M) = B_{vol,i}(M) \mathbb{I}^{vol} + B_{dev,i}(M) \mathbb{I}^{dev}, \quad i = 3, 4, \quad (4.22)$$

where \mathbb{I}^{vol} and \mathbb{I}^{dev} stand for the volumetric and deviatoric parts of the symmetric fourth-order identity tensor \mathbb{I} . Their components read as $I_{ijkl} = (\delta_{ik}\delta_{jl} + \delta_{il}\delta_{jk})/2$, $I_{ijkl}^{vol} = (\delta_{ij}\delta_{kl})/3$, and $I_{ijkl}^{dev} = I_{ijkl} - I_{ijkl}^{vol}$, where δ_{ij} is the Kronecker delta which is equal to 1 for $i = j$, and equal to 0 otherwise. The volumetric and deviatoric components of the stress downscaling tensors, $B_{vol,i}(M)$ and $B_{dev,i}(M)$, respectively, read as (Dohnalík et al., 2022)

$$B_{vol,i}(M) = \frac{k_i(M)/k_{bio}}{1 + \frac{S_{vol}(k_i(M)-k_{bio})}{k_{bio}}} \left\{ \sum_{i=1}^2 \frac{f_i}{1 + \frac{S_{vol}(k_i-k_{bio})}{k_{bio}}} + \sum_{i=3}^4 f_i \int_0^\infty \frac{\varphi_i(M)}{1 + \frac{S_{vol}(k_i(M)-k_{bio})}{k_{bio}}} dM \right\}^{-1}, \quad (4.23)$$

$$B_{dev,i}(M) = \frac{g_i(M)/g_{bio}}{1 + \frac{S_{dev}(g_i(M)-g_{bio})}{g_{bio}}} \left\{ \sum_{i=1}^2 \frac{f_i}{1 + \frac{S_{dev}(g_i-g_{bio})}{g_{bio}}} + \sum_{i=3}^4 f_i \int_0^\infty \frac{\varphi_i(M)}{1 + \frac{S_{dev}(g_i(M)-g_{bio})}{g_{bio}}} dM + \frac{4\pi\omega}{3} T_{dev} \right\}^{-1}, \quad (4.24)$$

where $i = 3, 4$ and $M \in \mathbb{R}^{0,+}$ and

$$S_{vol} = \frac{3k_{bio}}{3k_{bio} + 4g_{bio}}, \quad (4.25)$$

$$S_{dev} = \frac{6(k_{bio} + 2g_{bio})}{5(3k_{bio} + 4g_{bio})} \quad (4.26)$$

$$T_{dev} = \frac{8(3k_{bio} + 4g_{bio})}{15\pi(3k_{bio} + 2g_{bio})}, \quad (4.27)$$

$$k_{bio} = 38.4 \text{ GPa}, \quad (4.28)$$

$$g_{bio} = 14.1 \text{ GPa}, \quad (4.29)$$

where S_{vol} and S_{dev} denote the volumetric and deviatoric components of the Eshelby tensor of a spherical inclusion in an infinite matrix with the stiffness of mature Biodentine, T_{dev} accounts for the influence of the microcracks, and k_{bio} and g_{bio} are the macroscopic “homogenized” bulk and shear moduli of mature Biodentine (Dohnalík et al., 2022). The integrals of Eqs. (4.23) and (4.24) are listed in Appendix B of Dohnalík et al. (2022).

4.4.3 Microscopic stress distributions in calcite-reinforced hydrates as a function of their indentation modulus

So far, the sign convention used in material testing of cementitious materials was used: compression was described with a positive mathematical sign. From now on, the sign convention used in continuum mechanics is used: compressive normal stresses are described with a negative mathematical sign, tensile normal stresses are positive.

In order to explain the microscopic origin of the macroscopic uniaxial compressive strength of mature Biodentine according to Eq. (4.13), a Cartesian coordinate system is introduced such that the direction of uniaxial compression is aligned with the z -direction. Thus, the stress state at failure is expressed as

$$\Sigma = -267.8 \text{ MPa} \times (\mathbf{e}_z \otimes \mathbf{e}_z). \quad (4.30)$$

Stress downscaling according to Eqs. (4.21)–(4.29) delivers axisymmetric microscopic principal stress states experienced by the two populations of hydrates. Denoting the normal stress component in the axial z -direction as σ_{axi} and the normal stress components in the lateral x - and y -directions as σ_{lat} , the microscopic stress states read as

$$\sigma_i(M) = \sigma_{i,axi}(M) \times (\mathbf{e}_z \otimes \mathbf{e}_z) + \sigma_{i,lat}(M) \times (\mathbf{e}_x \otimes \mathbf{e}_x + \mathbf{e}_y \otimes \mathbf{e}_y), \quad i = 3, 4, \quad (4.31)$$

see also Fig. 4.10. The absolute values of the compressive axial normal stresses increase with increasing indentation modulus of the HDCR hydrates. The lateral principal normal stresses are negligibly small compared to the axial normal stresses.

4.4.4 Shear failure of calcite-reinforced hydrates

Cementitious hydration products resulting from the dissolution of dicalcium and tricalcium silicate and from precipitation of solids out of the oversaturated porewater solution, are known to exhibit pressure-sensitive shear failure (Constantinides et al., 2006; Sarris and

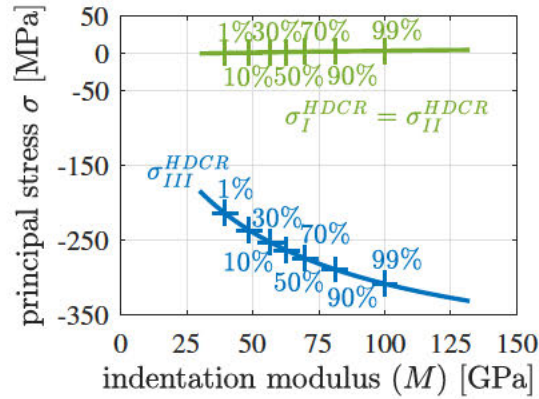


Fig. 4.10. Axial (blue) and lateral (green) components of the microscopic principal stress states experienced by the HDCR population of hydrates, as a function of the indentation modulus M ; standard sign convention of continuum mechanics: compression is negative, tension is positive.

Constantinides, 2013; Pichler et al., 2013; Königsberger et al., 2018). The corresponding Mohr-Coulomb failure criterion reads as:

$$f(\sigma) = \sigma_I \frac{1 + \sin \varphi}{2c \cos \varphi} - \sigma_{III} \frac{1 - \sin \varphi}{2c \cos \varphi} \leq 1, \quad (4.32)$$

where σ_I denotes the largest principal normal stress, σ_{III} the smallest principal normal stress, c the cohesion, and φ the angle of internal friction. $f(\sigma) < 0$ refers to stress states sustained by the material by means of linear elastic behavior, while $f(\sigma) = 0$ refers to brittle failure. Recalling that $\sigma_{lat} = \sigma_I$ is negligibly small compared to $\sigma_{axi} = \sigma_{III} < 0$ and introducing an equivalent shear strength C such that $1/(2C)$ is equal to the term multiplied by σ_{III} in Eq. (4.32),

$$C = c \frac{\cos \varphi}{1 - \sin \varphi}, \quad (4.33)$$

the failure criterion according to Eq. (4.32) can be rewritten as

$$\frac{|\sigma_{axi}|}{2} \leq C, \quad (4.34)$$

where the $<$ sign refers to linear elastic behavior and the $=$ sign to brittle failure. Notably, $|\sigma_{axi}|$ increases with increasing stiffness of the hydrates, see Fig. 4.10. Given that the indentation modulus and the indentation hardness of the hydrates are lognormally distributed, it is to be expected that also the equivalent shear strength is lognormally distributed. This provides the motivation to establish correlations between lognormal distributions of indentation modulus, indentation hardness, and the equivalent shear strength.

4.4.5 Correlations between lognormal distributions of indentation modulus, indentation hardness, and the equivalent shear strength

Correlations between lognormal distributions of the indentation modulus M , the indentation hardness H , and the equivalent shear strength C are established by relating all p -quantiles of any lognormal distribution to the same p -quantiles of the other two lognormal distributions. To this end, we introduce the p -quantiles of two lognormal distributions referring to statistical

variables X and Y as

$$X_p = \exp(\mu_X + u_p \sigma_X), \quad (4.35)$$

$$Y_p = \exp(\mu_Y + u_p \sigma_Y), \quad (4.36)$$

with $X \in [M, H, C]$ and $Y \in [M, H, C]$. In Eqs. (4.35) and (4.36), σ_X and μ_X as well as σ_Y and μ_Y denote the parameters of the two lognormal distributions, and u_p stands for the p -quantile of the standard normal distribution. Solving both Eqs. (4.35) and (4.36) for u_p , setting the two resulting expressions equal to each other, and transforming the resulting expression as detailed in Appendix 4.A, yields the following remarkable result: relating any p -quantile of one lognormally distributed statistical variable X to the same p -quantile of another lognormally distributed statistical variable Y leads to the following power-law relation between the two statistical variables:

$$Y = \exp\left(\mu_Y - \frac{\sigma_Y}{\sigma_X} \mu_X\right) \times X^{\frac{\sigma_Y}{\sigma_X}}. \quad (4.37)$$

Setting X equal to the indentation hardness H as well as Y equal to the indentation modulus M , yields a power-law describing that the stiffness increases underlinearly with increasing strength, see Fig. 4.11(a), (b). This is qualitatively reminiscent of similar power-law relations between stiffness and strength of mature construction concretes, see the *fib* Model Code 2010 (International Federation for Structural Concrete, 2010) and Fig. 6 of (Ausweger et al., 2019).

4.4.6 Identification of lognormal parameters of the equivalent shear strength

The microscopic stresses experienced by the hydrates, see Fig. 4.10, were obtained from downscaling the macroscopic uniaxial compressive *strength* of mature Biodentine. Thus, one specific portion of the HDCR hydrates (with one specific value of the indentation modulus) must fulfill the failure criterion (4.34), consider the = sign in (4.34), while the < sign applies to all other hydrates. This represents a side condition for the sought lognormal distribution of the equivalent shear strength.

As for identification of the lognormal distributions of the equivalent shear strength of the HDCR hydrates, is useful to illustrate their stress states as a function of their indentation modulus in a double logarithmic fashion, see Fig. 4.11(c), where the ordinate refers to $\log|\sigma_{axi}/2|$ rather than to $\log|\sigma_{axi}|$, because the figure will be used to illustrate the failure criterion (4.34).

The *sought* lognormal distribution of the equivalent shear strength is related to the *known* lognormal distribution of the indentation modulus by correlating their quantiles as explained in Subsection 4.4.5. The resulting power-law is obtained from setting X equal to M and Y equal to C in Eq. (4.37):

$$C = \exp\left(\mu_C - \frac{\sigma_C}{\sigma_M} \mu_M\right) \times M^{\frac{\sigma_C}{\sigma_M}}, \quad (4.38)$$

where $\mu_M = 4.14$ and $\sigma_M = 0.20$, see Table 4.11, while μ_C and σ_C are to be identified. As for adding a graphical illustration of Eq. (4.38) to Fig. 4.11(c), a second ordinate showing $\log(C)$ is added. The power-law (4.38) refers to a straight line in Fig. 4.11(c). This straight line can be moved and rotated in Fig. 4.11(c), by means of assigning different values to μ_C and σ_C . A realistic pair of values is identified such that the straight line becomes the tangent

to the graph showing $\log|\sigma_{axi}/2|$ over $\log(M)$. The contact point refers to those hydrates which fulfill the failure criterion (4.34). Given that median stiffness values have been shown to be the most representative values of lognormal distributions when it comes to upscaling of the elastic stiffness (Dohnalík et al., 2022), we here assume that the microstresses experienced by the hydrates with the median stiffness are relevant for strength upscaling. In other words, μ_C and σ_C are identified such that the graph of Eq. (4.38) touches the graph of the axial stresses at the median value of M , i.e. at the 50% quantile of M , amounting to 62.6 GPa for the studied HDCR hydrates, see Fig. 4.11(c) and Table 4.10. The corresponding lognormal parameters of the distributions of the equivalent shear strength of the HDCR hydrates read as

$$\mu_C = 4.879, \quad (4.39)$$

$$\sigma_C = 0.078. \quad (4.40)$$

The corresponding probability density function of the equivalent shear strength is illustrated in Fig. 4.11(d). Corresponding values of the mode, the median, and the mean value are listed in Table 4.12. The lognormal distribution of the effective shear strength is only slightly

Table 4.12

Mode, median, and mean value of the lognormal distribution of the equivalent shear strength C of the HDCR hydrates, see also Eqs. (4.39) and (4.40).

mode [MPa]	median [MPa]	mean [MPa]
130.7	131.5	131.9

skewed. This is in agreement with the only slightly skewed distributions of the indentation modulus and hardness of the HDCR hydrates.

4.4.7 Degree of utilization of hydrates as a function of their indentation moduli

The degree of utilization is a dimensionless stress-based quantity ranging from 0 to 1. The value 0 refers to a stress-free configuration; the value 1 to failure. The larger the degree of utilization, the closer is the investigated stress state to the strength of the analyzed material. A mathematical expression describing the degree of utilization \mathcal{F} is obtained from dividing the failure criterion (4.34) by C

$$\mathcal{F} = \frac{|\sigma_{axi}|}{2C} \leq 1, \quad (4.41)$$

where both the microstresses σ_{axi} and the equivalent shear strength C are functions of the indentation modulus, see Fig. 4.11(c). The corresponding evaluation of Eq. (4.41) underlines that the maximum attainable degree of utilization, $\mathcal{F} = 1$, is only reached by the hydrates with indentation modulus equal to the median value, while all other hydrates have degrees of utilization smaller than 1, see Fig. 4.12(a). Still, it is remarkable that the degree of utilization of all HDCR hydrates is larger than some 93%. This underlines that mature Biodentine is a highly optimized material.

4.4.8 Shear failure of HDCR hydrates explains macroscopic strength of mature Biodentine

Mature Biodentine fails in a brittle fashion. Corresponding specimens break into a very high number of fragments once the strength is reached. Therefore, it is likely that many

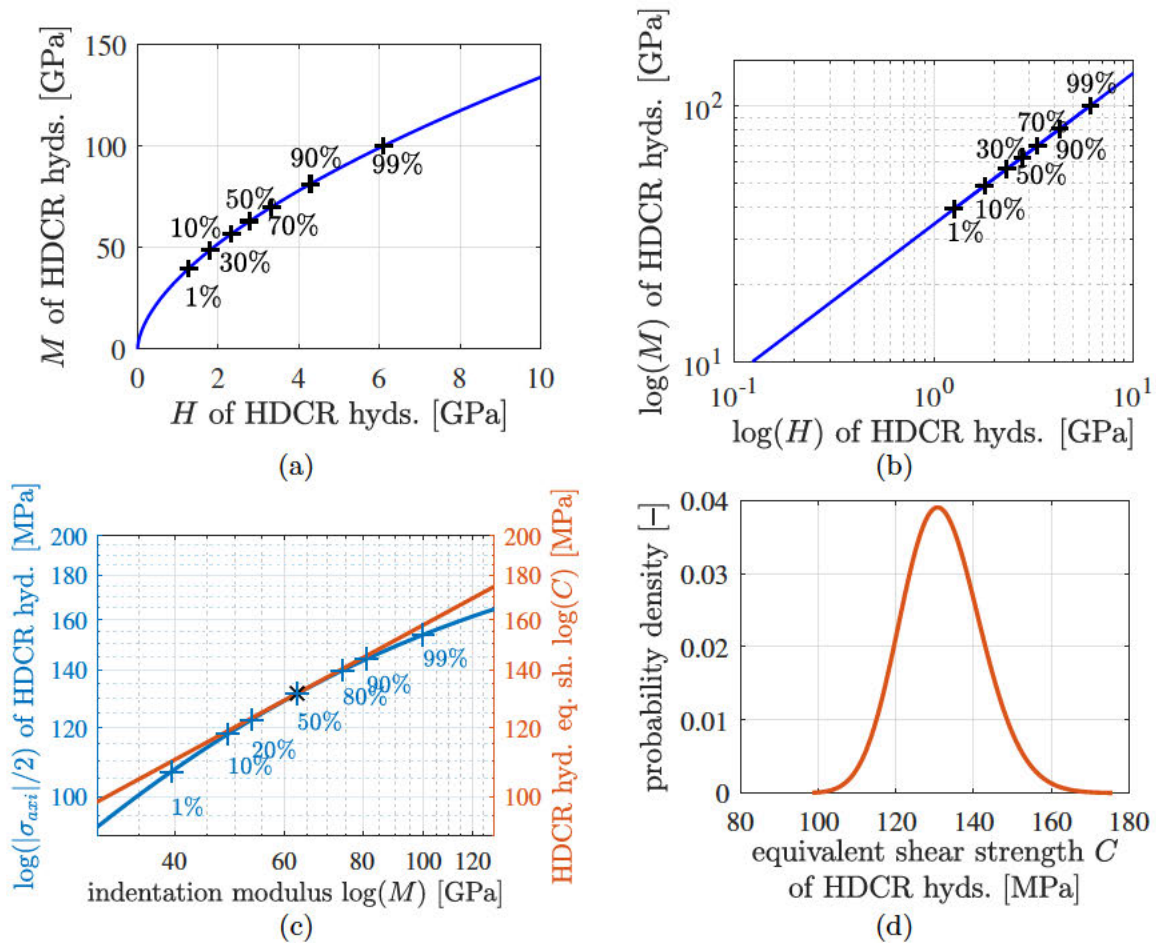


Fig. 4.11. (a), (b) Quantile-based correlation between the lognormal distributions of the indentation modulus M and the indentation hardness H of the HDCR hydrates: representation of the power-law-relation according to Eq. (4.37) with $X = H$, $Y = M$, $\mu_M = 4.14$, $\sigma_M = 0.20$, $\mu_H = 1.02$, and $\sigma_H = 0.34$, see Table 4.11 and Dohnalík et al. (2021): (a) natural scale, (b) double-logarithmic representation; the black “+” symbols mark p -quantiles, with values of p equal to the printed percentage values. (c) Illustration of the failure criterion (4.34): the equivalent shear strength of all HDCR hydrates (orange line) is larger than $|\sigma_{axi}|/2$ (blue line), except for the median value of the indentation modulus, for which $|\sigma_{axi}|/2 = C$; the blue “+” symbols mark p -quantiles, with values of p given as percentage values. (d) Lognormal probability density distribution of the equivalent shear strength of the HDCR hydrates explaining macroscopic failure of mature Biodentine under uniaxial compression according to Eq. (4.30); the lognormal parameters are given in Eqs. (4.39) and (4.40).

hydrates fail at virtually the same macroscopic stress intensity. This provides the motivation to quantify the amount of hydrates which have a degree of utilization of 99% or larger. All HDCR hydrates between the 7.6%-quantile and the 92.2%-quantile have degrees of utilization larger than or equal to 99%, see Fig. 4.12(b). In other words, $92.2\% - 7.6\% = 84.6\%$ of the

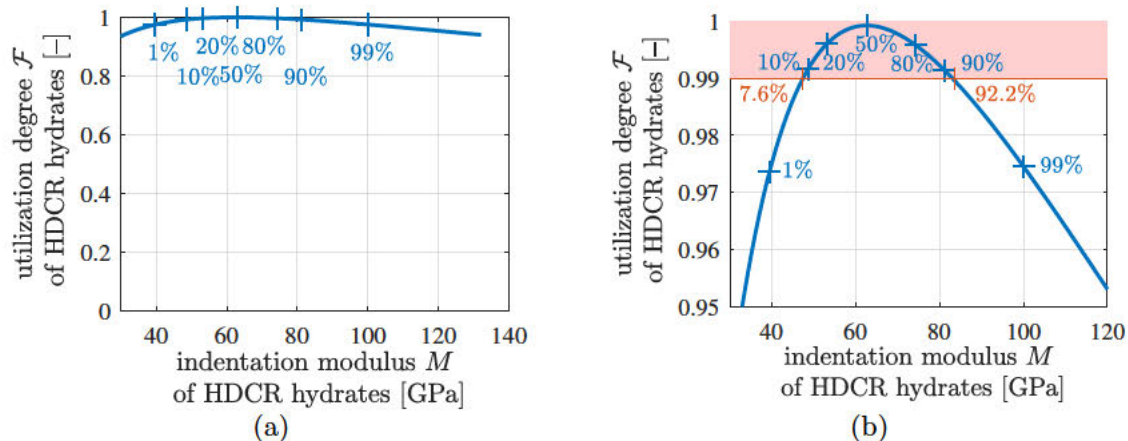


Fig. 4.12. Degree of utilization $\mathcal{F} = |\sigma_{axi}|/(2C)$ as a function of the indentation modulus M for HDCR hydrates; the “+” symbols mark p -quantiles, with values of p given as percentage values.

HDCR hydrates have a degree of utilization larger than or equal to 99%. Therefore, they will fail virtually simultaneously. Given that HDCR hydrates make up 74.20% of the volume of Biodentine, see Table 4.11, $84.6\% \times 74.20\% = 62.8\%$ of the volume of Biodentine fails at the same time. This is consistent with destructive mechanical testing having the Biodentine samples broken into many fragments.

The presented analysis was carried out under the assumption that the HDCR population of hydrates is responsible for failure of mature Biodentine. Repeating the analysis under the alternative assumption that the LDCR population of hydrates triggers failure of mature Biodentine, see Appendix 4.B, leads to the results that only 3.5% of the volume of Biodentine would fail virtually at the same time, but that would lead to pre-peak nonlinearities rather than to the experimentally observed sudden brittle mode of failure associated with many fragments.

4.5 Conclusions

Cylindrical specimens of Biodentine, with slenderness ratios of 1.84 and 1.34, respectively, were subjected to destructive compression tests at material ages from 1 hour to 28 days. The results were analyzed by means of (i) formulae from two standards for construction concretes (the *fib* Model Code 2010 (International Federation for Structural Concrete, 2010) and the ASTM C39 (American Society for Testing and Materials, 2021)), as well as (ii) a micromechanics model for mature Biodentine (Dohnalík et al., 2022), which accounts for two populations of hydrates with lognormally distributed stiffness properties, as quantified from the results of a comprehensive grid nanoindentation testing campaign (Dohnalík et al., 2021). From the results of the presented study, the following conclusions are drawn:

- Biodentine exhibits some pre-peak ductility only during the first 90 minutes after production. After that, the material behaves virtually linear elastic all the way up

to sudden brittle failure. Very young specimens showed axial splitting at the lateral surface, leaving behind fragments reminiscent of two cones, whereby the bases of the two cones were located at the interfaces between specimen and the load plates, and the two tips of the cones touched each other at the center of the specimen. At material ages amounting to 1 day and older, the specimens broke into many fragments, so that classical categorizations concerning the propagation direction of single cracks are not useful anymore.

- The evolution of the uniaxial compressive strength of Biodentine curing at 37°C can be described by means of adapting an empirical formula from the *fib* Model Code 2010 (International Federation for Structural Concrete, 2010), which refers to construction concretes curing at 20°C. This underlines that the strength evolution of Biodentine is qualitatively similar to that of construction concretes. Quantitatively, however, Biodentine outperforms cementitious construction materials: the strength evolution of Biodentine is significantly faster and leads to a by far larger “final” strength compared to chemically comparable construction cement pastes.
- The smaller the length-to-diameter ratio (“slenderness ratio”) of cylindrical specimens of Biodentine, the larger is the maximum force sustained by these specimens when crushed under uniaxial compression. Empirical correction factors of the ASTM C39 for concrete cylinders with a length-to-diameter ratio smaller than 2, applied to 14-days-strength values of cylindrical Biodentine specimens with slenderness-ratios of 1.84 and 1.34, respectively, delivered virtually *the same* estimate of the uniaxial compressive strength at that material age. This indicates that the correction factors account for a structural effect rather than for a material property. This was further corroborated by the observation that ratio of the strength values of two types of cylindrical Biodentine specimens is in good approximation constant throughout the curing process.
- Microscopic stress states in both populations of hydrates of Biodentine, computed by means of a micromechanics model accounting for lognormal stiffness distributions of two populations of hydrates (Dohnalík et al., 2022), are in good approximation *uniaxial* compressive stress states, because the principal normal stresses in lateral direction are by two orders of magnitude smaller than the dominating principal normal stresses aligned with the axis of macroscopic uniaxial loading. In addition, the dominating axial normal stresses are the larger, the larger the stiffness of the hydrates.
- Correlating quantiles of two lognormal distributions results in a power-law relation between the two statistical variables. The indentation modulus of the high-density calcite-reinforced hydrates of Biodentine, for instance, increases underlinearly with increasing indentation hardness. This is qualitatively reminiscent of similar power-law relations between stiffness and strength of mature construction concretes, see the *fib* Model Code 2010 (International Federation for Structural Concrete, 2010) and Fig. 6 of (Ausweger et al., 2019). Given that indentation modulus *and* hardness of both populations of hydrates of Biodentine are lognormally distributed (Dohnalík et al., 2022), the probability density function of the effective shear strength of the high-density calcite-reinforced hydrates of Biodentine was introduced to be of lognormal nature as well.
- Assuming that macroscopic strength of Biodentine results from failure of the high-density calcite-reinforced hydrates with indentation modulus equal to the median value, it was

found that some 85% of the high-density calcite-reinforced hydrates have virtually the same degree of utilization (= stress-to-strength ratio). Because the high-density calcite-reinforced hydrates occupy some 74% of the volume of Biodentine, the analysis underlines that some 63% of the volume of Biodentine fail at virtually the same macroscopic loading. This is a plausible explanation for the very brittle failure mode of Biodentine, and it underlines that the material is very highly optimized for strength.

Acknowledgments

This project has received funding from the European Union's Horizon 2020 research and innovation programme under the Marie Skłodowska-Curie Grant Agreement No. 764691. The authors gratefully acknowledge the support of R&D team at Septodont, 105 Av. Beaurepaire, Saint-Maur-des-Fossés, France, concerning preparation of the specimens and compressive strength experiments.

Appendix 4.A Quantile-based correlation between two lognormal distributions

Solving both Eqs. (4.35) and (4.36) for u_p and setting the two resulting expressions equal to each other yields

$$\frac{1}{\sigma_X} [\ln(X_p) - \mu_X] = \frac{1}{\sigma_Y} [\ln(Y_p) - \mu_Y]. \quad (4.A.1)$$

Solving the Eq. (4.A.1) for $\ln(Y_p)$ yields

$$\ln(Y_p) = \mu_Y + \frac{\sigma_Y}{\sigma_X} [\ln(X_p) - \mu_X]. \quad (4.A.2)$$

Re-arranging terms and making use of “ $a \ln(b) = \ln(b^a)$ ” on the right side of Eq. (4.A.2) yields

$$\ln(Y_p) = \left(\mu_Y - \frac{\sigma_Y}{\sigma_X} \mu_X \right) + \ln \left(X_p^{\frac{\sigma_Y}{\sigma_X}} \right). \quad (4.A.3)$$

Applying to the term in the first pair of brackets on the right side of Eq. (4.A.3), first the exponential function, and then its inverse, the natural logarithm, yields

$$\ln(Y_p) = \ln \left(\exp \left(\mu_Y - \frac{\sigma_Y}{\sigma_X} \mu_X \right) \right) + \ln \left(X_p^{\frac{\sigma_Y}{\sigma_X}} \right). \quad (4.A.4)$$

Making use of “ $\ln(a) + \ln(b) = \ln(a \times b)$ ” on the right side of Eq. (4.A.4) yields

$$\ln(Y_p) = \ln \left(\exp \left(\mu_Y - \frac{\sigma_Y}{\sigma_X} \mu_X \right) \times X_p^{\frac{\sigma_Y}{\sigma_X}} \right). \quad (4.A.5)$$

Applying the exponential function to both sides of Eq. (4.A.5) finally yields

$$Y_p = \exp \left(\mu_Y - \frac{\sigma_Y}{\sigma_X} \mu_X \right) \times X_p^{\frac{\sigma_Y}{\sigma_X}}. \quad (4.A.6)$$

Given that Eq. (4.A.6) is valid for any p -quantile, the indices p can be omitted. This leads to Eq. (4.37).

Appendix 4.B Analysis of the equivalent shear strength of the LDCR hydrates

In the following, it is checked whether or not the LDCR hydrates could be the microstructural origin of macroscopic failure of mature Biodentine subjected to uniaxial compression. To this end, the macroscopic uniaxial compressive strength, see Eq. (4.30), is downscaled according to Eqs. (4.21)–(4.24) into the LDCR hydrates, see Fig. 4.B.13.

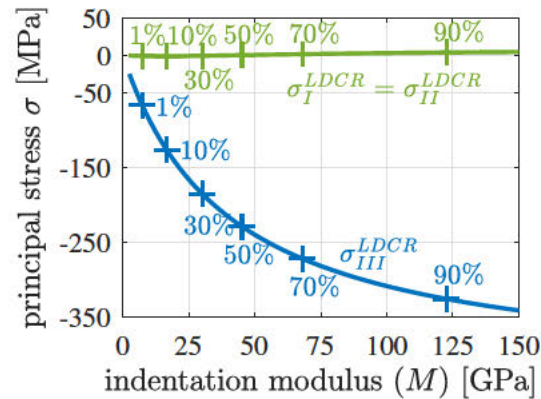


Fig. 4.B.13. Axial and lateral components of the microscopic principal stress states experienced by less-dense calcite-reinforced hydrates, as a function of the indentation modulus M .

The correlation between the lognormal distributions of the indentation modulus M and the indentation hardness H of the LDCR hydrates is illustrated in Fig. 4.B.14(a), (b). In the same way, the known lognormal distribution of the indentation modulus M is correlated with the sought lognormal distribution of the equivalent shear strength C of the LDCR hydrates, see Eq. (4.38). Realistic values of μ_C and σ_C are identified such that the corresponding straight line in Fig. 4.B.14(c) becomes a tangent to the graph showing $\log |\sigma_{axi}/2|$ over $\log(M)$. The contact point refers to the 50% quantile of M . As for the LDCR hydrates, this value amounts to 45.1 GPa, see Fig. 4.B.14(c) and Table 4.10. The corresponding lognormal parameters of the distribution of the equivalent shear strength read as

$$\mu_C = 4.737, \quad (4.B.1)$$

$$\sigma_C = 0.365. \quad (4.B.2)$$

The corresponding probability density function of the equivalent shear strength of the LDCR hydrates is illustrated in Fig. 4.B.14(d). Related values of the mode, the median, and the mean value are listed in Table 4.B.13.

Table 4.B.13

Mode, median, and mean value of the lognormal distribution of the equivalent shear strength C of the LDCR hydrates, see also Eqs. (4.B.1) and (4.B.2).

mode [MPa]	median [MPa]	mean [MPa]
99.9	114.1	122.0

The degree of utilization of all LDCR hydrates is larger than or equal to some 78%. This is smaller than the utilization degree of the HDCR hydrates, compare Figs. 4.B.15(a)

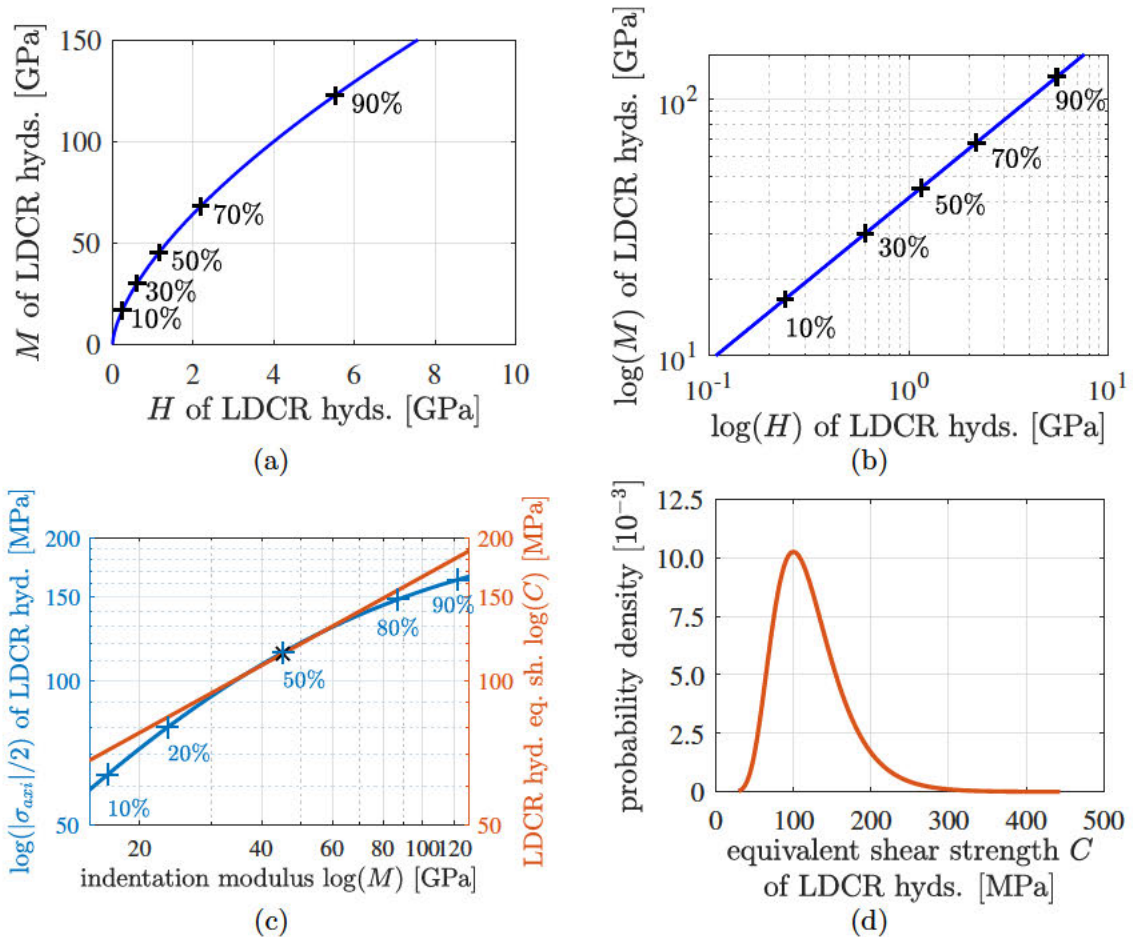


Fig. 4.B.14. (a), (b) Quantile-based power-law correlation between the lognormal distributions of the indentation modulus (see the ordinates) and the indentation hardness (see the abscissas) of the LDCR hydrates: representation of the power-law-relation according to Eq. (4.37) with $X = H$, $Y = M$, $\mu_M = 3.81$, $\sigma_M = 0.78$, $\mu_H = 0.14$, and $\sigma_H = 1.23$, see Table 4.11 and Dohnalík et al. (2021): (a) natural scale, as well as (b) double-logarithmic representation; the black "+" symbols mark p -quantiles, with values of p equal to the printed percentage values. (c) Illustration of the failure criterion (4.34): the equivalent shear strength of all LDCR hydrates is larger than $|\sigma_{axi}|/2$, except for the median value of the indentation modulus, for which $|\sigma_{axi}|/2 = C$; the blue "+" symbols mark p -quantiles, with values of p given as percentage values. (d) Lognormal probability density function of the equivalent shear strength of the LDCR hydrates; lognormal parameters of the distribution are given in Eqs. (4.B.1) and (4.B.2).

and 4.12(a). All LDCR hydrates between the 36.1%-quantile and the 64.6%-quantile have degrees of utilization larger than or equal to 99%, see Fig. 4.B.15(b). Therefore, if the

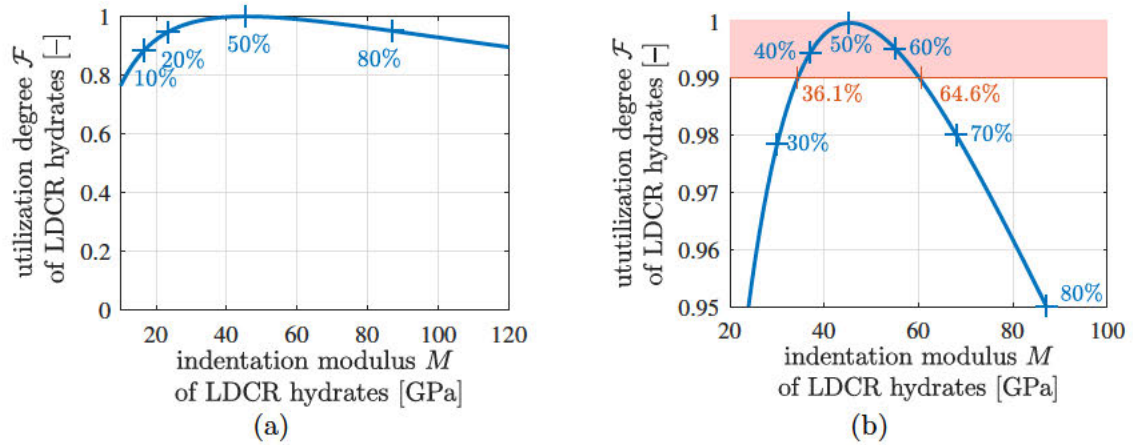


Fig. 4.B.15. Degree of utilization $\mathcal{F} = |\sigma_{axi}|/(2C)$ as a function of the indentation modulus M of LDCR hydrates; the “+” symbols mark p -quantiles, with values of p given as percentage values.

lognormal distribution of the equivalent shear strength according to Fig. 4.B.14(d) is realistic, then $64.6\% - 36.1\% = 28.5\%$ of the LDCR hydrates have a degree of utilization larger than or equal to 99% and will, therefore, fail virtually simultaneously. Given that LDCR hydrates make up 12.3% of the volume of Biodentine, see Table 4.11, $28.5\% \times 12.3\% = 3.5\%$ of the volume of Biodentine will fail at the same time. This does not propose the LDCR hydrates as primary reason for the sudden, well-spread brittle failure of the mature Biodentine specimens under destructive compressive mechanical testing.

Chapter 5

Summary, conclusions, and outlook

5.1 Summary of the experimental studies

The dental cement paste was investigated at microscopic scale by means of the grid nanoindentation technique. From 5748 indentation experiments, only two had to be excluded due to violation of the requirement for minimum indentation depth which is based on the average roughness of the probed surface. Moreover, the individual indents are regarded as being totally independent on each other, considering the typical spacing of $70\ \mu\text{m}$ and the average indentation depth of $139\ \text{nm}$. Indentation modulus and hardness histograms, derived from the Oliver–Pharr solution applied to the thousands of nanoindentation tests, were approximated by means of superposition of two times three lognormal probability density functions. They refer to less-dense calcite-reinforced (LDCR) hydrates, high-density calcite-reinforced (HDCR) hydrates, and to indents into cement clinker and zirconium dioxide. The median values of the three stiffness distribution are used for calculation of upper and lower stiffness bounds as well as stiffness estimation in form of self-consistent scheme. The continuous probability density functions of the LDCR, and HDCR hydrates are used as input for the improved micromechanical model.

Light microscopy imaging provided complementary information about the microstructure of the material probed by grid nanoindentation. In the case of dental cement paste, the color as well as black-and-white microscopy images having resolution of 2584×1936 pixels and 1292×968 pixels with pixel sizes ranging from 0.34 to $0.54\ \mu\text{m}$ gave access to characteristic particle sizes within the Biodentine's microstructure.

Non-destructive ultrasonic pulse transmission technique characterized macroscopic (homogenized) elastic stiffness of dental cement paste from material ages of seven to 28 days. 325 tests were carried out using longitudinal transducers with central frequencies amounting to $50\ \text{kHz}$, $500\ \text{kHz}$, $1\ \text{MHz}$, $2.25\ \text{MHz}$, $5\ \text{MHz}$, $10\ \text{MHz}$, and $20\ \text{MHz}$. The longitudinal waves sent through the material characterized representative volume elements (RVEs) ranging from about $25\ \mu\text{m}$ to approximately $10\ \text{mm}$ which is considerably larger than the biggest microheterogeneity in the material. Similarly, 122 measurements, using shear transducers with central excitation frequencies of $5\ \text{MHz}$ and $2.25\ \text{MHz}$, characterized RVEs of $49.5\ \mu\text{m}$ and $1.1\ \text{mm}$, respectively. Bulk and shear moduli derived from these measurements were used for micromechanical model accounting for two populations of hydrates with lognormally distributed microstiffness properties.

Destructive compression tests characterized strength evolution at nine material ages ranging from 1 hour to 28 days. 122 tests were carried out for two kinds of cylindrical specimens,

different in their length-to-diameter ratio, on which quasi-static loading was imposed. If a specimen was found to be flawed, either by geometric imperfections or by pores entrapped during casting, the obtained result was discarded. The evidence was gathered by means of inspecting the specimen's stress-strain diagram and by a visual check of the specimen itself as well as its fragments after the test (whenever it was possible). The mean strength values of the two kinds of specimens at mature material state are corrected in accordance to ASTM C39 standard, in order to obtain genuine uniaxial compressive strength of the material. The strength evolution formula of *fib* Model Code 2010 was adopted to estimate the uniaxial compressive strength of a four months old dental cement paste, the material age at which the nanoindentation tests were carried out. The result was exploited in the micromechanical model used for explanation of the genuine uniaxial compressive strength of well-hardened Biodentine.

5.2 Summary of the developed models

Upper and lower stiffness bounds as well as upscaled stiffness from self-consistent micromechanical model were calculated based on three median microstiffnesses obtained from grid nanoindentation results. The results were compared to ultrasound-derived “macroscopic” elastic properties. These models provided the starting point for more profound analysis.

A micromechanical model, linking microstructural stiffness properties with macroscopic effective stiffness, was further developed based on previous modeling efforts. In the improved model, the microstructure of dental cement paste is considered as a “polycrystalline” arrangement of five material phases: zirconia, clinker, HDCR hydrates, LDCR hydrates, and grain boundary defects. The latter is modeled as closed microcracks represented by oblate spheroid isotropically oriented in space. The other four solid constituents are represented as spherical phases. The most important feature of this model is that it takes into account the statistical nature of the indentation moduli of the two populations of calcite-reinforced hydrates as an input parameter rather than just one representative stiffness per population. As for the statistical distributions, lognormal probability density functions are adopted, such that positive definiteness of the probed mechanical properties is a priori considered. Because of this aspect, the model is also referred as the lognormal microelasticity model, and allows for:

- quantification of Poisson's ratio of the two populations of calcite-reinforced hydrates,
- identification of the Budiansky and O'Connell's crack density parameter by means of linking the micromechanical model to both nanoindentation and ultrasonic test results,
- quantitative illustration of how macroscopic uniform loading, imposed on a representative volume of dental cement paste, results in microscopic stress and strain distributions inside the two populations of hydrates,
- assessing the potential and the limitations of piecewise uniform microelasticity model.

The latter is based on just one representative stiffness per population of calcite-reinforced hydrates, usually used in micromechanical models for construction cement pastes. The lognormal microelasticity model is a valuable tool for further explanation of the compressive strength.

The sudden brittle failure of the dental cement paste was explained by means of the lognormal microelasticity model loaded by macroscopic stress equal to the genuine uniaxial

compressive strength obtained from the compressive strength experiments. These macrostresses were downscaled to microstresses experienced by the HDCR population of hydrates. The axial normal microstresses, playing a prominent role in Biodentine's strength, were inserted into a microscopic failure criterion, based on which a lognormally distributed equivalent shear strength (cohesion-like quantity) was sought. The lognormal parameters of the equivalent shear strength were found by means of correlating quantiles of the lognormal microstiffness distribution and the equivalent shear strength. The lognormally distributed equivalent shear stresses were used for calculation of the degree of utilization in the hydrates, a ratio of the microstress in the hydrates with respect to their strength.

5.3 Research contribution and main findings

The experimental as well as the modeling campaigns contribute to the knowledge in (dental) cement research in several ways: (i) the hydration products of the dental cement paste are about twice as stiff and three times harder as the hydration products in construction cement pastes. The high-density version of the hydrates occupies the largest relative volumetric amount of the hardened material, this is the opposite to hardened construction cement pastes. (ii) The mature dental cement paste contains defects and cracks that likely lower the overall Biodentine performance. (iii) Representative quantity of a skewed lognormal distribution is its median. (iv) The smaller the length-to-diameter ratio ("slenderness ratio") of cylindrical specimens of Biodentine, the larger is the maximum force sustained by these specimens when crushed under uniaxial compression.

The main findings are summarized according to the research objectives as follows:

- **Grid nanoindentation:**

Probing well-hardened dental cement paste revealed the existence of calcite-reinforced hydration products, which are significantly stiffer and stronger than hydrates of construction cement pastes. Thousands of indentation experiments revealed skewed rather than symmetric stiffness distributions of indentation-related stiffness and strength properties of the material constituents. These distributions were represented by lognormal probability density functions.

- **Ultrasonic pulse transmission technique:**

Ultrasonic tests revealed that macroscopic stiffness of a dental cement paste older than seven days is independent on material age. The homogenized stiffnesses were also fairly independent on central frequency of the transducers ranging from 50 kHz to 20 MHz. Given that the highest frequency of the longitudinal wave sent through the material characterized an RVE as large as 25 μm , this underlines the fine microstructure of the dental cement paste.

- **Compressive strength tests:**

The stress-strain diagrams of specimens younger than 90 minutes exhibit some pre-peak ductility. At later ages, the material behaves virtually linearly elastic until it fails in brittle fashion. After one day of production, the specimens broke into many fragments, so that classical categorizations concerning the propagation direction of single cracks were not useful any longer. The maximum force sustained by a cylindrical specimen is the larger, the smaller is its slenderness ratio. Empirical correction factors of the ASTM C39 dedicated for concrete cylinders, applied to dental cement paste specimens, delivered virtually the same estimate of the uniaxial compressive strength. This indicates

that the correction factors account for a structural effect rather than for a material property.

- **Simple micromechanical modeling:**

The discrepancy between the ultrasonically derived homogenized stiffness and the micromechanical estimates, derived from the nanoindentation probed hydrate, clinker and zirconia phases, indicates the presence of microstructural defects in mature dental cement paste, which may worsen its macroscopic mechanical properties.

- **Improved model for stiffness upscaling:**

The identified value of Poisson's ratio of the lower-density and high-density calcite-reinforced hydrates of Biodentine, $\nu_h = 0.20$, is smaller than Poisson's ratio assumed for the low-density and high-density calcium-silicate-hydrates of Portland cements, $\nu = 0.24$ (Constantinides, 2002). This difference may be caused by a reinforcement effect of calcite and calcium hydroxide. The crack density parameter corresponding to the grain boundary defects was identified as $\omega = 0.78$. The defects are responsible for almost 50% of the deviatoric deformation of Biodentine. Provided that medians of the microscopic stiffness distributions are assigned to the two types hydrates in the piecewise uniform model, the result of bottom-up stiffness homogenization is virtually equivalent to the lognormal microelasticity model. Top-down strain and stress quantification revealed important differences between the model accounting for microstiffness distributions of the hydrates and the model which is based on piecewise uniform microscopic stiffness values. The former approach provides direct access to microscopic stress fluctuations, whereas the latter approach leads to volume-averaged values of the stresses experienced by the two populations of hydrates.

- **Explanation of compressive strength:**

The probability density function of the effective shear strength (which is a cohesion-related quantity), that belongs to the high-density calcite-reinforced hydrates, was introduced to be of lognormal nature. Based on the identified lognormal parameters of the effective shear strength, it was found that some 85% of the high-density calcite-reinforced hydrates have virtually the same degree of utilization (a ratio of stress-to-strength). This corresponds to some 63% of the volume of the dental cement paste, which fails at virtually the same macroscopic loading. Given the very brittle failure mode of the dental cement paste, this explanation seems plausible.

5.4 Perspectives

The experimental campaign, introduced here, provided insights into the properties of the dental cement paste. However, there are more aspects that may be beneficial not only for future development of dental cement pastes, but also to cement and concrete research in particular. As regards experimental investigation at nanometric scale, TEM imaging can provide valuable information as regards the grain boundary defects and cracks as well as the calcite-reinforced hydrates. Quantification of water at different scales by means of ^1H NMR could provide important insight into the microstructure of the dental cement paste. As regards experiments providing access to the macrostructural elastic properties, ultrasound investigation of young dental cement paste with material age up to 7 days would nicely complement the measurements carried out within this work.

From the micromechanical modeling viewpoint, it would be very interesting to resolve the high-density calcite-reinforced hydrates even into smaller scale, similarly to Königsberger et al. (2020) resolving the C-S-H foam into solid C-S-H and gel pores. In this context, it would be of extreme interest to study the reinforcing effect of calcite and calcium hydroxide. At last, but not least, studying the boundary interfaces and defects could be of importance in order to understand, and possibly improve the properties of dental cement pastes even further.

Bibliography

- Achenbach, J. (1973). *Wave propagation in elastic solids, One-dimensional motion of an elastic continuum*. Elsevier. ISBN: 978-1-4831-6373-4.
- Alhodiry, W., Lyons, M., and Chadwick, R. (2014). Effect of saliva and blood contamination on the bi-axial flexural strength and setting time of two calcium-silicate based cements: Portland cement and Biodentine. *The European Journal of Prosthodontics and Restorative Dentistry*, 22(1):20–23.
- Alzraikat, H., Taha, N. A., and Salameh, A. (2016). A comparison of physical and mechanical properties of Biodentine and Mineral Trioxide Aggregate. *Journal of Research in Medical and Dental Science*, 4(2):121–126.
- American Society for Testing and Materials (2021). *Standard Test Method for Compressive Strength of Cylindrical Concrete Specimens, ASTM Standard C39/C39M–21*.
- Amieur, M. (1994). *Etude numérique et expérimentale des effets d'échelle et de conditions aux limites sur des éprouvettes de béton n'ayant pas le volume représentatif [Numerical and experimental study of scale effects and boundary conditions on concrete specimens having no representative volume]*. PhD thesis, École Polytechnique Fédérale de Lausanne (EPFL).
- Angker, L., Swain, M. V., and Kilpatrick, N. (2003). Micro-mechanical characterisation of the properties of primary tooth dentine. *Journal of Dentistry*, 31(4):261–267.
- Atmeh, A. R. (2020). Investigating the effect of bicarbonate ion on the structure and strength of calcium silicate-based dental restorative material—Biodentine. *Clinical Oral Investigations*, 24(12):4597–4606.
- Auriault, J.-L., Boutin, C., and Geindreau, C. (2010). *Homogenization of coupled phenomena in heterogenous media*, volume 149. John Wiley & Sons. ISBN: 978-1-848-21161-2.
- Ausweger, M., Binder, E., Lahayne, O., Reihnsner, R., Maier, G., Peyerl, M., and Pichler, B. (2019). Early-age evolution of strength, stiffness, and non-aging creep of concretes: Experimental characterization and correlation analysis. *Materials*, 12(2):207.
- Balooch, M., Demos, S., Kinney, J., Marshall, G., Balooch, G., and Marshall, S. (2001). Local mechanical and optical properties of normal and transparent root dentin. *Journal of Materials Science: Materials in Medicine*, 12(6):507–514.
- Barbour, M. E., Parker, D. M., and Jandt, K. D. (2003). Enamel dissolution as a function of solution degree of saturation with respect to hydroxyapatite: A nanoindentation study. *Journal of Colloid and Interface Science*, 265(1):9–14.

- Benveniste, Y. (1987). A new approach to the application of Mori-Tanaka's theory in composite materials. *Mechanics of Materials*, 6(2):147–157.
- Bernard, O., Ulm, F.-J., and Lemarchand, E. (2003). A multiscale micromechanics-hydration model for the early-age elastic properties of cement-based materials. *Cement and Concrete Research*, 33(9):1293–1309.
- Binder, E. (2019). *Multiscale analysis of time-dependent behavior of cementitious materials: High-dynamic strength gain and temperature-activated creep*. PhD thesis, Vienna University of Technology, Karlsplatz 13/202, Vienna, Austria.
- Binder, E., Reihnsner, R., Yuan, Y., Mang, H. A., and Pichler, B. L. A. (2020). High-dynamic compressive and tensile strength of specimens made of cementitious materials. *Cement and Concrete Research*, 129:105890.
- Bronnec, F., Colon, P., and Plasse-Pradelle, N. (2010). Dimensional changes of a Ca_3SiO_5 based cement during setting. In *Poster Session, IADR Congress, Barcelona*, page ID: 3090.
- Brown, L., Allison, P. G., and Sanchez, F. (2018). Use of nanoindentation phase characterization and homogenization to estimate the elastic modulus of heterogeneously decalcified cement pastes. *Materials & Design*, 142:308–318.
- Budiansky, B. and O'Connell, R. J. (1976). Elastic moduli of a cracked solid. *International Journal of Solids and Structures*, 12(2):81–97.
- Butt, N., Talwar, S., Chaudhry, S., Nawal, R. R., Yadav, S., and Bali, A. (2014). Comparison of physical and mechanical properties of mineral trioxide aggregate and Biodentine. *Indian Journal of Dental Research*, 25(6):692.
- Camilleri, J. (2022). BiodentineTM microstructure and composition. In *BiodentineTM*, pages 1–10. Springer. ISBN: 978-3-030-80931-7.
- Camilleri, J., Sorrentino, F., and Damidot, D. (2013). Investigation of the hydration and bioactivity of radiopacified tricalcium silicate cement, Biodentine and MTA Angelus. *Dental Materials*, 29(5):580–593.
- Carcione, J. M. (2007). *Wave fields in real media: Wave propagation in anisotropic, anelastic, porous and electromagnetic media*. Elsevier. ISBN: 978-0-0804-6890-7.
- Chan, Y., Ngan, A., and King, N. (2011). Nano-scale structure and mechanical properties of the human dentine-enamel junction. *Journal of the Mechanical Behavior of Biomedical Materials*, 4(5):785–795.
- Chang, S. W. (2018). Chemical composition and porosity characteristics of various calcium silicate-based endodontic cements. *Bioinorganic Chemistry and Applications*, 2018.
- Chaudhry, M. A., Qadir, A., Rafique, M., and Zubair, S. (1997). Extension of Euler's beta function. *Journal of Computational and Applied Mathematics*, 78(1):19–32.
- Chen, J. J., Sorelli, L., Vandamme, M., Ulm, F.-J., and Chanvillard, G. (2010). A coupled nanoindentation/SEM-EDS study on low water/cement ratio Portland cement paste: Evidence for C-S-H/ $\text{Ca}(\text{OH})_2$ nanocomposites. *Journal of the American Ceramic Society*, 93(5):1484–1493.

- Constantinides, G. (2002). The elastic properties of calcium leached cement pastes and mortars: A multi-scale investigation. Master's thesis, Massachusetts Institute of Technology.
- Constantinides, G., Chandran, K. R., Ulm, F.-J., and Van Vliet, K. (2006). Grid indentation analysis of composite microstructure and mechanics: Principles and validation. *Materials Science and Engineering: A*, 430(1-2):189–202.
- Constantinides, G. and Ulm, F.-J. (2004). The effect of two types of C-S-H on the elasticity of cement-based materials: Results from nanoindentation and micromechanical modeling. *Cement and Concrete Research*, 34(1):67–80.
- Constantinides, G. and Ulm, F.-J. (2007). The nanogranular nature of C-S-H. *Journal of the Mechanics and Physics of Solids*, 55(1):64–90.
- Constantinides, G., Ulm, F.-J., and Van Vliet, K. (2003). On the use of nanoindentation for cementitious materials. *Materials and Structures*, 36(3):191–196.
- Da Silva, W., Němeček, J., and Štemberk, P. (2014). Methodology for nanoindentation-assisted prediction of macroscale elastic properties of high performance cementitious composites. *Cement and Concrete Composites*, 45:57–68.
- Damien, D., Wang, Y., and Xi, Y. (2019). Prediction of elastic properties of cementitious materials based on multiphase and multiscale micromechanics theory. *Journal of Engineering Mechanics*, 145(10):04019074.
- Deudé, V., Dormieux, L., Kondo, D., and Maghous, S. (2002). Micromechanical approach to nonlinear poroelasticity: Application to cracked rocks. *Journal of Engineering Mechanics*, 128(8):848–855.
- Deus, G. D., Camilleri, J., Primus, C. M., Duarte, M. A. H., and Bramante, C. M. (2014). Introduction to mineral trioxide aggregate. In *Mineral Trioxide Aggregate in Dentistry*, pages 1–17. Springer. ISBN: 978-3-642-55156-7.
- Diamond, S. and Bonen, D. (1993). Microstructure of hardened cement paste—a new interpretation. *Journal of the American Ceramic Society*, 76(12):2993–2999.
- Dohnalík, P., Hellmich, C., Richard, G., and Pichler, B. L. A. (2022). Stiffness and stress fluctuations in dental cement paste: A continuum micromechanics approach. *Mechanics of Advanced Materials and Structures*, pages 1–19.
- Dohnalík, P., Pichler, B. L. A., Zelaya-Lainez, L., Lahayne, O., Richard, G., and Hellmich, C. (2021). Micromechanics of dental cement paste. *Journal of the Mechanical Behavior of Biomedical Materials*, 124:104863.
- Donnelly, E., Baker, S. P., Boskey, A. L., and van der Meulen, M. C. (2006). Effects of surface roughness and maximum load on the mechanical properties of cancellous bone measured by nanoindentation. *Journal of Biomedical Materials Research Part A*, 77(2):426–435.
- Dormieux, L., Kondo, D., and Ulm, F.-J. (2006). *Microporomechanics*. John Wiley & Sons. ISBN: 978-0-4700-3199-5.
- Drugan, W. and Willis, J. (1996). A micromechanics-based nonlocal constitutive equation and estimates of representative volume element size for elastic composites. *Journal of the Mechanics and Physics of Solids*, 44(4):497–524.

- Elnaghy, A. M. (2014). Influence of acidic environment on properties of Biodentine and white Mineral Trioxide Aggregate: A comparative study. *Journal of Endodontics*, 40(7):953–957.
- Elsaka, S. E., Elnaghy, A. M., Mandorah, A., and Elshazli, A. H. (2019). Effect of titanium tetrafluoride addition on the physicochemical and antibacterial properties of Biodentine as intraorifice barrier. *Dental Materials*, 35(1):185–193.
- Eshelby, J. D. (1957). The determination of the elastic field of an ellipsoidal inclusion, and related problems. *Proceedings of the Royal Society of London: Series A*, 241(1226):376–396.
- Fischer, I., Pichler, B., Lach, E., Terner, C., Barraud, E., and Britz, F. (2014). Compressive strength of cement paste as a function of loading rate: Experiments and engineering mechanics analysis. *Cement and Concrete Research*, 58:186–200.
- Ford, E., Arora, A., Mobasher, B., Hoover, C. G., and Neithalath, N. (2020). Elucidating the nano-mechanical behavior of multi-component binders for ultra-high performance concrete. *Construction and Building Materials*, 243:118214.
- Franquin, J.-C., Marie, O., Bottero, M.-J., Koubi, G., and About, I. (2010). Physical properties of a new Ca_3SiO_5 -based dentin substitute. In *Poster Session, IADR Congress, Barcelona*, page ID: 4572.
- Fränzel, W. and Gerlach, R. (2009). The irradiation action on human dental tissue by X-rays and electrons – a nanoindenter study. *Zeitschrift für Medizinische Physik*, 19(1):5–10.
- Freedman, D. and Diaconis, P. (1981). On the histogram as a density estimator: L_2 theory. *Zeitschrift für Wahrscheinlichkeitstheorie und verwandte Gebiete*, 57(4):453–476.
- Furin, I., Pastrama, M.-I., Kariem, H., Luczynski, K. W., Lahayne, O., and Hellmich, C. (2016). A new nanoindentation protocol for identifying the elasticity of undamaged extracellular bone tissue. *MRS Advances*, 1(11):693–704.
- Gao, X., Wei, Y., and Huang, W. (2017). Effect of individual phases on multiscale modeling mechanical properties of hardened cement paste. *Construction and Building Materials*, 153:25–35.
- Garboczi, E. J. and Lura, P. (2020). Local elastic moduli of simple random composites computed at different length scales. *Materials and Structures*, 53(6):1–16.
- Göbel, L., Bos, C., Schwaiger, R., Flohr, A., and Osburg, A. (2018). Micromechanics-based investigation of the elastic properties of polymer-modified cementitious materials using nanoindentation and semi-analytical modeling. *Cement and Concrete Composites*, 88:100–114.
- Govindaraju, L., Neelakantan, P., and Gutmann, J. L. (2017). Effect of root canal irrigating solutions on the compressive strength of tricalcium silicate cements. *Clinical oral Investigations*, 21(2):567–571.
- Grazziotin-Soares, R., Nekoofar, M. H., Davies, T., Hübler, R., Meraji, N., and Dummer, P. M. (2019). Crystalline phases involved in the hydration of calcium silicate-based cements: Semi-quantitative Rietveld X-ray diffraction analysis. *Australian Endodontic Journal*, 45(1):26–32.

- Guidoni, G., Denkmayr, J., Schöberl, T., and Jäger, I. (2006). Nanoindentation in teeth: Influence of experimental conditions on local mechanical properties. *Philosophical Magazine*, 86(33-35):5705–5714.
- Guneser, M. B., Akbulut, M. B., and Eldeniz, A. U. (2013). Effect of various endodontic irrigants on the push-out bond strength of Biodentine and conventional root perforation repair materials. *Journal of Endodontics*, 39(3):380–384.
- Ha, W. N., Bentz, D. P., Kahler, B., and Walsh, L. J. (2015). D90: The strongest contributor to setting time in Mineral Trioxide Aggregate and Portland cement. *Journal of Endodontics*, 41(7):1146–1150.
- Habelitz, S., Marshall Jr, G. W., Balooch, M., and Marshall, S. J. (2002). Nanoindentation and storage of teeth. *Journal of Biomechanics*, 35(7):995–998.
- Halgaš, R., Dusza, J., Kaiferová, J., Kováčsová, L., and Markovská, N. (2013). Nanoindentation testing of human enamel and dentin. *Ceramics–Silikáty*, 57(2):92–99.
- Hashin, Z. (1983). Analysis of composite materials—a survey. *Journal of Applied Mechanics*, 50:481–505.
- Hellmich, C. and Mang, H. (2005). Shotcrete elasticity revisited in the framework of continuum micromechanics: From submicron to meter level. *Journal of Materials in Civil Engineering*, 17(3):246–256.
- Hershey, A. (1954). The elasticity of an isotropic aggregate of anisotropic cubic crystals. *Journal of Applied Mechanics-Transactions of the ASME*, 21(3):236–240.
- Hill, R. (1963). Elastic properties of reinforced solids: Some theoretical principles. *Journal of the Mechanics and Physics of Solids*, 11(5):357–372.
- Hill, R. (1965a). Continuum micro-mechanics of elastoplastic polycrystals. *Journal of the Mechanics and Physics of Solids*, 13(2):89–101.
- Hill, R. (1965b). A self-consistent mechanics of composite materials. *Journal of the Mechanics and Physics of Solids*, 13(4):213–222.
- Hlobil, M., Šmilauer, V., and Chanvillard, G. (2016). Micromechanical multiscale fracture model for compressive strength of blended cement pastes. *Cement and Concrete Research*, 83:188–202.
- Hussey, R. J. and Wilson, J. (1998). *Advanced technical ceramics directory and databook*. Springer Science & Business Media. ISBN: 978-1-4419-8662-7.
- International Federation for Structural Concrete (2010). *fib Model Code for Concrete Structures 2010*. Ernst & Sohn: Berlin, Germany.
- International Organization for Standardization (2007). *Dentistry — Water-based cements — Part 1: Powder/liquid acid-base cements, ISO 9917-1:2007*.
- Irfan-ul-Hassan, M., Pichler, B., Reihnsner, R., and Hellmich, C. (2016). Elastic and creep properties of young cement paste, as determined from hourly repeated minute-long quasi-static tests. *Cement and Concrete Research*, 82:36–49.

- Jagsch, V., Kuttke, P., Lahayne, O., Zelaya-Lainez, L., Scheiner, S., and Hellmich, C. (2020). Multiscale and multitechnique investigation of the elasticity of grooved rail steel. *Construction and Building Materials*, 238:117768.
- Jang, E., Lee, J., Nam, S., Kwon, T., and Kim, H. (2021). Comparison of microleakage and compressive strength of different base materials. *Journal of the Korean Academy of Pediatric Dentistry*, 48(2):168–175.
- Jeng, Y.-R., Lin, T.-T., Hsu, H.-M., Chang, H.-J., and Shieh, D.-B. (2011). Human enamel rod presents anisotropic nanotribological properties. *Journal of the Mechanical Behavior of Biomedical Materials*, 4(4):515–522.
- Jennings, H. M. (2000). A model for the microstructure of calcium silicate hydrate in cement paste. *Cement and Concrete Research*, 30(1):101–116.
- Johnson, D. (1997). The triangular distribution as a proxy for the beta distribution in risk analysis. *Journal of the Royal Statistical Society: Series D (The Statistician)*, 46(3):387–398.
- Juenger, M. C. G. and Jennings, H. M. (2001). The use of nitrogen adsorption to assess the microstructure of cement paste. *Cement and Concrete Research*, 31(6):883–892.
- Karte, P., Hlobil, M., Reihnsner, R., Dörner, W., Lahayne, O., Eberhardsteiner, J., and Pichler, B. (2015). Unloading-based stiffness characterisation of cement pastes during the second, third and fourth day after production. *Strain*, 51(2):156–169.
- Keskin, C., Sariyilmaz, E., and Keleş, A. (2019). The effect of bleaching agents on the compressive strength of calcium silicate-based materials. *Australian Endodontic Journal*, 45(3):311–316.
- Kohlhauser, C. (2009). *Elasticity tensor determination by means of ultrasonic pulse transmission: Application ranges in terms of specimen geometry and microstructure, off-diagonal tensor components, as well as different engineering and biomedical materials*. PhD thesis, Vienna University of Technology, Karlsplatz 13/202, Vienna, Austria (July 2009).
- Kohlhauser, C. and Hellmich, C. (2012). Determination of Poisson’s ratios in isotropic, transversely isotropic, and orthotropic materials by means of combined ultrasonic-mechanical testing of normal stiffnesses: Application to metals and wood. *European Journal of Mechanics - A/Solids*, 33:82–98.
- Kohlhauser, C. and Hellmich, C. (2013). Ultrasonic contact pulse transmission for elastic wave velocity and stiffness determination: Influence of specimen geometry and porosity. *Engineering Structures*, 47:115–133.
- Königsberger, M. (2016). *Multiscale microstructural modeling in cement and concrete: From hydration to poroelasticity, creep, and strength*. PhD thesis, Vienna University of Technology, Karlsplatz 13/202, Vienna, Austria.
- Königsberger, M., Hellmich, C., and Pichler, B. (2016). Densification of C-S-H is mainly driven by available precipitation space, as quantified through an analytical cement hydration model based on NMR data. *Cement and Concrete Research*, 88:170–183.
- Königsberger, M., Hlobil, M., Delsaute, B., Staquet, S., Hellmich, C., and Pichler, B. (2018). Hydrate failure in ITZ governs concrete strength: A micro-to-macro validated engineering mechanics model. *Cement and Concrete Research*, 103:77–94.

- Königsberger, M., Pichler, B., and Hellmich, C. (2020). Multiscale poro-elasticity of densifying calcium-silicate hydrates in cement paste: An experimentally validated continuum micromechanics approach. *International Journal of Engineering Science*, 147:103196.
- Königsberger, M. and Staquet, S. (2018). Micromechanical multiscale modeling of ITZ-driven failure of recycled concrete: Effects of composition and maturity on the material strength. *Applied Sciences*, 8(6):976.
- Königsberger, M., Zelaya-Lainez, L., Lahayne, O., Pichler, B. L., and Hellmich, C. (2021). Nanoindentation-probed Oliver-Pharr half-spaces in alkali-activated slag-fly ash pastes: Multimethod identification of microelasticity and hardness. *Mechanics of Advanced Materials and Structures*, pages 1–12.
- Kyocera Group (2019). Zirconia - Zirconium Dioxide, ZrO_2 . Accessed on: June, 4, 2019. [Online]. Available: <https://global.kyocera.com/prdct/fc/list/material/zirconia/zirconia.html>.
- Laurent, P., Camps, J., and About, I. (2012). Biodentine™ induces TGF- β 1 release from human pulp cells and early dental pulp mineralization. *International Endodontic Journal*, 45(5):439–448.
- Laurent, P., Camps, J., De Méo, M., Déjou, J., and About, I. (2008). Induction of specific cell responses to a Ca_3SiO_5 -based posterior restorative material. *Dental Materials*, 24(11):1486–1494.
- Lavergne, F., Fraj, A. B., Bayane, I., and Barthélémy, J. (2018). Estimating the mechanical properties of hydrating blended cementitious materials: An investigation based on micromechanics. *Cement and Concrete Research*, 104:37–60.
- Laws, N. (1977). The determination of stress and strain concentrations at an ellipsoidal inclusion in an anisotropic material. *Journal of Elasticity*, 7(1):91–97.
- Lee, S.-J., Monsef, M., and Torabinejad, M. (1993). Sealing ability of a mineral trioxide aggregate for repair of lateral root perforations. *Journal of Endodontics*, 19(11):541–544.
- Li, Q., Hurt, A. P., and Coleman, N. J. (2019). The application of ^{29}Si NMR spectroscopy to the analysis of calcium silicate-based cement using Biodentine as an example. *Journal of Functional Biomaterials*, 10(2):25.
- Li, Y., Liu, Y., and Wang, R. (2021). Evaluation of the elastic modulus of concrete based on indentation test and multi-scale homogenization method. *Journal of Building Engineering*, 43:102758.
- Li, Y., Wang, P., and Wang, Z. (2017). Evaluation of elastic modulus of cement paste corroded in brine solution with advanced homogenization method. *Construction and Building Materials*, 157:600–609.
- Liang, S., Wei, Y., and Wu, Z. (2017). Multiscale modeling elastic properties of cement-based materials considering imperfect interface effect. *Construction and Building Materials*, 154:567–579.
- Lura, P., Trtik, P., and Münch, B. (2011). Validity of recent approaches for statistical nanoindentation of cement pastes. *Cement and Concrete Composites*, 33(4):457–465.

- Ma, Y., Ye, G., and Hu, J. (2017). Micro-mechanical properties of alkali-activated fly ash evaluated by nanoindentation. *Construction and Building Materials*, 147:407–416.
- Mahoney, E., Holt, A., Swain, M., and Kilpatrick, N. (2000). The hardness and modulus of elasticity of primary molar teeth: An ultra-micro-indentation study. *Journal of Dentistry*, 28(8):589–594.
- Mahoney, E. K., Rohanizadeh, R., Ismail, F., Kilpatrick, N., and Swain, M. (2004). Mechanical properties and microstructure of hypomineralised enamel of permanent teeth. *Biomaterials*, 25(20):5091–5100.
- Merkel, C., Deuschle, J., Griesshaber, E., Enders, S., Steinhauser, E., Hochleitner, R., Brand, U., and Schmahl, W. W. (2009). Mechanical properties of modern calcite-(mergerlia truncata) and phosphate-shelled brachiopods (discradisca stella and lingula anatina) determined by nanoindentation. *Journal of Structural Biology*, 168(3):396–408.
- Miller, M., Bobko, C., Vandamme, M., and Ulm, F.-J. (2008). Surface roughness criteria for cement paste nanoindentation. *Cement and Concrete Research*, 38(4):467–476.
- Miller, S. A., Horvath, A., and Monteiro, P. J. (2016). Readily implementable techniques can cut annual CO₂ emissions from the production of concrete by over 20%. *Environmental Research Letters*, 11(7):074029.
- Muller, A., Scrivener, K., Gajewicz, A., and McDonald, P. (2013a). Use of bench-top NMR to measure the density, composition and desorption isotherm of C-S-H in cement paste. *Microporous and Mesoporous Materials*, 178:99–103.
- Muller, A. C., Scrivener, K. L., Gajewicz, A. M., and McDonald, P. J. (2013b). Densification of C-S-H measured by 1H NMR relaxometry. *The Journal of Physical Chemistry C*, 117(1):403–412.
- Müller, N. and Harnisch, J. (2008). How to turn around the trend of cement related emissions in the developing world. *WWF—Lafarge Conservation Partnership: Gland, Switzerland*.
- Nagas, E., Cehreli, Z. C., Uyanik, O., Vallittu, P. K., and Lassila, L. V. (2016). Reinforcing effect of glass fiber-incorporated ProRoot MTA and Biodentine as intraorifice barriers. *Journal of Endodontics*, 42(11):1673–1676.
- Natale, L., Rodrigues, M., Xavier, T., Simões, A., De Souza, D., and Braga, R. (2015). Ion release and mechanical properties of calcium silicate and calcium hydroxide materials used for pulp capping. *International Endodontic Journal*, 48(1):89–94.
- Němeček, J., Králík, V., and Vondřejc, J. (2013). Micromechanical analysis of heterogeneous structural materials. *Cement and Concrete Composites*, 36:85–92.
- Oliver, W. C. and Pharr, G. M. (1992). An improved technique for determining hardness and elastic modulus using load and displacement sensing indentation experiments. *Journal of Materials Research*, 7(6):1564–1583.
- Park, S., Quinn, J., Romberg, E., and Arola, D. (2008). On the brittleness of enamel and selected dental materials. *Dental Materials*, 24(11):1477–1485.

- Pastrama, M.-I., Blanchard, R., Clement, J. G., Pivonka, P., and Hellmich, C. (2018). Modal analysis of nanoindentation data, confirming that reduced bone turnover may cause increased tissue mineralization/elasticity. *Journal of the Mechanical Behavior of Biomedical Materials*, 84:217–224.
- Pensée, V. and He, Q.-C. (2007). Generalized self-consistent estimation of the apparent isotropic elastic moduli and minimum representative volume element size of heterogeneous media. *International Journal of Solids and Structures*, 44(7-8):2225–2243.
- Pensée, V., Kondo, D., and Dormieux, L. (2002). Micromechanical analysis of anisotropic damage in brittle materials. *Journal of Engineering Mechanics*, 128(8):889–897.
- Pichler, B. and Hellmich, C. (2011). Upscaling quasi-brittle strength of cement paste and mortar: A multi-scale engineering mechanics model. *Cement and Concrete Research*, 41(5):467–476.
- Pichler, B., Hellmich, C., and A. Mang, H. (2007). A combined fracture-micromechanics model for tensile strain-softening in brittle materials, based on propagation of interacting microcracks. *International Journal for Numerical and Analytical Methods in Geomechanics*, 31(2):111–132.
- Pichler, B., Hellmich, C., and Eberhardsteiner, J. (2009). Spherical and acicular representation of hydrates in a micromechanical model for cement paste: Prediction of early-age elasticity and strength. *Acta Mechanica*, 203(3):137–162.
- Pichler, B., Hellmich, C., Eberhardsteiner, J., Wasserbauer, J., Termkhajornkit, P., Barbarulo, R., and Chanvillard, G. (2013). The counteracting effects of capillary porosity and of unhydrated clinker grains on the macroscopic strength of hydrating cement paste—a multi-scale model. *9th International Conference on Creep, Shrinkage, and Durability Mechanics, (CONCREEP-9)*:40–47.
- Pichler, B., Hellmich, C., and Mang, H. A. (2005). Impact of rocks onto gravel design and evaluation of experiments. *International Journal of Impact Engineering*, 31(5):559–578.
- Poplai, G., Jadhav, S., and Hegde, V. (2012). Effect of acidic environment on the push-out bond strength of Biodentine™. *World Journal of Dentistry*, 3:313–315.
- Primus, C. M., Tay, F. R., and Niu, L. (2019). Bioactive tri/dicalcium silicate cements for treatment of pulpal and periapical tissues. *Acta Biomaterialia*, 96:35–54.
- Rajasekharan, S., Martens, L., Cauwels, R., and Anthonappa, R. P. (2018). Biodentine™ material characteristics and clinical applications: A 3 year literature review and update. *European Archives of Paediatric Dentistry*, 19(1):1–22.
- Rajasekharan, S., Martens, L., Cauwels, R., and Verbeeck, R. (2014). Biodentine™ material characteristics and clinical applications: a review of the literature. *European Archives of Paediatric Dentistry*, 15(3):147–158.
- Reuss, A. (1929). Berechnung der Fließgrenze von Mischkristallen auf Grund der Plastizitätsbedingung für Einkristalle. *Zeitschrift für Angewandte Mathematik und Mechanik*, 9(1):49–58.

- Sanahuja, J., Dormieux, L., and Chanvillard, G. (2007). Modelling elasticity of a hydrating cement paste. *Cement and Concrete Research*, 37(10):1427–1439.
- Sarris, E. and Constantinides, G. (2013). Finite element modeling of nanoindentation on C–S–H: Effect of pile-up and contact friction. *Cement and Concrete Composites*, 36:78–84.
- Schmid, S. (2018). Die homogenisierte elastische Steifigkeit von Granit: Mikromechanische Berechnung unter Berücksichtigung von isotroper Risschädigung. Bachelor's thesis, Vienna University of Technology, Karlsplatz 13/202, Vienna, Austria.
- Shahsavari, A. and Picu, R. (2013). Size effect on mechanical behavior of random fiber networks. *International Journal of Solids and Structures*, 50(20-21):3332–3338.
- Sheykhrezae, M. S., Meraji, N., Ghanbari, F., Nekoofar, M. H., Bolhari, B., and Dummer, P. M. (2018). Effect of blood contamination on the compressive strength of three calcium silicate-based cements. *Australian Endodontic Journal*, 44(3):255–259.
- Sorelli, L., Constantinides, G., Ulm, F.-J., and Toutlemonde, F. (2008). The nano-mechanical signature of ultra high performance concrete by statistical nanoindentation techniques. *Cement and Concrete Research*, 38(12):1447–1456.
- Stefaniuk, D., Niewiadomski, P., Musial, M., and Lydzba, D. (2019). Elastic properties of self-compacting concrete modified with nanoparticles: Multiscale approach. *Archives of Civil and Mechanical Engineering*, 19(4):1150–1162.
- Stora, E., He, Q.-C., and Bary, B. (2006). Influence of inclusion shapes on the effective linear elastic properties of hardened cement pastes. *Cement and Concrete Research*, 36(7):1330–1344.
- Subramanyam, D. and Vasantharajan, M. (2017). Effect of oral tissue fluids on compressive strength of MTA and biodentine: An in vitro study. *Journal of Clinical and Diagnostic Research: JCDR*, 11(4):ZC94.
- Taplin, J. (1959). A method for following the hydration reaction in Portland cement paste. *Australian Journal of Applied Science*, 10:329–345.
- Taylor, H. F. et al. (1997). *Cement chemistry*, volume 2. Thomas Telford London. ISBN: 978-0-7277-2592-9.
- Tennis, P. D. and Jennings, H. M. (2000). A model for two types of calcium silicate hydrate in the microstructure of Portland cement pastes. *Cement and Concrete Research*, 30(6):855–863.
- Torabinejad, M., Watson, T., and Ford, T. P. (1993). Sealing ability of a mineral trioxide aggregate when used as a root end filling material. *Journal of Endodontics*, 19(12):591–595.
- Torabinejad, M. and White, D. J. (1993a). Tooth filling material and method of use: US Patent Number 5415547. 1993.
- Torabinejad, M. and White, D. J. (1993b). Tooth filling material and method of use: US Patent Number 5769638. 1993.

- Ulm, F.-J., Vandamme, M., Bobko, C., Ortega, J. A., Tai, K., and Ortiz, C. (2007). Statistical indentation techniques for hydrated nanocomposites: Concrete, bone, and shale. *Journal of the American Ceramic Society*, 90(9):2677–2692.
- Uyanik, O., Nagas, E., Kucukkaya Eren, S., Cehreli, Z. C., Vallittu, P. K., and Lassila, L. V. (2019). Effect of phytic acid on the setting times and tensile strengths of calcium silicate-based cements. *Australian Endodontic Journal*, 45(2):241–245.
- Vandamme, M. and Ulm, F.-J. (2009). Nanogranular origin of concrete creep. *Proceedings of the National Academy of Sciences*, 106(26):10552–10557.
- Velez, K., Maximilien, S., Damidot, D., Fantozzi, G., and Sorrentino, F. (2001). Determination by nanoindentation of elastic modulus and hardness of pure constituents of Portland cement clinker. *Cement and Concrete Research*, 31(4):555–561.
- Voigt, W. (1889). Über die Beziehung zwischen den beiden Elasticitätsconstanten isotroper Körper. *Annalen der Physik*, 274(12):573–587.
- Zaoui, A. (2002). Continuum micromechanics: Survey. *Journal of Engineering Mechanics*, 128(8):808–816.
- Zhu, Q.-Z., Shao, J., and Kondo, D. (2011). A micromechanics-based thermodynamic formulation of isotropic damage with unilateral and friction effects. *European Journal of Mechanics - A/Solids*, 30(3):316–325.
- Ziskind, D., Hasday, M., Cohen, S. R., and Wagner, H. D. (2011). Young's modulus of peritubular and intertubular human dentin by nano-indentation tests. *Journal of Structural Biology*, 174(1):23–30.

Personal information

Curriculum Vitae

Personal Data

Name: Petr Dohnalík
Academic Degree: Ing.
Date of Birth: [REDACTED]
Place of Birth: [REDACTED]
Nationality: Czech
Current address: [REDACTED]

Education

11/2017 – 09/2022 Doctoral studies in Civil Engineering at Vienna University of Technology (TU-Wien), Vienna, Austria
09/2014 – 08/2017 Master's studies in Mechanical Engineering at Brno University of Technology
09/2011 – 08/2014 Bachelor's studies in Mechanical Engineering at Brno University of Technology
09/2007 – 06/2011 Technical High School for Electrical Engineering, Olomouc, Czech Republic

Work Experience

11/2017 – 09/2022 Project Assistant, Institute for Mechanics of Materials and Structures, Vienna University of Technology
09/2016 – 10/2017 FEA Structural Engineer at "Honeywell, Inc.", Brno, Czech Republic, part-time employment
12/2014 – 05/2015 Structural Engineer at "Evektor-Aerotechnik, Ltd.", Kunovice, Czech Republic, trainee program

Activities Abroad

11/2021 – 12/2021 Research stay at Septodont R&D Laboratory Saint-Maur-des-Fossés, France
03/2020 – 03/2020 Research stay at Septodont R&D Laboratory Saint-Maur-des-Fossés, France
04/2019 – 04/2019 Research stay at University of Surrey Guildford, United Kingdom
02/2016 – 07/2016 Erasmus+ study program at Graz University of Technology, Austria

Awards and Scholarships

2017 Dean's award for an excellent diploma thesis, granted by the Brno University of Technology
2012, 2015, 2016 Award for excellent performance as a student, granted by the Faculty of Mechanical Engineering, Brno University of Technology

Scientific Dissemination

Publications

- P. Dohnalík, B. L. A. Pichler, L. Zelaya-Lainez, O. Lahayne, G. Richard, and C. Hellmich. Micromechanics of dental cement paste. *Journal of the Mechanical Behavior of Biomedical Materials*, 124:104863, 2021.
- P. Dohnalík, C. Hellmich, G. Richard, and B. L. A. Pichler. Stiffness and stress fluctuations in dental cement paste: A continuum micromechanics approach. *Mechanics of Advanced Materials and Structures*, 1–19, 2022a.
- P. Dohnalík, C. Hellmich, G. Richard, and B. L. A. Pichler. Strength of dental cement paste: Early age testing and micromechanical explanation at mature ages. *submitted to the Frontiers in Bioengineering and Biotechnology*, 2022b.

Conference Papers

- P. Dohnalík, C. Hellmich, O. Lahayne, and B. L. A. Pichler. Stiffness and Strength of Mature Dental Cement Paste. In: *Programme & Proceedings of the China-Austria Forum for Postgraduates of Civil Engineering, Vienna University of Technology, Institute for Mechanics of Materials and Structures*, pages 69–71, 2019.
- P. Dohnalík, B. L. A. Pichler, L. Zelaya-Lainez, O. Lahayne, G. Richard, and C. Hellmich. Experimental and computational micromechanics of dental cement paste. In: *Computational Modelling of Concrete and Concrete Structures (EURO-C 2022), Vienna, Austria*, pages 96–101. CRC Press, 2022.

Conference Presentations and Posters

- P. Dohnalík, B. L. A. Pichler, and C. Hellmich. Innovative Characterization and Multiscale Modeling of Dental Cement Pastes. Oral presentation at the “90th Annual Meeting of the International Association of Applied Mathematics and Mechanics (GAMM 2019)”, Vienna, Austria, 2019.
- P. Dohnalík, C. Hellmich, O. Lahayne, and B. L. A. Pichler. Stiffness and Strength of Mature Dental Cement Paste. Oral presentation at the “China-Austria Forum for Postgraduates of Civil Engineering”, Vienna, Austria, 2019.
- P. Dohnalík, B. L. A. Pichler, L. Zelaya-Lainez, O. Lahayne, and C. Hellmich. Grid Nanoindentation of Mature Dental Cement Paste. Oral presentation at the “ERICA CASH II Final Conference”, 2021.
- P. Dohnalík, B. L. A. Pichler, O. Lahayne, and C. Hellmich. Grid nanoindentation and ultrasonic characterization of dental cement paste. Oral presentation at the conference “Engineering Mechanics Institute Conference and Probabilistic Mechanics & Reliability Conference (EMI/PMC 2021)”, New York, USA, 2021.
- P. Dohnalík, B. L. A. Pichler, L. Zelaya-Lainez, O. Lahayne, G. Richard, and C. Hellmich. Characterization of Dental Cement Paste: Grid Nanoindentation and Ultrasound. Oral presentation at the “37th Danubia-Adria Symposium on Advances in Experimental Mechanics”, Linz, Austria, 2021.